NASA CR- 86055

ULTRA–HIGH TEMPERATURE MEASURING TECHNIQUES

by

P. J. Freyheit, K. J. Nygaard, D. Norcross, P. M. Stone

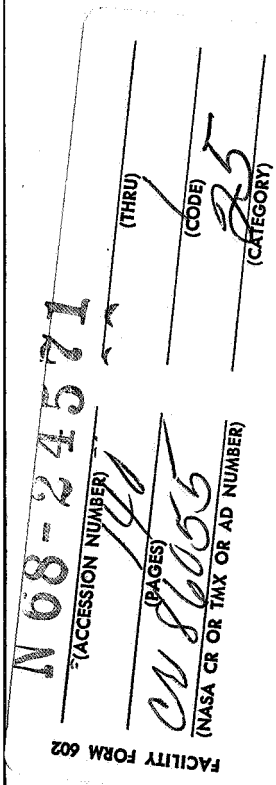

FINAL REPORT

MAY 1968

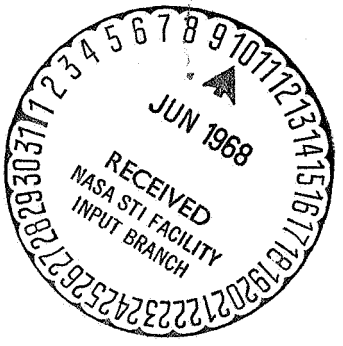

Contract No. NAS 12–86

Electronics Research Center
NATIONAL AERONAUTICS AND SPACE ADMINISTRATION

SPERRY RAND RESEARCH CENTER
SUDBURY, MASSACHUSETTS 01776

Victor E. Scherrer
Technical Monitor
NAS 12–86
Electronics Research Center
575 Technology Square
Cambridge, Massachusetts 02139

Requests for copies of this report should be referred to:

NASA Scientific and Technical Information Facility
P.O. Box 33, College Park, Maryland 20740

NASA CR–

SRRC–CR–68–17

ULTRA–HIGH TEMPERATURE MEASURING TECHNIQUES

by

P. J. Freyheit, K. J. Nygaard, D. Norcross, P. M. Stone

FINAL REPORT

MAY 1968

Contract No. NAS 12–86

Electronics Research Center
NATIONAL AERONAUTICS AND SPACE ADMINISTRATION

SPERRY RAND RESEARCH CENTER
SUDBURY, MASSACHUSETTS 01776

TABLE OF CONTENTS

LIST OF ILLUSTRATIONS

LIST OF ILLUSTRATIONS (cont.)

LIST OF ILLUSTRATIONS (cont.)

LIST OF TABLES

ULTRA HIGH TEMPERATURE MEASURING TECHNIQUES

P. J. Freyheit, K. J. Nygaard, D. Norcross,
P. M. Stone and H. R. Durling
Sperry Rand Research Center
Sudbury, Massachusetts

SUMMARY

Development of a real-time technique for measuring gas temperatures above $5000^{o}K$ in an air nitrogen plasma was investigated using an air plasma in the temperature range from $5,000^{o}K$ to $24,000^{o}K$ at light densities in the range from 10 times normal to 10^{-6} times normal. The temperature measurement techniques considered were Doppler line broadening, line intensity ratios, line-to-continuum intensity ratios, and measurement of particle density with subsequent calculation of temperature. Two methods, line intensity ratios and Doppler broadening, covered the range adequately. A real-time temperature measuring system employing these methods would use photomultiplier tubes as detectors and incorporate an independent means (e.g., Stark broadening) of measuring eletron density.

In investigations of a hot cesium seeded hydrogen plasma, the influence of cesium seed fraction on the cesium-hydrogen plasma photoabsorption coefficient was determined over the pressure range from 0.1 to 100 atmospheres. Plasma temperatures from $5,000^{o}K$ to $20,000^{o}K$ and cesium/hydrogen ratios of 10^{-3} to 10^{-1} were employed. Selected line intensities and shapes, and the plasma absorption coefficient in the ultraviolet region (4.0 - 25 eV) were determined. In addition, the photoabsorption coefficient in the far ultraviolet region was calculated. Spectroscopic techniques for measuring the temperature of hot cesium seeded hydrogen were also analyzed, and a procedure for determining temperature using the Stark broadened width, line center absorption coefficient, and emission energy of selected lines is presented.

The operating characteristics of a wall stabilized arc jet designed to generate the plasmas employed in the program are also discussed.

I. INTRODUCTION

The primary purpose of this program was an investigation of methods of determining the kinetic temperature of an air or nitrogen plasma over a wide range of temperature and density. During the first phase of the contract (1 December 1965 - 30 November 1966) various methods of temperature measurement were evaluated in terms of radiation available from an air plasma over the temperature range from 5,000°K to 24,000°K at light densities ranging from 10 times normal to 10^{-6} times normal. The results are described in the first phase final report, which has been attached as Appendix A. In the present phase of the program, the characteristics of a cesium seeded hydrogen plasma was investigated theoretically and experimentally as part of an investigation of the properties of radiation from very hot (up to 50,000°K) sources.

The technical discussion of work performed during the present phase is divided into three parts. A theoretical discussion of the enhancement of the photoabsorption coefficient of a cesium-hydrogen plasma as a function of cesium seed fraction is presented in Sec. II. Spectroscopic techniques for measuring the temperature of hot cesium seeded hydrogen are described in Sec. III. Supplementary data, presented originally in the 5th Quarterly Technical Report, is included as Appendix B. Finally, Sec. IV is devoted to describing the wall stabilized arc jet used to generate the plasmas investigated during the course of the program.

II. CESIUM-HYDROGEN CONCENTRATIONS AND ABSORPTION COEFFICIENT

A. CESIUM-HYDROGEN CONCENTRATIONS

In the far ultraviolet spectral region, the photoabsorption coefficient of a pure hydrogen plasma (at temperatures high enough that molecular absorption is negligible) is determined almost totally by photoionization of the ground state of the hydrogen atom (Ref. 1). The coefficients for photoionization of excited states and for free-free absorption are lower by over two orders of magnitude. Since the bound-free absorption coefficient is approximately proportional to $(h\nu)^{-3}$ at energies above the ionization threshold of 13.6 eV, there is a rapid falloff in the absorption coefficient for photons with energies more than a few volts above this threshold.

For a high temperature radiating source, a large fraction of the total emitted energy is in the far-ultraviolet spectral region. For a blackbody with a radiant temperature of 50,000°K, the emission spectrum has a maximum at about 12 eV (1000° Å). About 80 percent of the total emitted energy is concentrated in the region from 4 to 25 eV (500 Å to 3000 Å) (Ref. 2). This energy region also encompasses almost all of the interesting photoabsorption regions of the Cs-H plasma.

The pure hydrogen plasma is thus not well suited for use as an absorbing medium for radiation from a high temperature source. Seeding the hydrogen plasma with an alkali metal such as cesium may, however, provide significant enhancement of the photoabsorption coefficient in this region. Since cesium is easily ionized ($E_i = 3.89$ eV), a seeding of cesium will result in an electron density increase at low temperatures (2000°K to 10,000°K) far in excess of the seed fraction. An increase in the free-free absorption coefficient can then be expected. In addition, at any temperature, photoionization of neutral cesium will enhance the absorption coefficient at low photon energies. The coefficients for absorption of continuum radiation by

hydrogen are already well known (Ref. 1). The determination of the additional contribution to the absorption coefficient of the cesium seed necessitates the determination of the densities of the absorbing species and the absorption "oscillator strengths" for the transitions.

The ranges of conditions which were considered are: total gas pressure from 10^{-1} to 10^{2} atmospheres, equilibrium plasma temperature from 5,000°K to 20,000°K, and a ratio of cesium to monatomic hydrogen from 10^{-3} to 10^{-1}. The lower limit for pressure was chosen arbitrarily, but for pressures above 10^{2} atmospheres the lowering of the ionization potential, discussed below, becomes so large as to bring into question the validity of the equation for the partition function of cesium.

It was found (Ref. 3) that hydrogen molecules constitute less than 20% of the hydrogen partial pressure at temperatures above 5000°K in the pressure range of interest. Hence, error due to the photoabsorption by the line spectrum of H_2 is minimized by confining the study to higher temperatures. Above 20,000°K both ground state Cs^{+++} and highly excited Cs^{+} ions begin to become present in significant amounts. Since little is known about the atomic characteristics of these species, it was decided to use this as the upper limiting temperature.

A plasma in thermodynamic equilibrium has its constituents related by the Saha equation. The individual partition functions which are needed can be evaluated when the statistical weights and the excitation energies for the levels of each species in the plasma are known. Because the electron-ion pairs are immersed in a plasma, there is a lowering of the ionization potential of the individual species due to the Debye shielding effect. This effect can be quite significant, and as a practical matter it causes the infinite sums which appear in the partition function to become truncated, which facilitates their evaluation. The Saha equations were solved simultaneously with the equations describing the charge neutrality of the plasma and the mass conservation equations. When the electron density and the

cesium seed fraction (Cs/H) are specified, the equations can be iteratively solved. In most cases, one iteration is sufficient for a high degree of accuracy. Typical results are shown in Figs. 1-4. A more detailed discussion concerning these results is available in the literature (Ref. 4) and in Appendix B.

The degree of ionization of hydrogen is plotted in Fig. 5 for the full range of electron density which is present in the cesium-seeded hydrogen plasma for the ranges of temperature, pressure and cesium seed being considered. The degree of ionization of hydrogen is essentially independent of the seeding (Ref. 4).

B. CESIUM-HYDROGEN ABSORPTION COEFFICIENT

1. Introduction

There are three significant mechanisms which contribute to the absorption of energy in a high temperature gas. When the incident photon energy coincides with the energy difference between an occupied bound state and one of the higher unoccupied states in the same atomic system, there is a definite probability that the photon will be absorbed and the system raised to a higher energy atomic state. Such bound-bound transitions will introduce a discrete contribution to the absorption coefficient.

If the incident photon energy is larger than the difference between the ionization energy and the original energy of the bound atomic system, ionization into the continuum is possible. Such bound-free transitions introduce a continuous contribution to the absorption coefficient and are characterized by a definite threshold energy for the incident photons, dependent on the original bound state involved in the interaction.

Due to the high temperature of the medium under investigation, it will be partially ionized but will maintain charge neutrality. A free electron absorbing a photon of incident radiation in the presence of an ionic potential has a definite probability of occurrence. Such

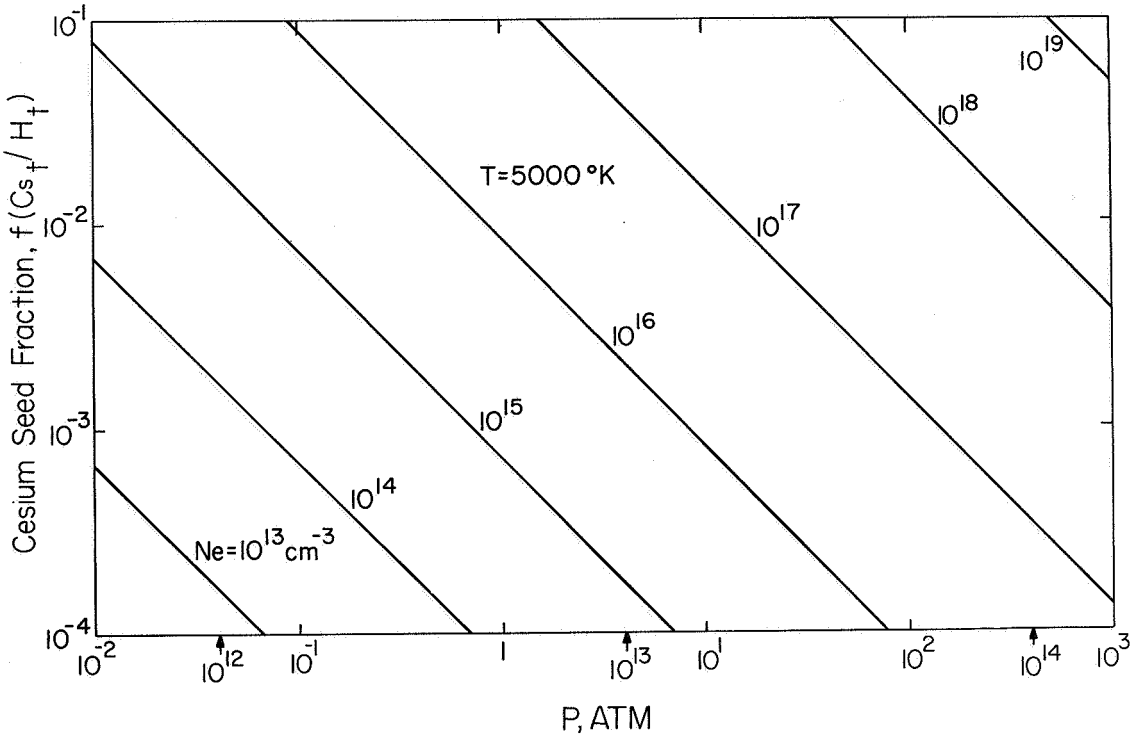

FIG. 1 Electron density in a cesium-hydrogen plasma at 5000°K as a function of cesium seeding. The ratio of Cs particles (atoms plus ions) to hydrogen particles (atoms plus ions) is plotted vs the total pressure of monatomic species and electrons. The electron density in a pure hydrogen plasma is indicated by the arrows.

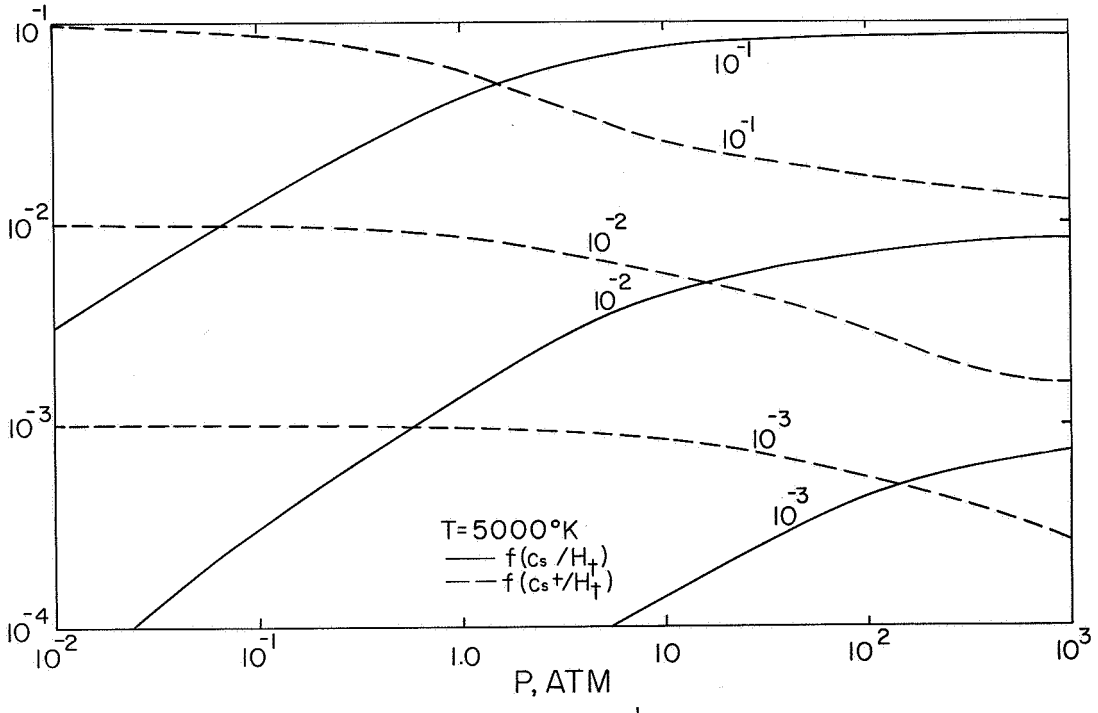

FIG. 2 The ratio of Cs atoms and of Cs^+ ions to hydrogen particles (atoms and ions) vs total pressure at 5000°K for seed fractions $f(Cs_t/H_t)$ of 10^{-1}, 10^{-2} and 10^{-3}.

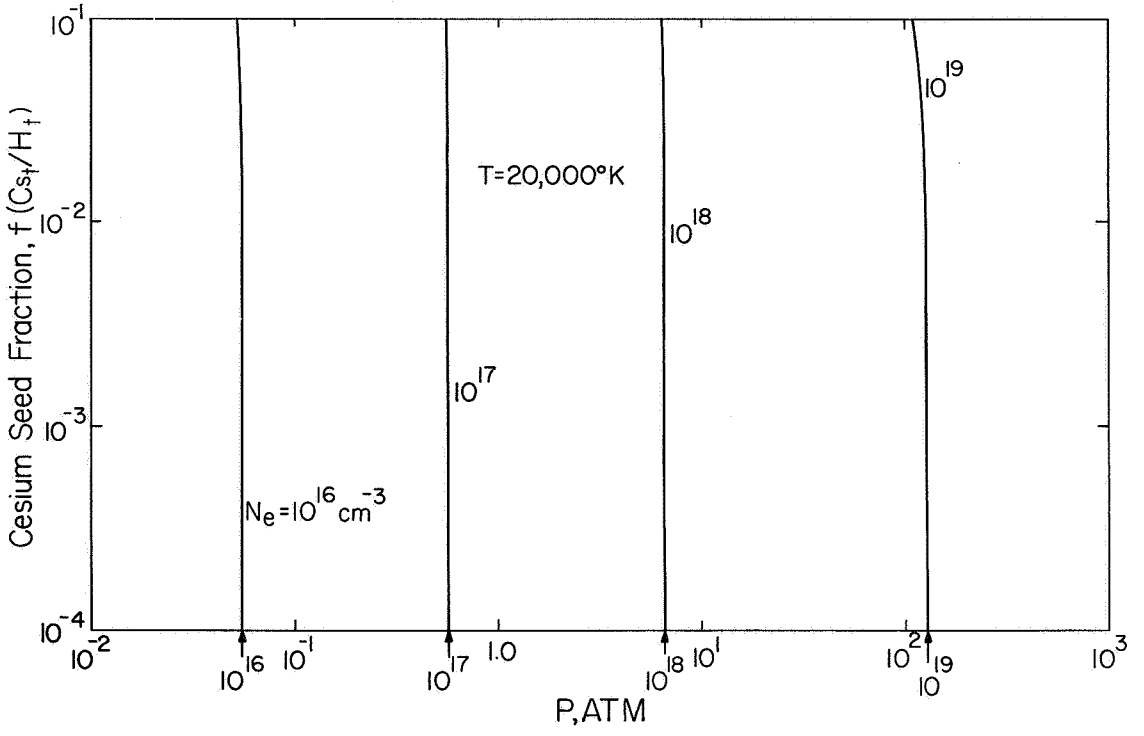

FIG. 3 Electron density in a cesium-hydrogen plasma at 20,000°K. Nomenclature is the same as Fig. 1.

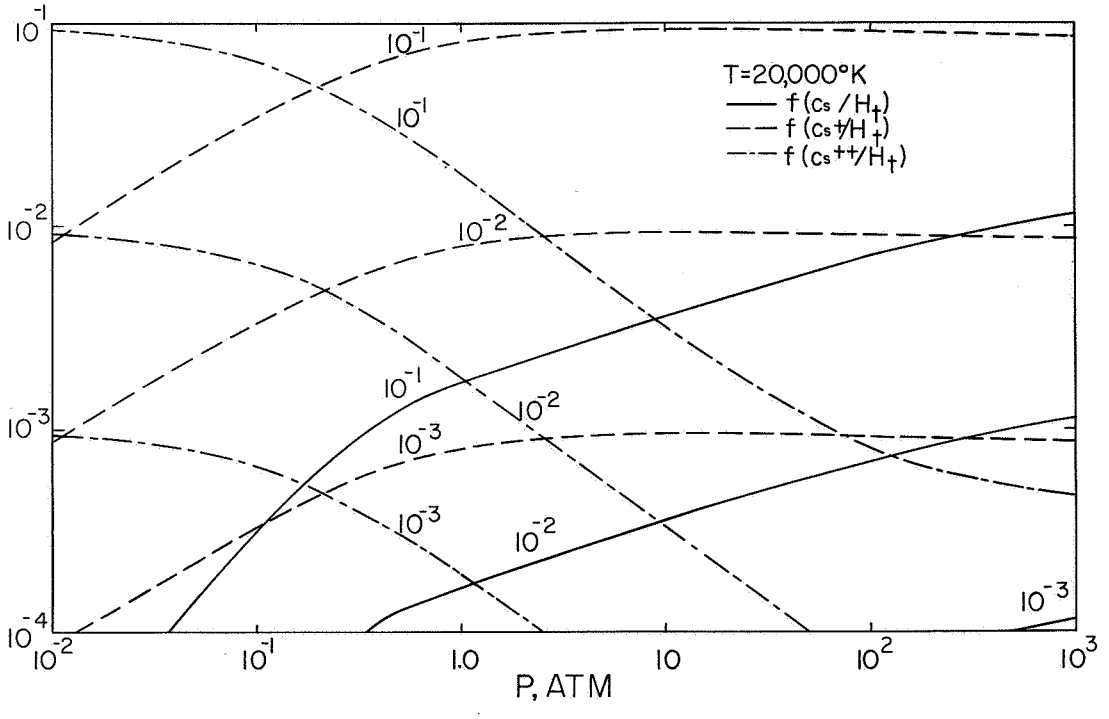

FIG. 4 Ratio of Cs atoms and of Cs^+ ions to hydrogen particles (atoms and ions) at 20,000°K. Nomenclature is the same as Fig. 2.

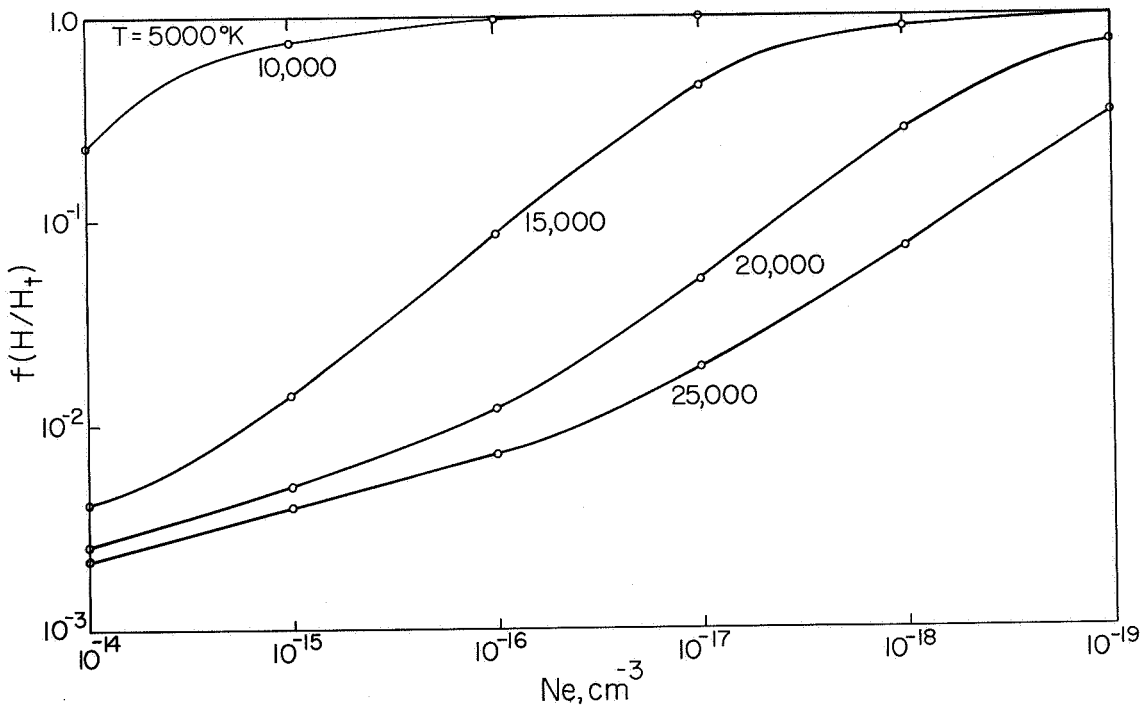

FIG. 5 The degree of ionization of hydrogen (H/H_t) vs electron density. This quantity is essentially independent of cesium seed fraction.

free-free transitions are again characterized by a continuous contribution to the absorption coefficient.

The absorption calculation performed includes bound-bound (line absorption), bound-free (photoionization) and free-free transitions (inverse Bremsstrahlung).

The absorption coefficient, cm^{-1}, can be written

$$k(\nu,T) = \sum_{i,j} \frac{h\nu_{ij}}{4\pi} N_i B_{ij} S_{ij}(\nu) + \sum_{i} N_i \sigma_{ie}(\nu,T) + N_e \sigma_{ee}(\nu,T) \qquad (1)$$

where the three terms represent bound-bound, bound-free and free-free absorption, respectively. B_{ij} is the Einstein absorption coefficient (cm^2/erg-sec), S_{ij} is the line shape (sec) for transitions from level i to level j. N_i is the population density of level i (cm^{-3}), N_e is the electron density, and the σ's are cross sections (cm^2). The summations are over all bound levels.

The species H, Cs^+ and Cs^{++} have absorption lines for photons in the region being considered. The only hydrogen absorption lines which need be considered are the Lyman series. The absorption oscillator strengths needed to compute the B_{ij} for hydrogen are well known (Ref. 5).

The constituent calculations reveal that there are few or no excited Cs^+ or Cs^{++} ions for the conditions of interest. Hence, line absorption by any but the ground states of these two ions can be neglected. Approximate oscillator strength values for Cs^+ were obtained for this work from Coulomb approximation techniques (Ref. 6). Reliable calculations of oscillator strengths or line shapes cannot be made for Cs^{++} because the energy level structure is not well enough known. Hence, line absorption was neglected.

Exact theoretical expressions are available for the bound-free absorption cross section of hydrogen (Ref. 7). Excited states will contribute negligibly, except at high temperatures where they are significantly populated. Their thresholds for photoionization are at or below 3.2 eV.

Theoretical values for the photoionization cross sections of Cs are available from previous work (Ref. 8). Only the ground and first two excited states are expected to contribute significantly. Thresholds are at 3.89 eV, 2.46 eV and 2.09 eV. Photoionization of Cs^+ can be neglected, since the threshold for the ground state is above 25 eV, and the population of the first excited state (threshold 11.6 eV) is extremely low under these conditions.

The contribution to the absorption coefficient from free-free transitions in the fields of the three ionic species H^+, Cs^+ and Cs^{++} can be computed from available formulae (modified hydrogenic formulae) (Ref. 9).

Calculations of the absorption coefficient for the cases shown in Table I were performed. A sampling of the results is presented in the sections to follow and is discussed in Appendix B.

2. Free-Free Absorption Coefficient

An electron of positive energy moving in a continuum state in some atomic potential can make a transition to a higher energy continuum state while absorbing a photon. There is no threshold for this process, so that the absorption is continuous across any energy range of radiation. The photon absorption cross section σ_{ee} can be derived from the related expression for Bremsstrahlung.

The free-free absorption coefficient (Ref. 2), allowing for stimulated emission from higher levels, is, in cm^{-1}

FF(CS/H) = 10^{-3}

log 10 N_e / T(K°)	15	16	17	18	19
5000	0.70	7.76	135		
6000	0.826	8.55	103		
7000	0.781	9.57	107		
8000	0.192	7.43	111		
9000		2.0	81.2		
10,000		0.405	29.1		
11,000		0.118	8.16		
12,000			2.73	187	
14,000			0.736	33.9	
16,000			0.521	11.7	
18,000			0.52	7.33	223
20,000			0.56	6.49	129
	15	16	17	18	19

FF(CS/H) = 10^{-2}

log 10 N_e / T(K°)	15	16	17	18	19
5000	0.0712	0.79	13.6		
6000	0.0845	0.87	10.5	183	
7000	0.0960	0.996	10.9	148	
8000	0.0763	1.08	11.9	143	
9000		0.837	12.5	148	
10,000		0.329	10.5	150	
11,000		0.113	5.68	134	
12,000			2.45	99.2	
14,000			0.727	30.2	
16,000			0.52	11.4	
18,000			0.52	7.29	212
20,000			0.559	6.48	127
	15	16	17	18	19

FF(CS/H) = 10^{-1}

log 10 N_e / T(K°)	15	16	17	18	19
5000		0.0921	1.55	42.8	
6000		0.102	1.21	20.7	
7000		0.117	1.28	17.0	
8000		0.133	1.40	16.6	
9000		0.143	1.54	17.3	
10,000		0.127	1.65	18.4	
11,000		0.0827	1.60	18.9	
12,000		0.0535	1.29	20.0	
14,000			0.661	15.8	
16,000			0.511	9.60	
18,000			0.516	6.96	152
20,000			0.551	6.37	111
	15	16	17	18	19

TABLE I

Total Pressure in Atmospheres for Cases Investigated (Cesium-hydrogen plasma characterized by seed fraction, electron density and temperature; all pressures in atmospheres.)

$$K_{ff}(\nu,T) = \frac{4\pi}{3\sqrt{3}} \left(\frac{2m}{\pi k}\right)^{1/2} \frac{e^6}{hcm^2} [1 - \exp(-h\nu/kT)] \frac{Z^2 g}{T^{1/2}} \frac{N_e N_i}{\nu^3} \qquad (2)$$

where $h\nu$ is the photon energy, T is the temperature in degrees Kelvin, Z is the effective charge on the ion, g is the Gaunt factor, and N_e and N_i are the electron and ion densities, respectively. This equation can be used for Cs^+ (Z=1), Cs^{++} (Z=2) and H^+ (Z=1) with N_e equal to the total electron density and N_i equal to the ion density of the particular species. The Gaunt factor can be set equal to 1.1 over the range of photon energies (4 - 25 eV) and temperatures ($5{,}000^0$ - $20{,}000^0$K) which we are considering for all three species (Ref. 10). These three ionic species are the only ones of importance for the parameters we are using.

No distinction is made in Eq. (2) between cesium and hydrogen ions. Such treatment is valid as long as the free electron does not pass so close to the cesium ion that it penetrates the core. These very close encounters are associated with large photon energies and are not treated well by Eq. (2). At the densities and photon energy range considered here, however, this approximation is sufficiently accurate. The effect is that the free-free absorption coefficient depends only on electron density and not explicitly on seed fraction. Of course the electron density depends on seed fraction.

Three representative curves of absorption coefficient vs photon energy $h\nu$ (eV) are found in Figs. 6, 7 and 8. The curves and numerical computer outputs give $K(cm^{-1})$ as a function of the plasma parameters; explicitly

(1) FF → cesium-hydrogen seeding fraction.

(2) T → plasma temperatures (^{0}K)

(3) DEN → electron density (cm^{-3}).

FF= 1.0000000E-02 T= 0.5000000E+04 DEN= 1.0000000E+17

e V	K(cm^{-1})
0.4000000E+01	0.6348003E-04
0.4500000E+01	0.4458690E-04
0.5000000E+01	0.3250450E-04
0.5500000E+01	0.2442126E-04
0.6000000E+01	0.1881063E-04
0.6500000E+01	0.1479508E-04
0.7000000E+01	0.1184577E-04
0.7500000E+01	0.9631050E-05
0.8000000E+01	0.7935741E-05
0.8500000E+01	0.6616079E-05
0.9000000E+01	0.5573525E-05
0.9500000E+01	0.4739000E-05
0.1000000E+02	0.4063099E-05
0.1050000E+02	0.3509858E-05
0.1100000E+02	0.3052667E-05
0.1150000E+02	0.2671554E-05
0.1200000E+02	0.2351331E-05
0.1250000E+02	0.2080307E-05
0.1300000E+02	0.1849385E-05
0.1350000E+02	0.1651415E-05
0.1400000E+02	0.1480721E-05
0.1450000E+02	0.1332765E-05
0.1500000E+02	0.1203881E-05
0.1550000E+02	0.1091094E-05
0.1600000E+02	0.9919676E-06
0.1650000E+02	0.9044939E-06
0.1700000E+02	0.8270099E-06
0.1750000E+02	0.7581294E-06
0.1800000E+02	0.6966906E-06
0.1850000E+02	0.6417151E-06
0.1900000E+02	0.5923750E-06
0.1950000E+02	0.5479660E-06
0.2000000E+02	0.5078874E-06
0.2050000E+02	0.4716240E-06
0.2100000E+02	0.4387323E-06
0.2150000E+02	0.4088294E-06
0.2200000E+02	0.3815834E-06
0.2250000E+02	0.3567056E-06
0.2300000E+02	0.3339442E-06
0.2350000E+02	0.3130790E-06
0.2400000E+02	0.2939163E-06
0.2450000E+02	0.2762862E-06
0.2500000E+02	0.2600384E-06

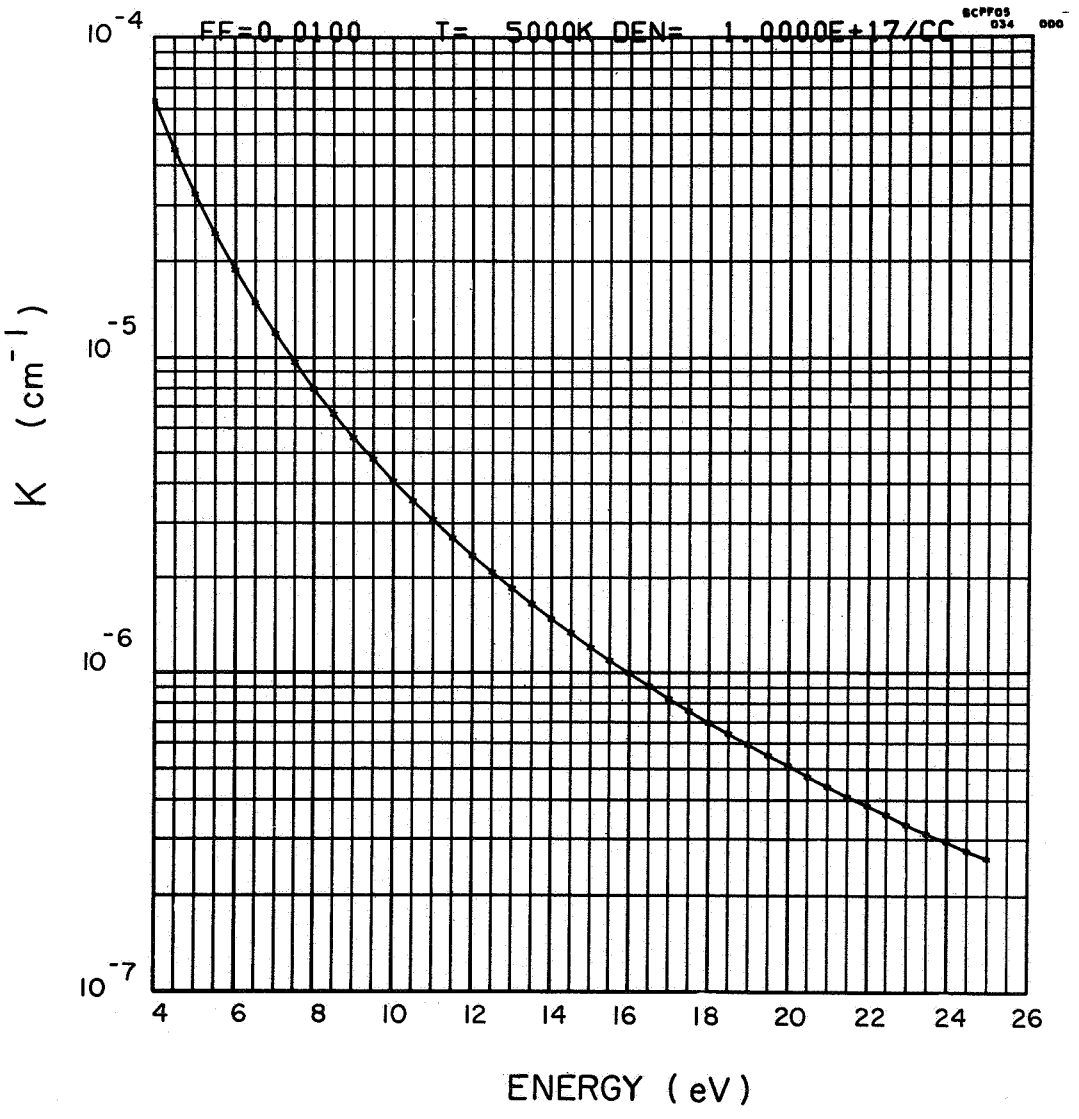

FIG. 6 Free-free absorption coefficient for a cesium-hydrogen ratio of 10^{-2}, electron density 10^{17} and temperature 5000^{0}K.

FF= 1.0000000E-02 T= 0.1200000E+05 DEN= 1.0000000E+17

e V	K(cm^{-1})
0.4000000E+01	0.4012369E-04
0.4500000E+01	0.2841076E-04
0.5000000E+01	0.2081510E-04
0.5500000E+01	0.1568672E-04
0.6000000E+01	0.1210558E-04
0.6500000E+01	0.9532427E-05
0.7000000E+01	0.7637656E-05
0.7500000E+01	0.6212435E-05
0.8000000E+01	0.5120280E-05
0.8500000E+01	0.4269526E-05
0.9000000E+01	0.3597110E-05
0.9500000E+01	0.3058709E-05
0.1000000E+02	0.2622563E-05
0.1050000E+02	0.2265523E-05
0.1100000E+02	0.1970448E-05
0.1150000E+02	0.1724461E-05
0.1200000E+02	0.1517769E-05
0.1250000E+02	0.1342830E-05
0.1300000E+02	0.1193773E-05
0.1350000E+02	0.1065985E-05
0.1400000E+02	0.9558037E-06
0.1450000E+02	0.8602982E-06
0.1500000E+02	0.7771044E-06
0.1550000E+02	0.7043007E-06
0.1600000E+02	0.6403145E-06
0.1650000E+02	0.5838503E-06
0.1700000E+02	0.5338344E-06
0.1750000E+02	0.4893721E-06
0.1800000E+02	0.4497134E-06
0.1850000E+02	0.4142268E-06
0.1900000E+02	0.3823777E-06
0.1950000E+02	0.3537118E-06
0.2000000E+02	0.3278411E-06
0.2050000E+02	0.3044330E-06
0.2100000E+02	0.2832015E-06
0.2150000E+02	0.2638991E-06
0.2200000E+02	0.2463119E-06
0.2250000E+02	0.2302533E-06
0.2300000E+02	0.2155608E-06
0.2350000E+02	0.2020923E-06
0.2400000E+02	0.1897228E-06
0.2450000E+02	0.1783426E-06
0.2500000E+02	0.1678546E-06

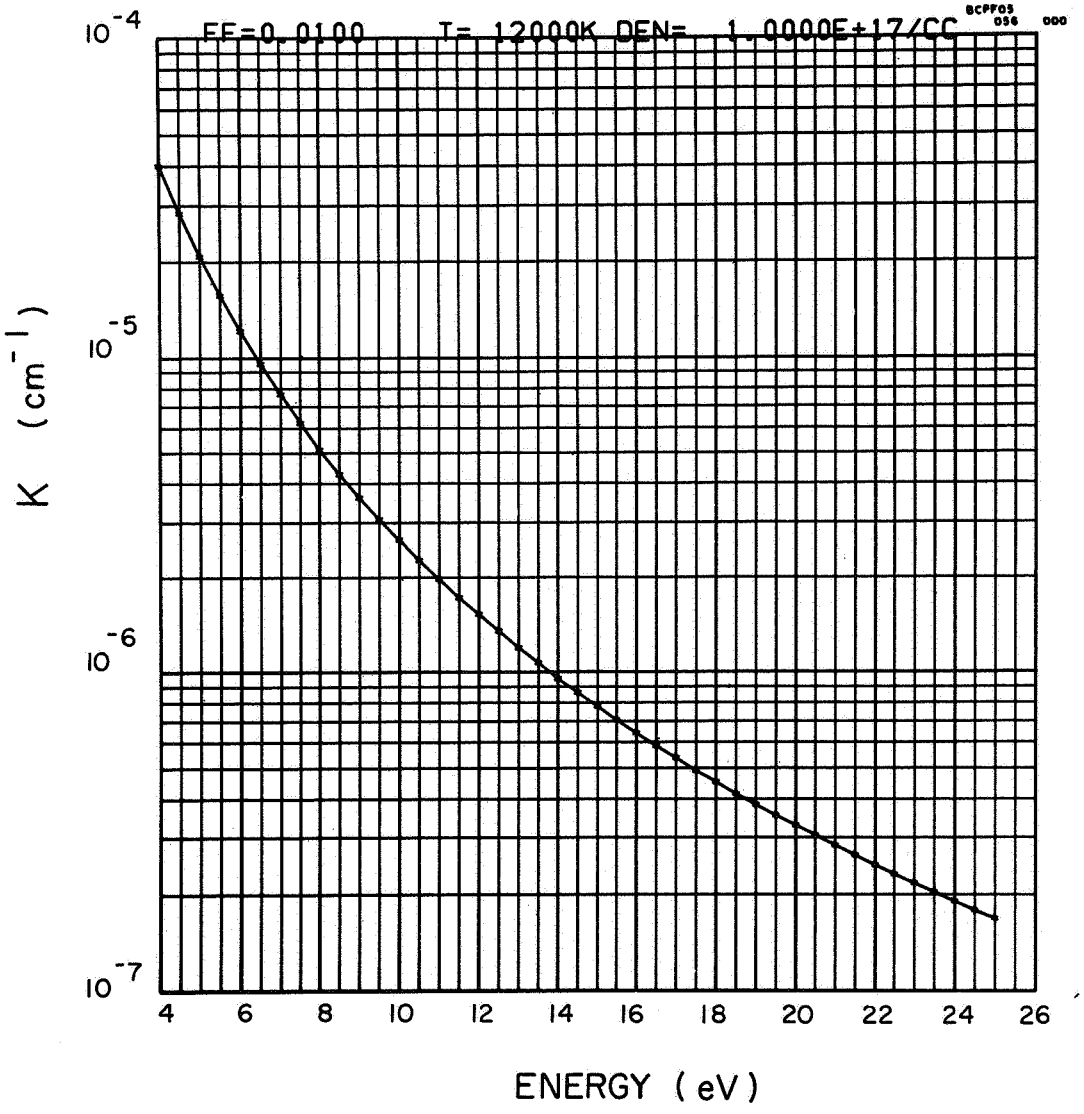

FIG. 7 Free-free absorption coefficient for a cesium-hydrogen ratio of 10^{-2}, electron density $10^{17}/cm^3$ and temperature 12,000°K.

FF= 1.0000000E-02 T= 0.2000000E+05 DEN= 1.0000000E+17

e V	K(cm^{-1})
0.4000000E+01	0.2879344E-04
0.4500000E+01	0.2077702E-04
0.5000000E+01	0.1544887E-04
0.5500000E+01	0.1177697E-04
0.6000000E+01	0.9169232E-05
0.6500000E+01	0.7269501E-05
0.7000000E+01	0.5854906E-05
0.7500000E+01	0.4781263E-05
0.8000000E+01	0.3952591E-05
0.8500000E+01	0.3303379E-05
0.9000000E+01	0.2787928E-05
0.9500000E+01	0.2373730E-05
0.1000000E+02	0.2037255E-05
0.1050000E+02	0.1761200E-05
0.1100000E+02	0.1532662E-05
0.1150000E+02	0.1341887E-05
0.1200000E+02	0.1181420E-05
0.1250000E+02	0.1045494E-05
0.1300000E+02	0.9296065E-06
0.1350000E+02	0.8302061E-06
0.1400000E+02	0.7444688E-06
0.1450000E+02	0.6701300E-06
0.1500000E+02	0.6053597E-06
0.1550000E+02	0.5486690E-06
0.1600000E+02	0.4988375E-06
0.1650000E+02	0.4548596E-06
0.1700000E+02	0.4159011E-06
0.1750000E+02	0.3812663E-06
0.1800000E+02	0.3503719E-06
0.1850000E+02	0.3227266E-06
0.1900000E+02	0.2979145E-06
0.1950000E+02	0.2755817E-06
0.2000000E+02	0.2554262E-06
0.2050000E+02	0.2371892E-06
0.2100000E+02	0.2206477E-06
0.2150000E+02	0.2056091E-06
0.2200000E+02	0.1919067E-06
0.2250000E+02	0.1793953E-06
0.2300000E+02	0.1679482E-06
0.2350000E+02	0.1574546E-06
0.2400000E+02	0.1478173E-06
0.2450000E+02	0.1389508E-06
0.2500000E+02	0.1307794E-06

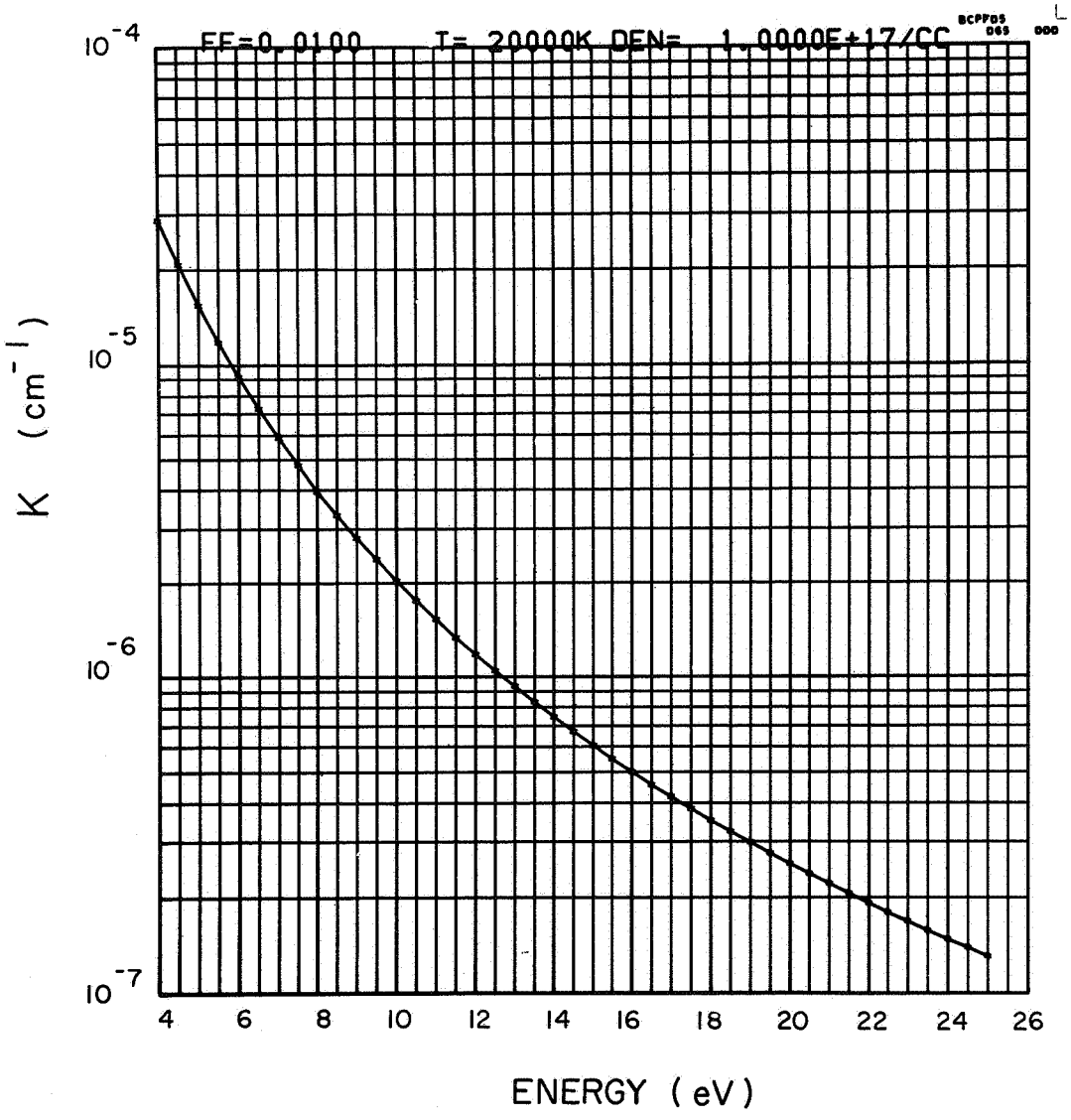

FIG. 8 Free-free absorption coefficient for a cesium-hydrogen ratio of 10^{-2}, electron density $10^{17}/cm^3$ and temperature 20,000°K.

Figure 9 is a master curve for an electron density of $DEN = 10^{17}$ cm^{-3}. To obtain values of $K(\nu,T)$ for any other density, one takes the value from Fig. 9 using the same temperature and multiplies all K values by the ratio $(DEN^2/10^{34})$. A more detailed discussion of these results is available (Ref. 11).

3. Bound-Free Absorption Coefficient

For calculations of the photoionization cross section σ_{ie} we use the phase shifted Coulomb approximation of Burgess and Seaton (Ref. 12). The equation for the cross section for ionization of a level with effective quantum numbers $\eta\ell$ is

$$\sigma_{\eta\ell}(\gamma') = 4\pi^2\alpha\, a_o^2 \sum_{\ell'=\ell\pm1} \frac{df}{d\epsilon'}(\eta,\ell;\gamma',\ell') \text{ cm}^2 \quad , \tag{3}$$

where α is the fine structure constant and a_o is the Bohr radius. The differential oscillator strength is defined by

$$\frac{df}{d\epsilon'} = \frac{1}{3\pi}(h\nu)\frac{\ell>}{2\ell+1}\left|\langle\eta,\ell|r|\gamma',\ell'\rangle\right|^2 \tag{4}$$

where η and γ' are the effective quantum numbers of the initial (bound) and final (free) states in the transition, respectively, given by

$$\begin{aligned} E_{\eta\ell} &= 1/\eta^2 \\ \epsilon' &= 1/\gamma'^2 \end{aligned} \tag{5}$$

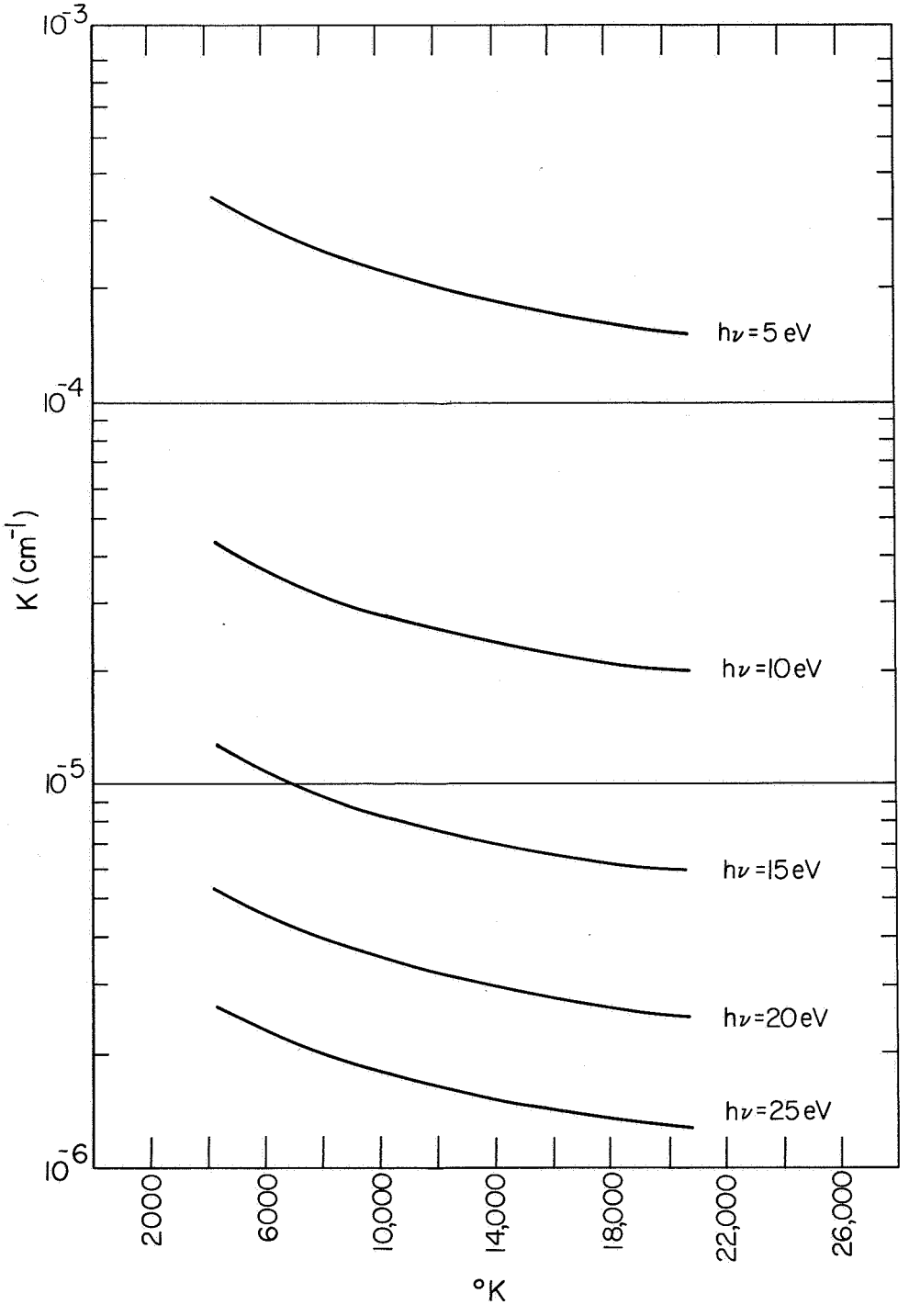

FIG. 9 Free-free absorption coefficient vs temperature at an electron density of $10^{17}/cm^3$.

The numbers ℓ and ℓ' are the angular momentum quantum numbers of the initial and final states, respectively. The term $\ell>$ is the larger of ℓ and ℓ'. The squares of the matrix elements have been formulated using the adjusted quantum defect method of Norcross and Stone (Ref. 8).

For the problem being considered, there are five bound levels which contribute significantly to the photoionization (see Table II).

Other bound levels do not absorb in the 4 eV - 25 eV range or are populated too little to give significant absorption. Their neglect is discussed in the previous quarterly progress reports issued under this contract. For the hydrogen states the calculation of the cross section is simplified due to the tables of Burgess (Ref. 13), which make available much of the necessary data in tabular form. For cesium we have used the formulation of Burgess and Seaton discussed above. The cross sections obtained are multiplied by the population density of the levels involved in order to obtain the absorption coefficient.

The cross sections of Table II are shown in Fig. 10 and the corresponding numerical values are presented for reference in Table III. Figures 11, 12 and 13 show the variations of the bound-free absorption coefficients as functions of the three independent parameter electron density, temperature, and cesium seed fraction.

4. Bound-Bound Absorption Coefficient

The linear absorption coefficient K_{12} related to the absorption of a photon of energy $h\nu$, corresponding to the atomic system going from a bound state (1) to a higher energy bound state (2), is given by

$$K_{12}(\nu) = \frac{h\nu}{4\pi} N_1 B_{12} S_{12}(\nu) \qquad (6)$$

TABLE II

Bound Levels of Cesium and Hydrogen

Element	States	η	Binding Energy
Cesium	$5^2D_{3/2}, 5^2D_{5/2}$	2.5514	0.15362 Ry
Cesium	$6^2P_{3/2}, 6^2P_{1/2}$	2.34522	0.18181 "
Cesium	$6^2S_{1/2}$	1.86874	0.28636 "
Hydrogen	$2^2S_{1/2}, 2^2P_{1/2}$	2.0	0.250 "
Hydrogen	$1^2S_{1/2}$	1.0	1.0 "

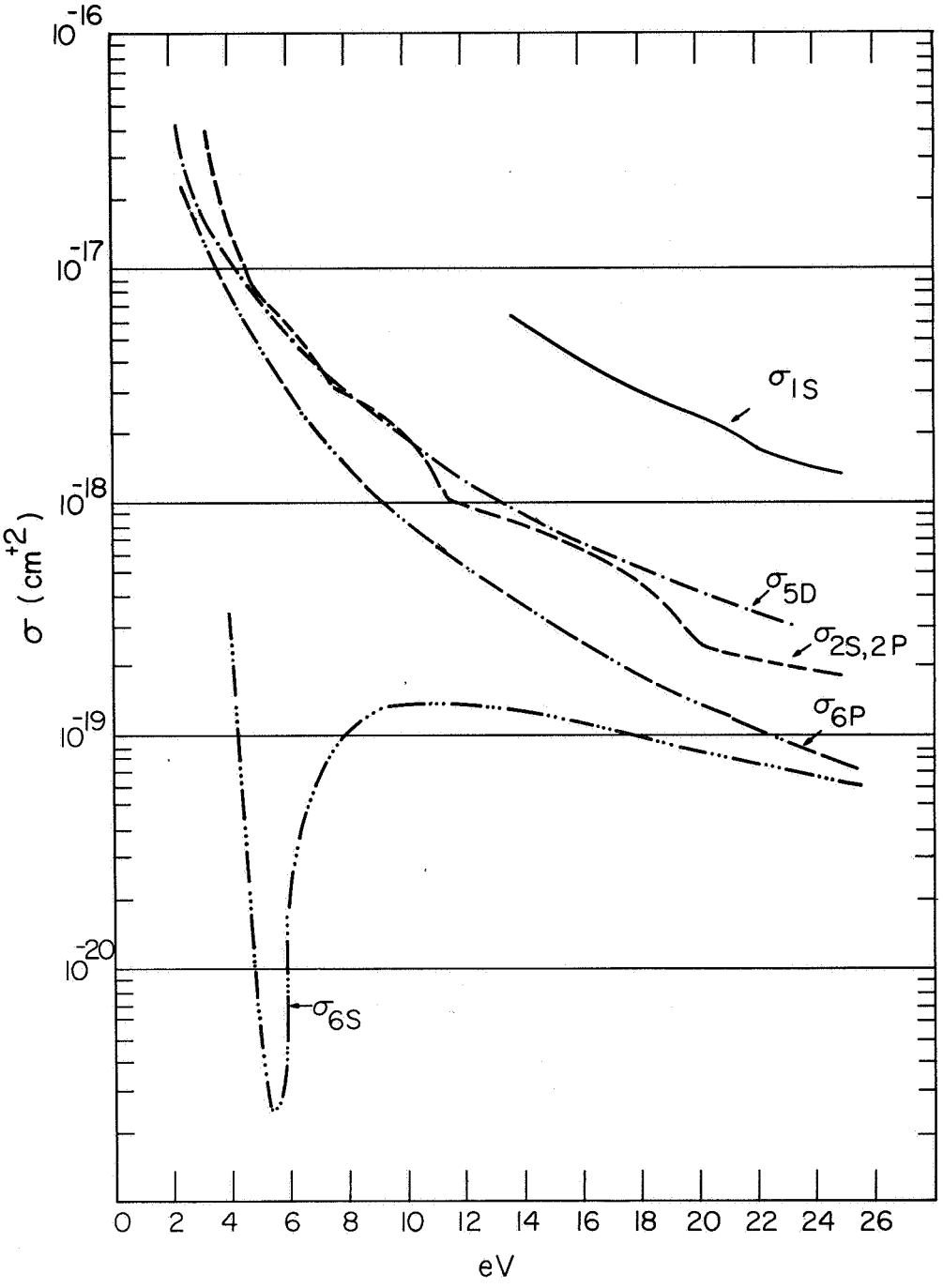

FIG. 10 Photoionization cross sections for the bound levels of cesium and hydrogen shown in Table II.

TABLE III

Numerical Values for the Photoionization Cross Sections Shown in Fig. 10

SIGMA 5D	SIGMA 6P	SIGMA 2S,2P	SIGMA 6S	SIGMA 1S	E.V.
0.4233000E-16	0.2261130E-16	0.3571647E-16	0.3440240E-18	0.6304135E-17	
0.0000000E-38	0.0000000E-38	0.0000000E-38	0.0000000E-38	0.0000000E-38	2.0
0.3299777E-16	0.2196461E-16	0.0000000E-38	0.0000000E-38	0.0000000E-38	2.5
0.2467600E-16	0.1531028E-16	0.0000000E-38	0.0000000E-38	0.0000000E-38	3.0
0.1883925E-16	0.1106217E-16	0.2630631E-16	0.0000000E-38	0.0000000E-38	3.5
0.1468902E-16	0.8236509E-17	0.1880634E-16	0.2687584E-18	0.0000000E-38	4.0
0.1167674E-16	0.6289738E-17	0.1382692E-16	0.6789672E-19	0.0000000E-38	4.5
0.9443765E-17	0.4907686E-17	0.1107899E-16	0.6291880E-20	0.0000000E-38	5.0
0.7755334E-17	0.3900977E-17	0.8331060E-17	0.2521060E-20	0.0000000E-38	5.5
0.6455387E-17	0.3151164E-17	0.7023952E-17	0.2069497E-19	0.0000000E-38	6.0
0.5438105E-17	0.2581718E-17	0.5971171E-17	0.4496338E-19	0.0000000E-38	6.5
0.4630276E-17	0.2141775E-17	0.4918391E-17	0.6855907E-19	0.0000000E-38	7.0
0.3980259E-17	0.1796673E-17	0.3865610E-17	0.8888265E-19	0.0000000E-38	7.5
0.3450961E-17	0.1522262E-17	0.3204763E-17	0.1052309E-18	0.0000000E-38	8.0
0.3015292E-17	0.1301377E-17	0.2937838E-17	0.1177308E-18	0.0000000E-38	8.5
0.2653163E-17	0.1121605E-17	0.2670913E-17	0.1268319E-18	0.0000000E-38	9.0
0.2349462E-17	0.9738176E-18	0.2403988E-17	0.1330734E-18	0.0000000E-38	9.5
0.2092674E-17	0.8512090E-18	0.2137063E-17	0.1369777E-18	0.0000000E-38	10.0
0.1873919E-17	0.7486336E-18	0.1870138E-17	0.1390106E-18	0.0000000E-38	10.5
0.1686277E-17	0.6621559E-18	0.1603213E-17	0.1395670E-18	0.0000000E-38	11.0
0.1524293E-17	0.5887306E-18	0.1336288E-17	0.1389754E-18	0.0000000E-38	11.5
0.1383634E-17	0.5259774E-18	0.1069363E-17	0.1375025E-18	0.0000000E-38	12.0
0.1260823E-17	0.4720181E-18	0.9790385E-18	0.1353639E-18	0.0000000E-38	12.5
0.1153049E-17	0.4253574E-18	0.9338978E-18	0.1327316E-18	0.0000000E-38	13.0
0.1058021E-17	0.3847950E-18	0.8887570E-18	0.1297427E-18	0.0000000E-38	13.5
0.9738599E-18	0.3493599E-18	0.8436162E-18	0.1265055E-18	0.5834342E-17	14.0
0.8990137E-18	0.3182610E-18	0.7984754E-18	0.1231052E-18	0.5316688E-17	14.5
0.8321921E-18	0.2908498E-18	0.7533346E-18	0.1196088E-18	0.4870306E-17	15.0
0.7723163E-18	0.2665905E-18	0.7081938E-18	0.1160682E-18	0.4456937E-17	15.5
0.7184796E-18	0.2450387E-18	0.6630531E-18	0.1125236E-18	0.4100198E-17	16.0
0.6699155E-18	0.2258230E-18	0.6179123E-18	0.1090061E-18	0.3811682E-17	16.5
0.6259738E-18	0.2086319E-18	0.5727715E-18	0.1055390E-18	0.3523166E-17	17.0
0.5860988E-18	0.1932026E-18	0.5276307E-18	0.1021398E-18	0.3234650E-17	17.5
0.5498152E-18	0.1793122E-18	0.4824899E-18	0.9882134E-19	0.2959844E-17	18.0
0.5167133E-18	0.1667711E-18	0.4373491E-18	0.9559266E-19	0.2805308E-17	18.5
0.4864397E-18	0.1554172E-18	0.3922084E-18	0.9245993E-19	0.2650772E-17	19.0
0.4586877E-18	0.1451113E-18	0.3470676E-18	0.8942702E-19	0.2496236E-17	19.5
0.4331906E-18	0.1357333E-18	0.3019268E-18	0.8649600E-19	0.2341700E-17	20.0
0.4097151E-18	0.1271795E-18	0.2567860E-18	0.8366748E-19	0.2187164E-17	20.5
0.3880571E-18	0.1193599E-18	0.2271906E-18	0.8094110E-19	0.2032627E-17	21.0
0.3680372E-18	0.1121962E-18	0.2217729E-18	0.7831552E-19	0.1878091E-17	21.5
0.3494974E-18	0.1056197E-18	0.2163552E-18	0.7578888E-19	0.1723555E-17	22.0
0.3322977E-18	0.9957039E-19	0.2109375E-18	0.7335883E-19	0.1608053E-17	22.5
0.3163142E-18	0.9399561E-19	0.2055198E-18	0.7102266E-19	0.1551134E-17	23.0
0.3014370E-18	0.8884880E-19	0.2001021E-18	0.6877755E-19	0.1494216E-17	23.5
0.2875677E-18	0.8408888E-19	0.1946844E-18	0.6662026E-19	0.1437297E-17	24.0
0.2746190E-18	0.7967949E-19	0.1892667E-18	0.6454779E-19	0.1380378E-17	24.5
0.2625123E-18	0.7558827E-19	0.1838490E-18	0.6255687E-19	0.1323459E-17	25.0

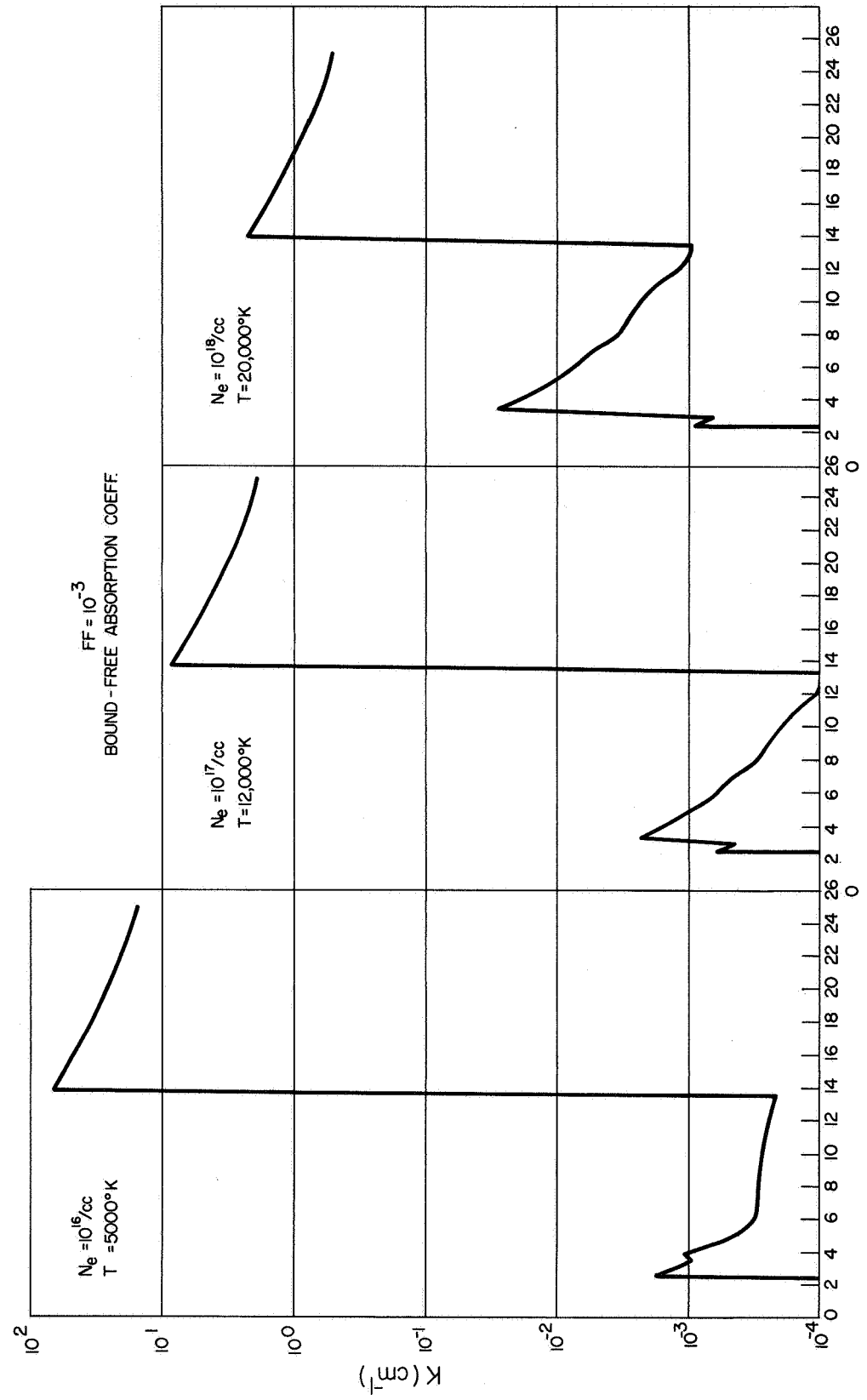

FIG. 11 Bound-free absorption coefficients vs photon energy for a cesium-hydrogen plasma with a seed fraction of 10^{-3}, temperature and electron density parameters as shown.

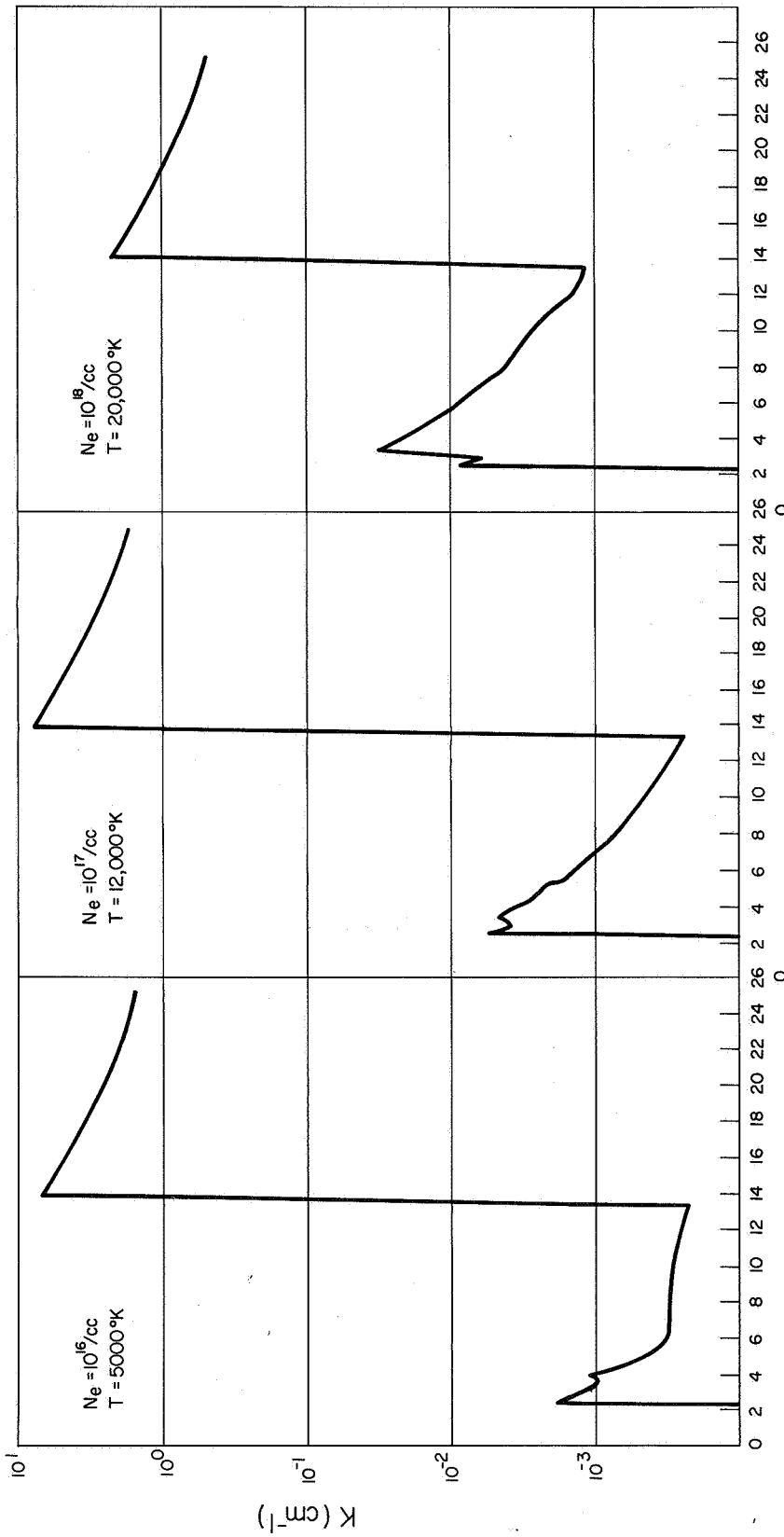

FIG. 12 Bound-free absorption coefficients vs photon energy for a cesium-hydrogen plasma with a seed fraction of 10^{-2}, temperature and electron density parameters as shown.

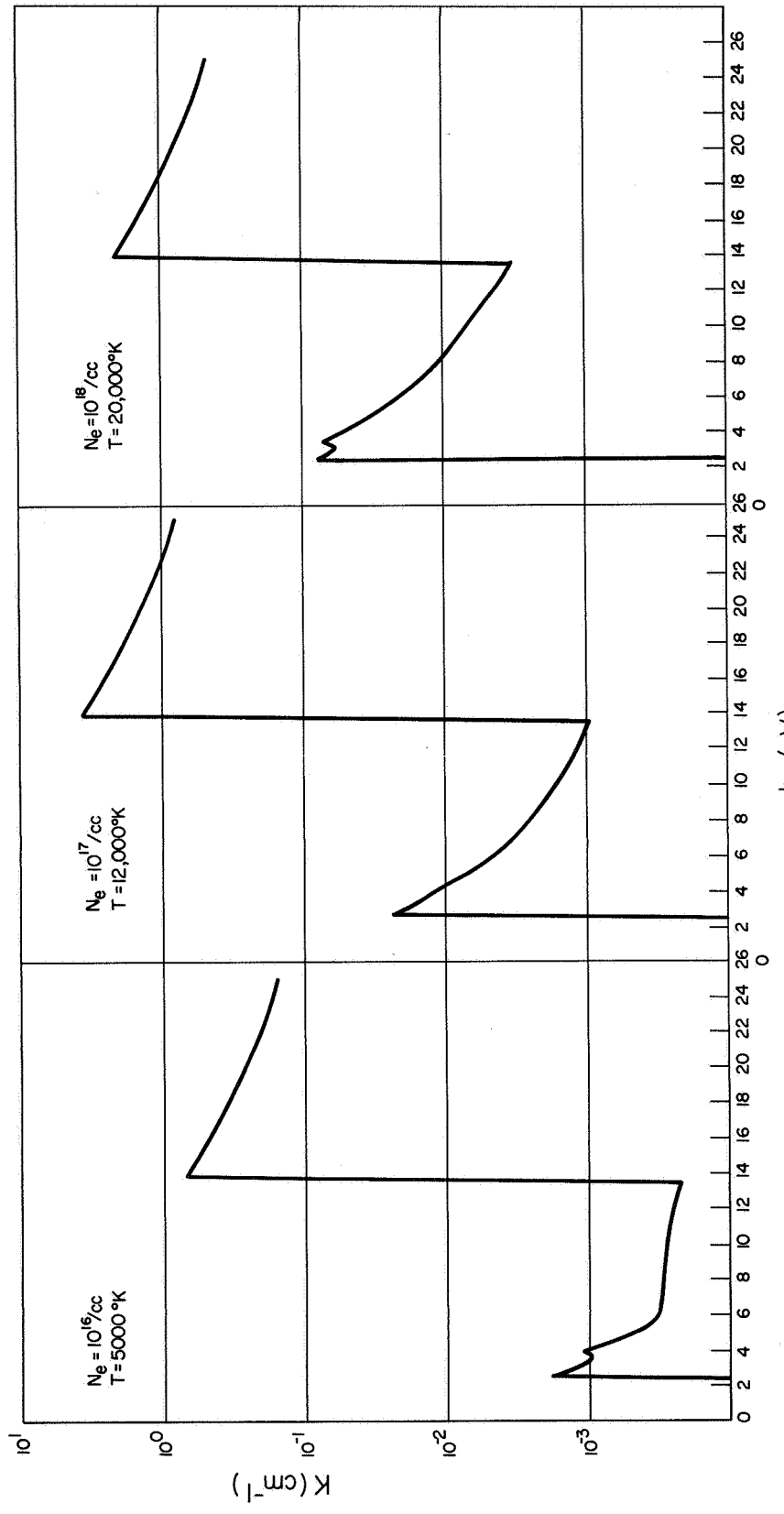

FIG. 13 Bound-free absorption coefficients vs photon energy for a cesium-hydrogen plasma with a seed fraction of 10^{-1}, temperature and electron density parameters as shown.

where N_1 is the density of absorbing atomic systems in state 1, c is the velocity of light, B_{12} is the Einstein induced absorption coefficient, and $S_{12}(\nu)$ is the line shape, defined by

$$\int_{-\infty}^{\infty} S(\nu)\, d\nu = 1 \quad . \tag{7}$$

Since we are concerned with the total absorption coefficient over some $\Delta(h\nu)$ interval in which this line falls, we define an average absorption coefficient

$$\overline{K_{12}(\nu)} = \frac{1}{\Delta(h\nu)} \int_{-h\nu/2}^{h\nu/2} K_{12}(\nu)\, d(h\nu) \approx \frac{1}{\Delta(h\nu)} \int_{-\infty}^{\infty} K_{12}(\nu)\, d(h\nu) = \frac{h}{\Delta(h\nu)} \frac{h\nu}{4\pi} N_1 B_{12} \tag{8}$$

Using the relationship between the Einstein coefficient and the absorption oscillator strength

$$B_{12} = \frac{e^2}{m} \frac{4\pi^2}{h\nu c} f_{12} \tag{9}$$

we get the result

$$\overline{K_{12}(\nu)} = \frac{h}{\Delta(h\nu)} \frac{\pi e^2}{mc} N_1 f_{12} \tag{10}$$

The evaluation of the absorption coefficient for the bound-bound transitions therefore reduces to knowing the oscillator strengths f_{ij} for the levels which contribute significantly for our range of parameters. The population densities N_i are, of course, known from previous calculation.

In our case we need consider only the Lyman series for hydrogen and the Cs^+ $(5p^6)$ term in cesium. (A full discussion of this conclusion will be found in Quarterly Progress Report No. 5, included as Appendix B.)

The absorption oscillator strength for discrete transitions between energy states with principal quantum numbers n and n' can be calculated exactly for the hydrogen atom. The formula is

$$f_{ij} = \frac{64}{3\sqrt{3\pi}} \frac{1}{g_n} \frac{1}{\left[(1/n)^2 - (1/n')^2\right]^3} \left| \frac{1}{n^3 n'^3} \right| g \qquad (11)$$

where $g_n = 2n^2$ and the Gaunt factor $g \equiv 1$. These oscillator strengths have been tabulated by Karzas and Latter (Ref. 10). Below 20,000°K only the ground state of Cs^+ $(5p^6\ {}^1S)$ is significantly populated. Photoabsorption in Cs^+ can proceed both by photoexcitation and photoionization, the latter process having a threshold of 25.08 eV. Therefore it will not be considered, as it is outside the context of this report. Our concern with photoabsorption in Cs^+ was therefore limited to obtaining the oscillator strengths for transitions from the ground state.

Accurate oscillator strengths are not yet available in the literature for Cs^+ but fairly reliable values were obtained by using the results of Ref. 6. This work is based on the Coulomb approximation, which is strictly applicable only to the case of a single electron outside a closed shell, but it has been shown to give adequate results in a much wider range of cases (Ref. 6).

The absorption oscillator strength f is related to the line strength S by

$$f = \frac{3.04 \times 10^2}{g\lambda} S \tag{12}$$

where g is the statistical weight of the lower level, the wavelength λ is in Å, and the line strength is in atomic units (a_0^2, e^2). The line strength is given by (Ref. 6)

$$S = \mathcal{S}(M)\mathcal{S}(L)\sigma^2 \tag{13}$$

where $\mathcal{S}(M)$ and $\mathcal{S}(L)$ are functions of the multiplets and lines involved in the transition, respectively. The term σ^2 is given in terms of the larger of the two values of the angular momentum quantum numbers $\ell>$, and radial wave functions of the initial and final states are given by

$$\sigma^2 = \frac{1}{4\ell>^2 - 1} \left\{ \int_0^\infty R_i R_f \, r \, dr \right\}^2 \tag{14}$$

The factors $\mathcal{S}(M)$ and $\mathcal{S}(L)$ take forms determined by the coupling scheme applicable to the atomic system. For Cs^+, the J-L coupling scheme seems to be the most appropriate, since its configuration is that of a rare gas (Ref. 14). These factors have been considered for the rare gases in Ref. 15 and hence can be applied directly here. In the notation of this paper

$$S = \mathcal{S}(M)X(L)\left\{\int_0^\infty R_i R_f \, r \, dr\right\}^2 \tag{15}$$

and

$$X(L) = \frac{3}{4\pi}(2\ell_i + 1)(2\ell_f + 1)\begin{pmatrix} \ell_i & 1 & \ell_f \\ 0 & 0 & 0 \end{pmatrix}^2 \tag{16}$$

where the squared expression is the quantum mechanical 3j symbol. The term $\mathcal{S}(M)$ is given in tabular form in Ref. 15 and σ was obtained from the tables given in Ref. 6.

Since the ground state of Cs^+ has $J=0$, the selection rules of the J-L coupling scheme allow transitions only to states having $J=1$. Transitions to the nearest states have the largest values of "f". We have considered the levels 6S, 5D, 7S and 6D. These levels contain ten states to which transitions are permitted by absorption of photons with energies from 15.2 to 18.9 eV.

In order to compute σ, the effective principal quantum number n^* of the level is needed. It is related to the ionization energy of the level ϵ, in Rydbergs, and the residual charge C on the atom by

$$n^* = C/\epsilon^{1/2} \tag{17}$$

The functions tabulated in Ref. 6 are rather insensitive to n^* so we have made the approximation of using an average n^* for the level, computed by using

$$\bar{\epsilon} = \sum_j (2J + 1)\epsilon / \sum_j (2J + 1) \qquad (18)$$

The results of these computations are shown in Table IV. The energy $h\nu$ is the photon energy required to effect the transition. Required energy level data were taken from Ref. 14. The entries fall into three groups because of the manner in which the calculations were programmed for the computer. The first group is the first fifteen levels of the Lyman hydrogen series. The two smaller groups include all of the Cs^+ lines used in the calculation. By extrapolation it was determined that excitation of the 8S and 7D levels in Cs^+ accounted for a negligible fraction of the photoabsorption. All of the lines shown in Table IV were averaged over a line width of approximately 10 Å, there is a slight variation from one group to another.

The results of these calculations are shown in Figs. 14, 15, and 16. Each figure compares the bound-bound line structure for a constant seed fraction for three values of temperature and density. Two pairs of these lines coincide, i.e., the hydrogen 6P line and one of the Cs^+ 5D lines, both fall at 13.17 eV and the hydrogen 9P line coincides with one of the Cs^+ 6S lines at 13.38 eV. For $FF = 10^{-3}$, 10^{-2} the addition of the Cs^+ absorption does not significantly change the value of the absorption coefficient as calculated for hydrogen alone. For $FF = 10^{-1}$ this still applies for the absorption coefficient at 13.38 eV while now the absorption at 13.17 eV is increased above the solid line value due to hydrogen alone, to the dot (indicated by arrow) because of the contribution of the Cs^+ 5D line. Even here the modification due to the Cs seed is insignificant.

In Fig. 17 we show the results from Figs. 14, 15 and 16 in a different format. For three constant values of density and temperature (corresponding to the values in Figs. 14, 15 and 16) we plot the variation of the individual lines as a function of seed fraction FF.

TABLE IV

Bound-Bound Lines Vs Energy

$h\nu$(eV)	Final State	f_{abs}
10.16	2 P	0.4162
12.04	3 P	0.7910×10^{-1}
12.70	4 P	0.2899×10^{-1}
13.00	5 P	0.1394×10^{-1}
13.17	6 P	0.7799×10^{-2}
13.27	7 P	0.4184×10^{-2}
13.33	8 P	0.3183×10^{-2}
13.38	9 P	0.2216×10^{-2}
13.41	10 P	0.1605×10^{-2}
13.43	11 P	0.1200×10^{-2}
13.45	12 P	0.9214×10^{-3}
13.46	13 P	0.7227×10^{-3}
13.47	14 P	0.5774×10^{-3}
13.48	15 P	0.4686×10^{-3}
13.49	16 P	0.3856×10^{-3}
13.17	5 D	0.1458×10^{-1}
13.38	6 S	0.2382×10^{-2}
13.76	5 D	0.1523×10^{-1}
15.23	6 S	0.2712×10^{-2}
15.33	5 D	0.3394×10^{-1}
18.55	6 D	0.2251×10^{-2}
18.56	7 S	0.4561×10^{-3}
18.57	6 D	0.2289×10^{-2}
20.31	7 S	0.4971×10^{-3}
20.58	6 D	0.5024×10^{-2}

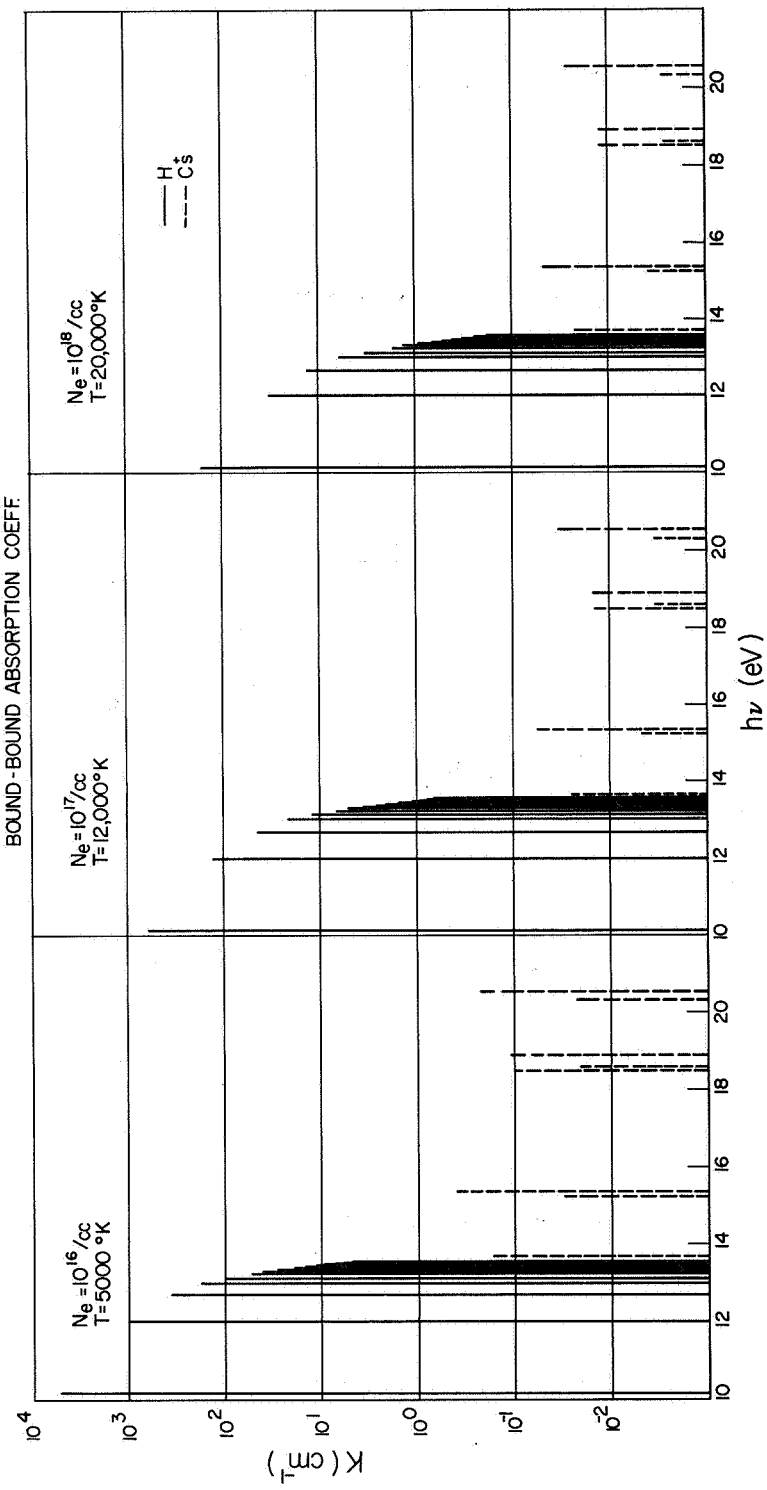

FIG. 14 Bound-bound absorption coefficient vs photon energy for a cesium-hydrogen plasma with a seed fraction of 10^{-3}, temperature and electron density parameters as shown.

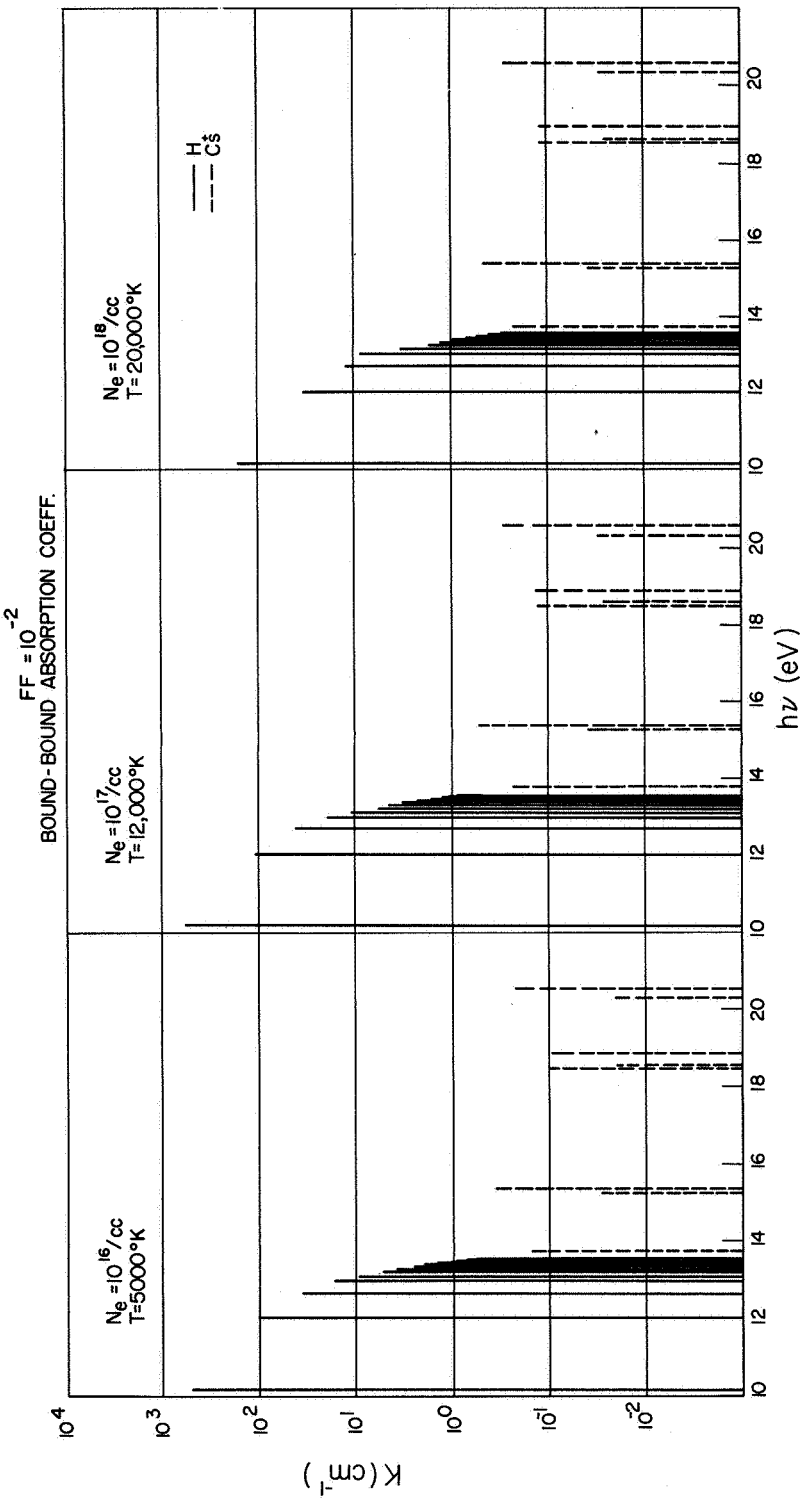

FIG. 15 Bound-bound absorption coefficient vs photon energy for a cesium-hydrogen plasma with a seed fraction of 10^{-2}, temperature and electron density parameters as shown.

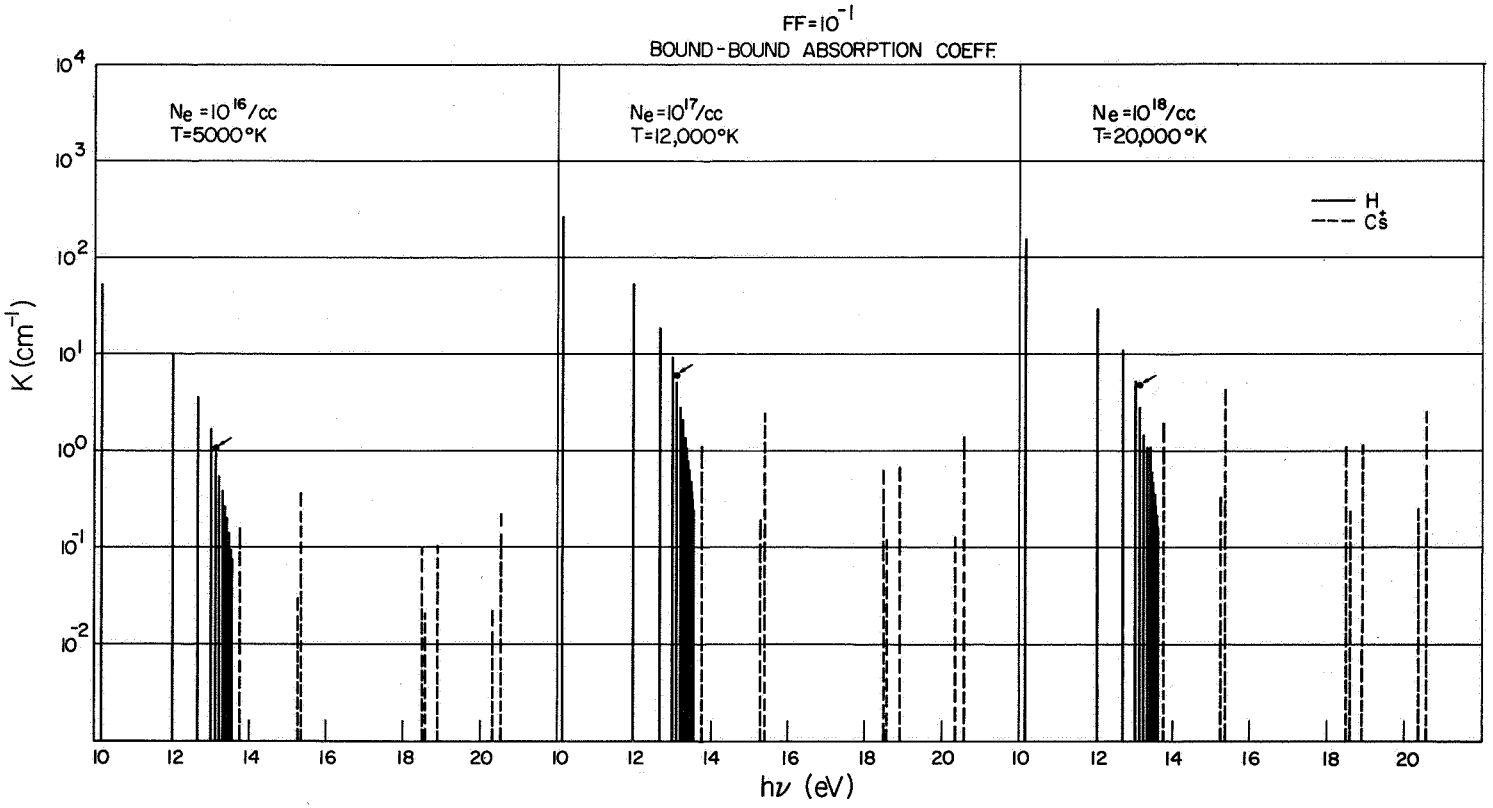

FIG. 16 Bound-bound absorption coefficient vs photon energy for a cesium-hydrogen plasma with a seed fraction of 10^{-1}, temperature and electron density parameters as shown.

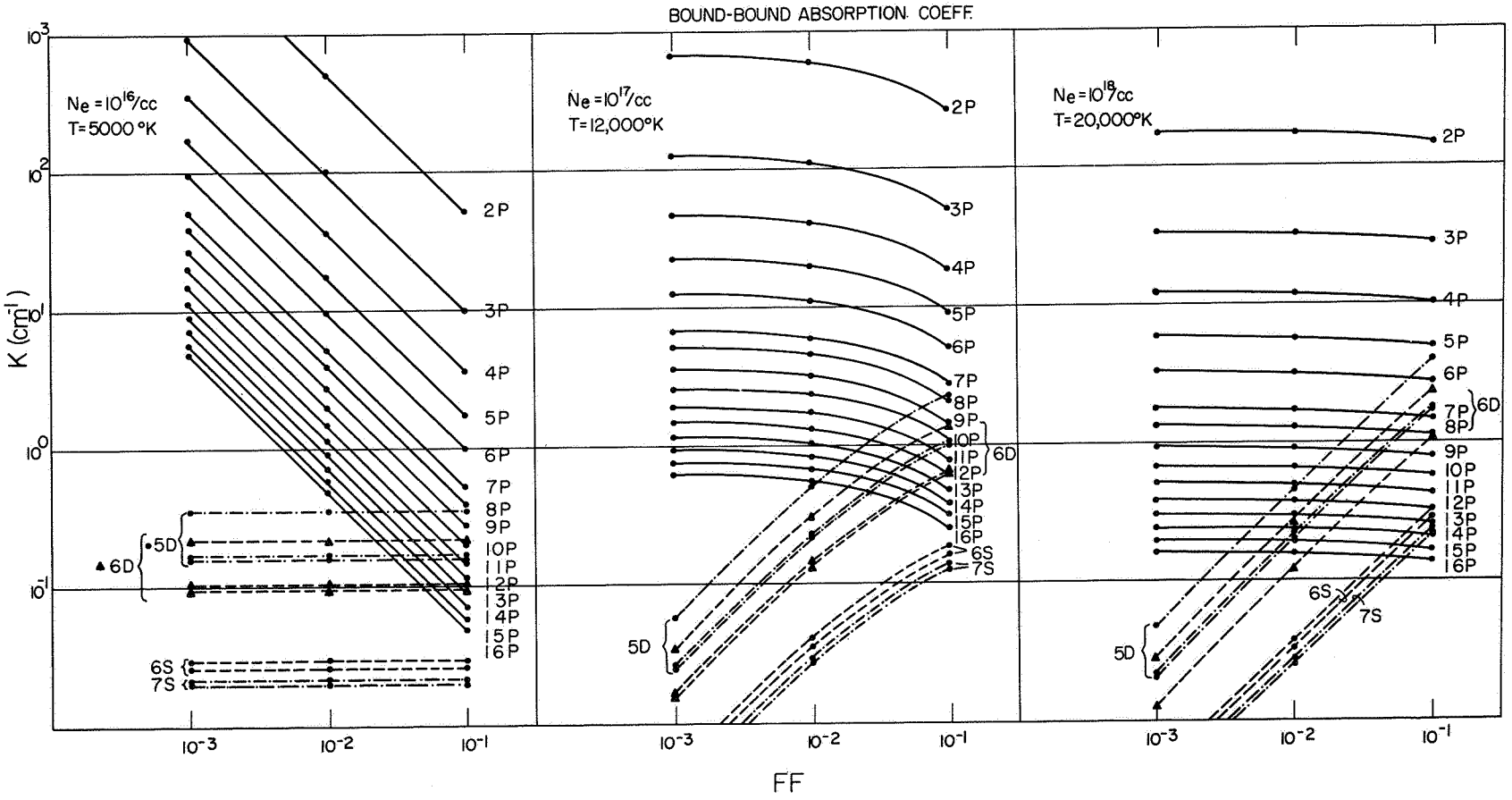

FIG. 17 Bound-bound absorption coefficient vs cesium hydrogen seed fraction, temperature and electron density parameters as shown.

From these plots, as the temperature and density increase we see the following. At low temperature and density, the hydrogen line absorption decreases as a function of seed fraction, while at high temperature and density it is independent of seed fraction. For Cs^+ the opposite is true, the line absorption being independent of seed fraction at low temperature and density, and increases with the seed fraction as the temperature and density increase, as shown by the change in curvature of the curves for $T = 12{,}000^0K$, $Ne = 10^{17}/cm^3$ and $T = 20{,}000^0K$ and $Ne = 10^{18}/cm^3$. The conclusion being that the Cs^+ line absorption efficiency increases with the three independent parameters electron density, temperature, and seed fraction, as was to be expected.

5. Total Absorption Coefficient

The total photoabsorption coefficient is obtained by adding the three contributions discussed in the previous sections. When the results are compared, the following facts emerge for the cases presented in this report.

For a temperature of 5000^0K and an electron density of $10^{16}/cm^3$, the absorption coefficient due to the free-free contribution is negligible compared to that due to the bound-free contribution. At low energies (below 13.6 eV) it is three orders of magnitude less, and at high energies (above 13.6 eV) it is at least eight orders of magnitude less. The total photoabsorption coefficient is therefore just the superposition of the line structure due to the discrete transition and the bound-free photoionization coefficient. The results are shown in Fig. 18, where they are plotted vs photon energy, with the cesium seed fraction as a parameter. By comparison with the results of Sec. 4 it is seen that the discrete line structure due to Cs^+ (above 13.6 eV) is lost in the photoionization continuum.

The results for a temperature of $12{,}000^0K$ and electron density of $10^{17}/cm^3$ are in general the same as for $T = 5000^0K$ and an

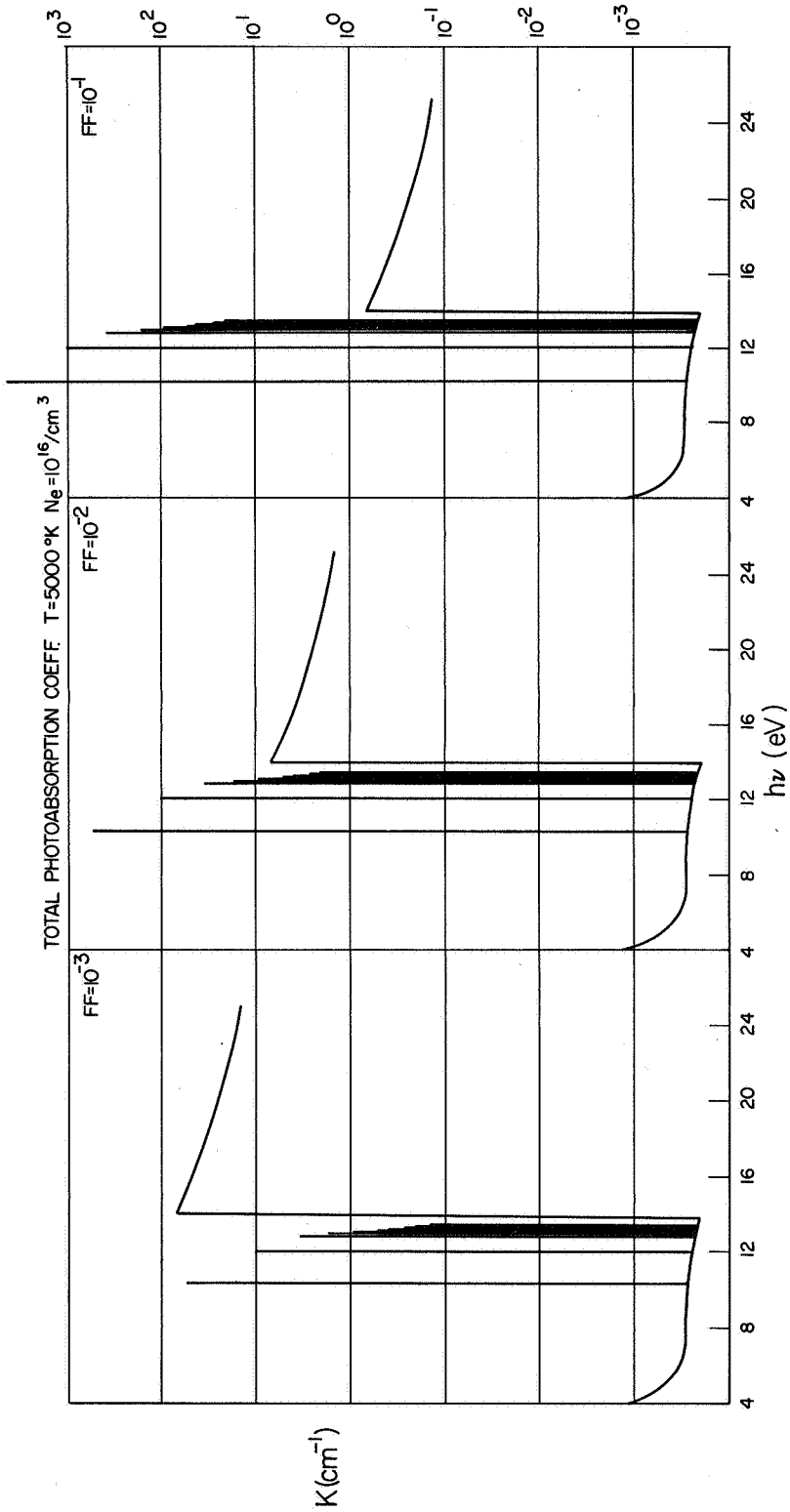

FIG. 18 Total photoabsorption coefficient as a function of photon energy at $T = 5000^{o}K$, $Ne = 10^{16}/cm^3$, with seed fraction as a parameter.

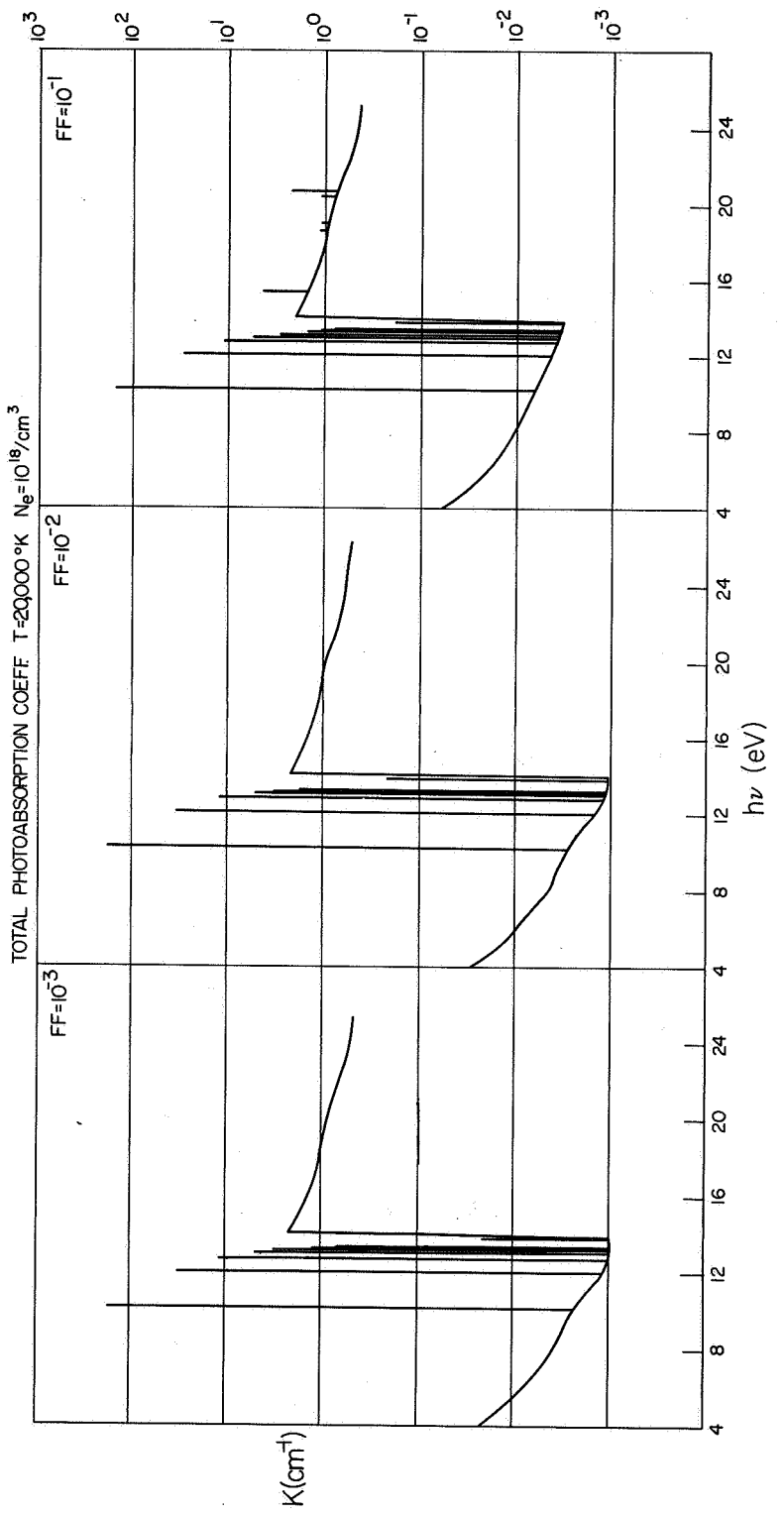

FIG. 19 Total photoabsorption coefficient as a function of photon energy at T = 12,000°K, Ne = $10^{17}/cm^3$, with seed fraction as a parameter.

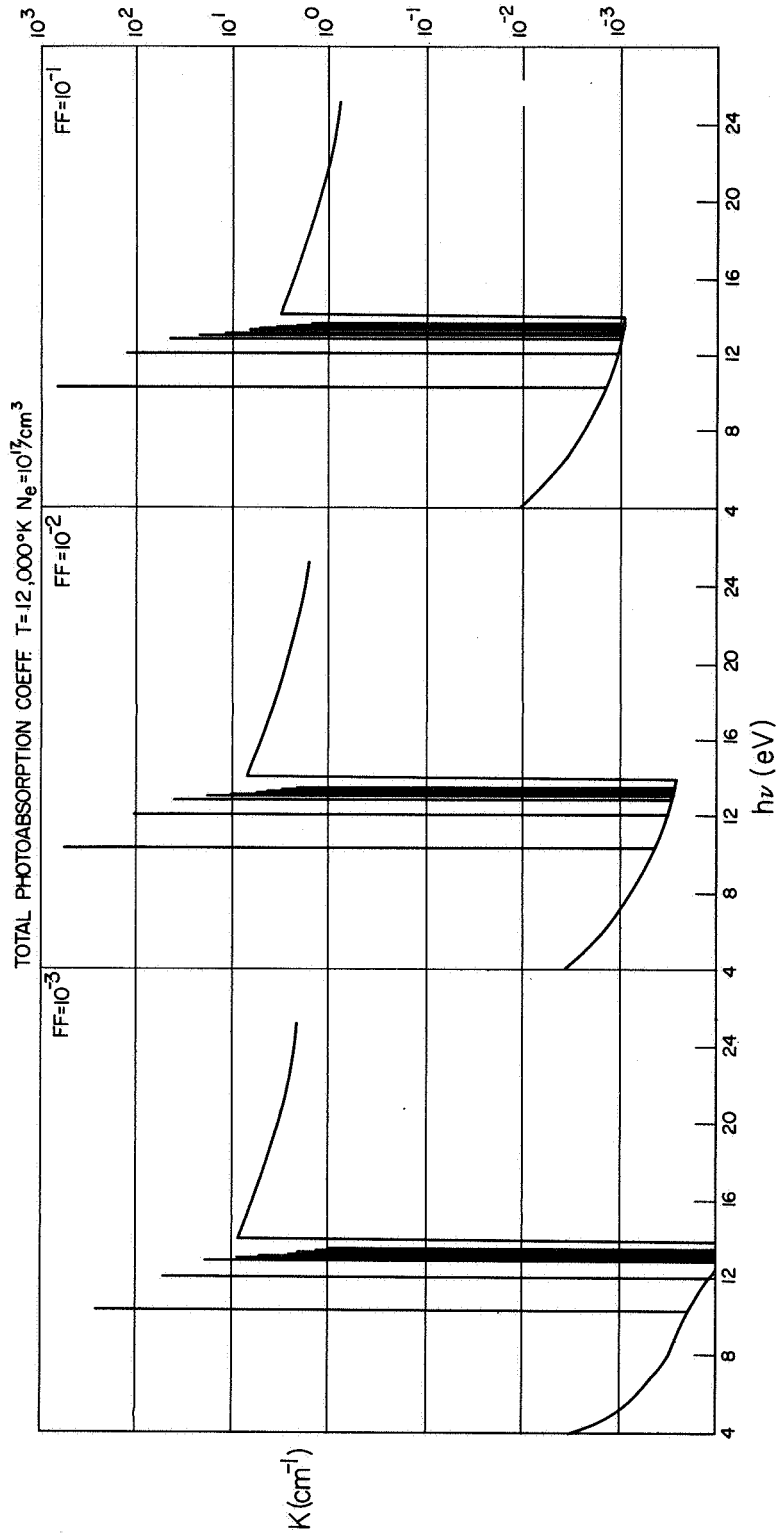

FIG. 20 Total photoabsorption coefficient as a function of photon energy at T = 20,000°K, Ne = $10^{18}/cm^3$, with seed fraction as a parameter.

electron density of $10^{16}/cm^3$, only the free-free contribution is now lower by two orders of magnitude at low energy and at least six orders of magnitude at high energy. The discrete line structure due to Cs^+ is again lost in the photoionization continuum. The results are shown in Fig. 19, plotted vs photon energy, with cesium seed fraction as a parameter.

At $20,000^0K$ the free-free contribution to the continuum is approximately 10% of the bound-free contribution for energies below 13.6 eV. At larger energies the free-free contribution is again negligible, being at least three orders of magnitude below the bound-free value. The total absorption coefficient including the lower energy modification due to the free-free contribution is shown in Fig. 20. Again the discrete line structure due to the bound-bound absorption has simply been added in. It is to be noticed that for the maximum seed fraction of $FF = 10^{-1}$ the discrete Cs^+ lines are visible above the continuum at high energy.

In summary, the cesium seed increases the absorption below 13.6 eV. The increase is most significant at the lowest energies and is nearly all due to the bound-free transitions from neutral cesium (photoionization). Above the threshold for hydrogen ionization (13 eV) the contribution of cesium is almost negligible.

III. SPECTROSCOPIC TEMPERATURE MEASUREMENT OF CS-H MIXTURE

A. INTRODUCTION

This section considers spectroscopic techniques for measuring the temperature of hot cesium seeded hydrogen gas. The primary methods are well known and involve absolute and relative line intensity measurements and continuum emission measurements. The objective in this report is to provide data so that the measurements can be performed. Particular lines are chosen and their width, absorption coefficient and emission energy density are calculated.

The range of temperature, T, pressure, p, and seed fraction, FF, are the same as in part B, Sec. II. That is, we consider

$$5000^{o}K \leq T \leq 20,000^{o}K$$

$$0.10 \text{ atm} \leq p \leq 100 \text{ atm}$$

$$10^{-3} \leq FF \leq 10^{-1}$$

Under these conditions the equilibrium electron density, N_e, is in the range

$$10^{14} \text{ cm}^{-3} \leq N_e \leq 10^{19} \text{ cm}^{-3}$$

The species concentrations are very nearly the same as they would be if the plasma were in thermodynamic equilibrium. This is a result of collisional interaction between the species. At the rather high pressures that we are considering, the radiative loss (a loss that causes departure from thermodynamic equilibrium) is small compared to collision effects which establish equilibrium. Other effects that would cause departures from equilibrium populations, such as diffusion to walls and energy input from a temperature source, are neglected as they are very much dependent on the particular device and cannot be treated in general. However, they will generally not be important in the body of the plasma, particularly when the plasma is physically large compared to collisional mean free paths.

The spectra observed from the plasma will be quite complex. There will be many lines of neutral cesium, singly ionized cesium and, at high temperatures, doubly ionized cesium. Hydrogen lines will also be present throughout the temperature range. The continua between lines is also complicated and is made up of bound-free transitions, some free-free

transitions and overlapping wings of nearby lines. The absorption coefficient of the previous section provides information about the continua that will be discussed in part E of this present section. Some molecular band spectra may also be observed. Molecular hydrogen, in particular, is present in significant quantities at the lower temperatures.

The spectra provide a wealth of information about the plasma. In particular, the temperature can be determined from the intensity of spectral lines. The electron density can be obtained from the shape of Stark broadened lines. Knowledge of electron density will also reveal the temperature in these equilibrium situations by reference to the concentration calculations (Figs. 1 - 5 of Sec. III, part A). Care must be used in interpreting properties of the plasma from emission spectra. Temperatures can be obtained from line intensities only if the lines are optically thin. Similarly, line shapes reveal electron densities only when the lines are optically thin and predominantly Stark broadened. Atomic constants for the lines must also be known to reasonable accuracy. These considerations rule out the use of much of the available spectrum.

Much of this section is devoted to consideration of the above difficulties. Lines that are suggested for spectroscopic measurements are listed in Table V. The hydrogen lines are the first four lines of the Balmer series. Pertinent atomic properties are also given. These lines are certainly not the strongest lines in the spectrum but are convenient to observe and are usually not affected by self-absorption (that is, they are optically thin). Self-absorption is reduced because none of the lines end on the ground state. Nevertheless care must be taken to be <u>certain</u> that self-absorption is not significant. This is discussed in detail in part C.

Only lines of hydrogen and neutral cesium are considered. Many lines of singly and doubly ionized cesium will be observed from the plasma, but atomic properties of these lines—particularly oscillator strengths—are not known well enough to use them for diagnostic purposes.

TABLE V

Lines Considered in This Report*

Species	Transition (L, U)	λ_o (Å)	f_{LU}	g_U	g_L	ϵ_U (Ry)	ϵ_L (Ry)
Cs I	$7S_{1/2}, 10P_{1/2}$	9812	.00017	2	2	.0244	.11736
Cs I	$7S_{1/2}, 10P_{3/2}$	9786	.00187	4	2	.0242	.11736
Cs I	$7S_{1/2}, 11P_{3/2}$	9187	.000911	4	2	.0181	.11736
Cs I	$7S_{1/2}, 12P_{3/2}$	8827	.000486	4	2	.0141	.11736
Cs I	$5D_{5/2}$, 5F	8081	.1272	14	6	.04044	.1533
Cs I	$5D_{5/2}$, 6F	7282	.0650	14	6	.02806	.1533
Cs I	$5D_{5/2}$, 7F	6872	.0383	14	6	.02059	.1533
Cs I	$5D_{5/2}$, 8F	6631	.0241	14	6	.01575	.1533
H_α	2, 3	6562	.641	18	8	.1111	.25
H_β	2, 4	4861	.1193	32	8	.0625	.25
H_γ	2, 5	4340	.0434	50	8	.0400	.25
H_δ	2, 6	4101	.0221	72	8	.0278	.25

* f is the oscillator strength,
λ_o is the wavelength at line center in angstroms,
g_U is the statistical weight of the upper level and
ϵ_U is the binding energy of the upper level in rydbergs (1 rydberg = 13.6 eV).
The subscript L refers to the lower level.

Moreover, ion lines are not really needed, as temperatures can be reasonably well deduced from neutral lines. It should be realized that the oscillator strengths calculated in part B of Sec. III for Cs^+ are not accurate enough for temperature diagnostics but are satisfactory for estimates of the absorption coefficient. This is because the ion line absorption is a small part of the total absorption.

The remainder of this section is a detailed calculation of the intensities and shapes of the lines listed in Table V. The assumption, already mentioned, that the species and their excited states are in equilibrium and prior knowledge of the atomic properties of the lines allows us to calculate intensities. The results of this calculation and a discussion of their interpretation in terms of a temperature are presented in part D. The line widths and absorption coefficients are determined in parts B and C. The line width is needed to determine electron density which is a critical parameter in the discussions, and to calculate the absorption coefficient at line center. The absorption coefficient must be known to be certain that self-absorption is not present. Finally, continuum emission is discussed briefly in part E.

It is assumed throughout the discussion that the total pressure of the gas mixture and the cesium seed fraction are known.

B. LINE WIDTH

Atomic line widths must be known to calculate the absorption coefficient at line center. The absorption coefficients are calculated in part C.

Atomic lines are broadened beyond their natural width in several ways. The important mechanisms to consider here are Doppler broadening, resonance broadening, Van der Waals broadening and Stark broadening. The lines that we consider are all greatly Stark broadened and the other mechanisms are not significant. Nevertheless, expressions are given from the standard literature for all these cases so that other

lines and conditions can be easily considered. In all expressions below, $\Delta\lambda$ is the half half-width in Å .

1. Doppler Broadening

The half-width at half maximum intensity is given by

$$\Delta\nu = \nu_o \left(2 \ell n \, 2 \frac{kT}{Mc^2}\right)^{1/2} \tag{19}$$

It is more convenient to convert to Angstrom units,

$$\Delta\lambda = 3.585 \times 10^{-7} \lambda_o \sqrt{T/M} \tag{20}$$

where λ_o is the line center wavelength in Å, $\Delta\lambda$ is the half half-width in Å, T is the temperature in ^oK, and M is the atomic weight of the species.

At 20,000^{o}K an 8000 Å cesium line has a $\Delta\lambda$ of 0.035 Å and an 8000 Å hydrogen line has $\Delta\lambda = 0.40$ Å . The width is less at lower temperature.

2. Resonance Broadening

This is due to the radiating atom colliding with a neutral atom of its own kind (Cs - Cs or H - H) when either the upper or lower level of the radiator possesses dipole matrix elements connecting it to the initial state (usually the ground state) of the perturber. The expression for the half half-width in frequency units is given by impact theory as

$$\Delta\nu = \frac{3}{2}\left(\frac{g_L}{g_U}\right)^{1/2}\left(\frac{e^2 f'}{2\pi m\nu'}\right) N_p \qquad (21)$$

$e = 4.8 \times 10^{-10}$ esu

$m = 9.1 \times 10^{-28}$ gms

g_U, g_L = statistical weight of the upper and lower levels of the transition, respectively.

f' = oscillator strength between the perturber and either upper or lower level of the radiating atom.

ν' = frequency of the transition associated with f', sec^{-1}.

N_p = perturber density, in cm^{-3}.

The impact theory is only valid when the perturber density is not too large. The requirement is

$$N_p \ll \frac{1}{2\pi}\left(\frac{2}{3}\right)^{3/2}\left(\frac{g_U}{g_L}\right)^{3/4}\left(\frac{2\pi m\nu'}{e^2 f'}\bar{V}\right)^{3/2} \qquad (22)$$

The only new quantity in this expression is the average perturber velocity, $\bar{V}$, given in cm/sec.

The average velocity can be expressed in terms of the temperature and the expression rewritten as

$$\frac{\Delta\lambda}{\lambda} = 0.524 \times 10^{-20} \left(\frac{g_L}{g_U}\right)^{1/2} (N_p f') \left(\frac{\lambda_o}{6200}\right) \left(\frac{10.0}{h\nu'}\right)$$

$$N_p \ll 6.90 \times 10^{19} \left(\frac{g_L}{g_U}\right)^{3/4} \left(\frac{T}{5000}\right)^{1/2} \left(\frac{6200}{\lambda_o}\right)^{3/2} \left(\frac{h\nu'}{10.0}\right)$$

with

λ_o in Å, T in ^oK, $h\nu'$ in eV and N_p in cm^{-3}.

3. Van der Waals Broadening

Van der Waals broadening results from collision of the radiating atom with other atoms when neither level of the radiative transition is connected by dipole matrix elements to the state of the perturber atom. The important perturbers are nearly always ground state atoms and may be of the same or a different species. This effect has most often been observed with large pressures of a foreign gas mixed in with the radiating gas.

The impact theory is almost always valid for this broadening and gives the half half-width as

$$\Delta\nu = \frac{1}{2} N_p \left(\frac{g\pi\hbar^5 \overline{R_U^2}}{16m^3 E_p^2}\right)^{2/5} \overline{v^{3/5}} \qquad (23)$$

with

$$\overline{R_U^2} = \frac{1}{2}\left(\frac{E_H}{E_\infty - E_H}\right)\left[\frac{5z^2E_H}{E_\infty - E_H} + 1 - 3\,\ell_U(\ell_U + 1)\right] \tag{24}$$

where

E_∞ = Ionization potential of radiating atom,

E_H = Ionization potential of hydrogen,

E_U = Excitation potential of upper state of radiating atom,

E_p = Excitation potential of first resonance level of perturber, in ergs,

ℓ_U = Orbital quantum number of upper state of radiating atom,

N_p = Perturber density, cm^{-3}, and

z = Effective charge on radiating electron (≈ 1.0).

$\overline{R_U^2}$ is the matrix element of the square of the position vector of the radiating electron in the initial state. The bar over $V^{3/5}$ means the average of $V^{3/5}$ over the velocity distribution.

The expression with wavelength in Å, E_p in eV, and T in ^oK is

$$\frac{\Delta\lambda}{\lambda_o} = 1.17 \times 10^{-24}\, N_p\left(\frac{\overline{R_U^2}}{E_p^2}\right)^{2/5}\left(\frac{\lambda_o}{6200}\right)\left(\frac{T}{10^4 M}\right)^{3/10} \tag{25}$$

As before, M is the molecular weight.

4. Stark Broadening

Stark broadening results from collisions of the radiating atom with ions and electrons. The interaction is through the electric fields of the charged perturbers and is of longer range than in the neutral atom collisions involved in resonance and Van der Waals broadening. This broadening dominates, therefore, at high electron (ion) density. In practice, whenever the ion density is 1% or more of the atom density the Stark effect must be considered. Ions and electrons must both be included in the calculation of Stark broadened widths. The calculation procedures are also different if the lines are, or are not, isolated. Isolated lines occur when the states involved in the radiative transition are sufficiently far away in energy from neighboring states. Transitions in hydrogen are never isolated because of the ℓ degeneracy of the excited states. Cesium lines are usually isolated but will become nonisolated (hydrogenic) at high ion densities when broadening of the upper level is sufficiently large to cause overlapping with neighboring levels. Very high states of any atom give non-isolated lines because high levels are necessarily close together. However, such high levels are not usually observed in diagnostic studies.

Simple expressions for the half half-widths of isolated lines have been given by Griem (Ref. 9)

$$\Delta\lambda = [1 + 1.75\ \alpha(1 - 0.75)r]\omega \qquad (26)$$

if

$$r < 0.8$$

$$\alpha < 0.5$$

with

$$r = \frac{15^{1/3}}{2^{1/6}} \frac{eN_p^{1/6}}{(kT)^{1/2}} \quad . \tag{27}$$

The coefficient r is the ratio of the mean distance between ions to the Debye distance. The coefficient α accounts for the contribution of ions to the total width using quasistatic theory, while ω is the impact theory width from electrons. The α and ω values are tabulated in Griem's book (Ref. 9). Only the upper state of isolated lines needs to be considered. Hence, lines from the same upper state have the same width in units of frequency or energy. The width ω is given by Griem in angstroms and must be converted for other lines with the same upper state by multiplying by $(\lambda_{line}/\lambda_{table})^2$.

Hydrogen lines are not isolated and their width cannot be expressed as in Eq. (26). Detailed calculations are available for these lines (Ref. 16). Table VI shows the widths of the lines of Table V given by Eq. (26) and Ref. 16 at the densities and temperatures of interest to us. Under all conditions listed in Table VI the lines are predominantly Stark broadened and other broadening mechanisms can be ignored. This is not necessarily true at lower electron densities than listed. At higher electron densities the cesium lines are no longer isolated ($\alpha \geq 0.5$ and/or $r \geq 0.8$). It should be emphasized that the entries in Table VI are half widths at half maximum intensity. The hydrogen lines usually have two symmetric maximum points off line center as the Stark fields remove the ℓ degeneracy of the states. Nevertheless, the hydrogen widths in Table VI are still widths at half the maximum intensity.

TABLE VI-A

Half-width at Half Maximum Intensity in Angstroms, Cesium Lines

Transition (L, U)	N_e (cm^{-3})	Temp (^oK)					
		5000	6000	7000	8000	9000	10,000
$7S, 10P_{1/2}$	10^{15}	2.960	3.048	3.120	3.176	3.200	3.240
$7S, 10P_{3/2}$	10^{15}	3.437	3.484	3.539	3.587	3.626	3.674
$7S, 11P_{3/2}$	10^{15}	6.263	6.366	6.453	6.526	6.577	6.614
$7S, 12P_{3/2}$	10^{15}	10.902	11.109	11.247	11.316	11.454	11.523
$5D_{5/2}, 5F$	10^{15}	0.640	0.636	0.635	0.633	0.629	0.629
$5D_{5/2}, 6F$	10^{15}	1.91	1.90	1.89	1.88	1.87	1.85
$5D_{5/2}, 7F$	10^{15}	3.80	3.77	3.77	3.75	3.77	3.78
$5D_{5/2}, 8F$	10^{15}	7.33	7.29	7.27	7.25	7.26	7.25
$7S, 10P_{3/2}$	10^{16}	31.44	32.24	33.60	34.40	34.72	35.28
$7S, 10P_{3/2}$	10^{16}	36.66	37.53	38.32	39.03	39.58	40.21
$7S, 11P_{3/2}$	10^{16}	67.82	69.64	71.10	72.42	73.29	74.02
$7S, 12P_{3/2}$	10^{16}	120.13	123.44	126.34	127.93	130.34	131.51
$5D_{5/2}, 5F$	10^{16}	6.81	6.83	6.86	6.89	6.87	6.90
$5D_{5/2}, 6F$	10^{16}	21.06	21.18	21.33	21.39	21.39	21.27
$5D_{5/2}, 7F$	10^{16}	*	*	*	*	*	*
$5D_{5/2}, 8F$	10^{16}	*	*	*	*	*	*

* Lines are becoming nonisolated.

TABLE VI - B

Half Width at Half Maximum Intensity in Angstroms, Hydrogen Lines

Line	Temperature**	$N_e = 10^{15}$	10^{16}	10^{17}	10^{18}
H_α	10,000		0.70	4.35	22.6
H_α	20,000		0.70	4.35	25.1
H_β	10,000	0.98	4.79	22.4	
H_β	20,000	1.01	4.67	21.2	
H_γ	10,000	0.88	4.79	24.0	
H_γ	20,000	0.72	4.67	29.4	
H_δ	10,000	2.07	10.50		
H_δ	20,000	2.07	10.80		

** Interpolate linearly for intermediate temperature.

C. OPTICAL THICKNESS

Line intensities cannot be used to determine the temperature in the gas unless they are optically thin. The optical depth of a uniform gas is

$$\text{optical depth} = k(\nu)\, x$$

where $k(\nu)$ is the frequency dependent absorption coefficient in cm^{-1} and x is the gas thickness in cm. When the optical depth at frequency ν is much less than one, the gas is optically thin at that frequency.

The absorption coefficient in the vicinity of a line centered at frequency ν_0 and resulting from an atomic transition from upper level 2 to lower level 1 is

$$k(\nu) = \frac{h\nu_0}{4\pi}\left[B_{12}N_1 - B_{21}N_2\right]S(\nu) \tag{28}$$

where $S(\nu)$ is the line shape, B_{12} is the Einstein absorption coefficient associated with intensity (cm^2/erg-sec), B_{21} is the induced emission coefficient and the N's are the level densities, cm^{-3}.

If the line has a pure Lorentz profile of half half-width $\Delta\nu = \gamma/4\pi$

$$S(\nu) = \frac{\gamma/4\pi^2}{(\nu - \nu_0)^2 + (\gamma/4\pi)^2} \tag{29}$$

the absorption coefficient at line center is

$$k_o = \frac{h\nu_o}{\pi\gamma}\left[B_{12}N_1 - B_{21}N_2\right] \tag{30}$$

We neglect the B_{21} term so that we have the coefficient for absorption only and do not consider the compensating effect of induced emission. The expression in terms of the oscillator strength is then

$$k_o = \frac{0.10616}{\gamma} N_1 f_{12} \tag{31}$$

and converting γ to angstrom units by

$$\gamma = 4\pi(\Delta\nu)$$

$$\Delta\nu = \frac{c}{\lambda_o^2}\Delta\lambda$$

gives

$$k_o = 2.81 \times 10^{-21}\left(\frac{\lambda_o^2}{\Delta\lambda}\right) N_1 f_{12} \tag{32}$$

with λ_o, $\Delta\lambda$ in angstroms. $\Delta\lambda$ is the half width at half maximum intensity.

The calculated absorption coefficients are shown in Table VII. The line widths of Table VI have been used in Eq. (32). It should be emphasized that Eq. (32) is strictly correct only for pure Lorentz profiles (Eq. (29)), while Stark broadening by ions and electrons gives a mixture of Lorentz shapes. It is felt, however, that use of Eq. (32) with the half widths of Table VI gives k_o accurately enough to use as a warning as to when the lines become optically thick. Accuracies of k_o to factors of two are sufficient for this purpose.

The product of k_o of Table VII and the actual gas thickness x is the optical thickness. Lines will be sufficiently thin to use for spectroscopic temperature measurements if $k_o x < 0.25$.

D. LINE EMISSION AND TEMPERATURE MEASUREMENTS

High temperature gas will emit photons by spontaneous emission. Induced emission is not important when the gas is optically thin for absorption. The energy emitted per unit volume per unit solid angle in an atomic line centered at frequency ν_o is

$$U(\Omega) = \frac{1}{4\pi} N_2 A_{21} \, h\nu_o \text{ erg/cm}^3\text{-sec-sr} \tag{33}$$

where N_2 is the population density of atoms in the upper state of the transition and A_{21} is the Einstein transition probability.

The same expression in terms of the oscillator strength is

$$U(\Omega) = 1.054 \left(\frac{g_1}{g_2}\right) \frac{N_2}{\lambda_o^3} f_{12} \text{ W/cm}^3\text{-sr} \tag{34}$$

TABLE VII - A

Absorption Coefficient at Line Center of Cesium Lines

FF = 10^{-3}

Transition	N_e	Temp. (^{0}K)** 5000	6000	7000	8000	9000	10,000
$7S_{\frac{1}{2}}$ $10P_{1/2}$	10^{15}	1.87(-6)	2.375(-6)	2.74(-6)	8.51(-7)		
$7S_{\frac{1}{2}}$ $10P_{3/2}$	10^{15}	1.77(-5)	2.28(-5)	2.65(-5)	8.25(-6)		
$7S_{\frac{1}{2}}$ $11P_{5/2}$	10^{15}	4.16(-6)	5.34(-6)	6.22(-6)	1.95(-6)		
$7S_{\frac{1}{2}}$ $12P_{3/2}$	10^{15}	1.18(-6)	1.51(-6)	1.75(-6)	5.54(-7)		
$5D_{5/2}$, 5F	10^{15}	4.37(-2)	4.46(-2)	4.60(-2)	1.32(-2)		
$5D_{5/2}$, 6F	10^{15}	6.08(-3)	6.19(-3)	6.42(-3)	1.85(-3)		
$5D_{5/2}$, 7F	10^{15}	1.60(-3)	1.64(-3)	1.69(-3)	4.86(-4)		
$5D_{5/2}$, 8F	10^{15}	4.87(-4)	4.96(-4)	5.13(-4)	1.47(-4)		
$7S_{\frac{1}{2}}$ $10P_{1/2}$	10^{16}	9.66(-6)	7.35(-6)	7.94(-6)	6.76(-6)	1.84(-6)	3.94(-7)
$7S_{\frac{1}{2}}$ $10P_{3/2}$	10^{16}	9.08(-5)	6.91(-5)	7.62(-5)	6.53(-05)	1.76(-5)	3.81(-6)
$7S_{\frac{1}{2}}$ $11P_{3/2}$	10^{16}	2.11(-5)	1.60(-5)	1.77(-5)	1.51(-5)	4.08(-6)	8.89(-7)
$7S_{\frac{1}{2}}$ $12P_{3/2}$	10^{16}	5.86(-6)	4.45(-6)	4.88(-6)	4.22(-6)	1.13(-6)	2.46(-6)
$5D_{5/2}$, 5F	10^{16}	2.25(-1)	1.36(-1)	1.33(-1)	1.05(-1)	2.65(-2)	5.49(-3)
$5D_{5/2}$, 6F	10^{16}	3.02(-2)	1.82(-2)	1.78(-2)	1.40(-2)	3.53(-3)	7.39(-4)
$5D_{5/2}$, 7F	10^{16}	*	*	*	*	*	*
$5D_{5/2}$, 8F	10^{16}	*	*	*	*	*	*

*Lines are becoming nonisolated.

**The parenthesis encloses the power of ten by which the entry should be multiplied.

TABLE VII - A (cont.)

FF = 10^{-2}

Transition (L, U)	N_e (cm^{-3})	Temp (^oK) 5000	6000	7000	8000	9000	10,000
$7S, 10P_{1/2}$	10^{15}	1.87(-6)	2.39(-6)	3.30(-6)	3.58(-6)		
$7S, 10P_{3/2}$	10^{15}	1.77(-5)	2.29(-5)	3.18(-5)	3.47(-5)		
$7S, 11P_{3/2}$	10^{15}	4.16(-6)	5.38(-6)	7.49(-6)	8.18(-6)		
$7S, 12P_{3/2}$	10^{15}	1.18(-6)	1.52(-6)	2.12(-6)	2.33(-6)		
$5D_{5/2}, 5F$	10^{15}	4.37(-2)	4.49(-2)	5.55(-2)	5.55(-2)		
$5D_{5/2}, 6F$	10^{15}	6.08(-3)	6.23(-3)	7.74(-3)	7.78(-3)		
$5D_{5/2}, 7F$	10^{15}	1.60(-3)	1.65(-3)	2.04(-4)	2.04(-4)		
$5D_{5/2}, 8F$	10^{15}	4.87(-4)	4.99(-4)	6.18(-4)	6.18(-4)		
$7S, 10P_{1/2}$	10^{16}	9.66(-6)	7.35(-2)	8.13(-4)	9.71(-6)	7.54(-6)	2.93(-6)
$7S, 10P_{3/2}$	10^{16}	9.07(-5)	6.91(-5)	7.80(-5)	9.04(-5)	7.23(-5)	2.80(-5)
$7S, 11P_{3/2}$	10^{16}	2.11(-5)	1.60(-5)	1.81(-5)	2.16(-5)	1.67(-5)	6.53(-6)
$7S, 12P_{3/2}$	10^{16}	5.86(-6)	4.45(-6)	5.00(-6)	6.06(-6)	4.64(-6)	1.81(-6)
$5D_{5/2}, 5F$	10^{16}	2.25(-1)	1.36(-1)	1.36(-1)	1.51(-1)	1.09(-1)	4.04(-2)
$5D_{5/2}, 6F$	10^{16}	3.02(-2)	1.82(-2)	1.82(-2)	2.01(-2)	1.45(-2)	5.43(-3)
$5D_{5/2}, 7F$	10^{16}	*	*	*	*	*	*
$5D_{5/2}, 8F$	10^{16}	*	*	*	*	*	*

* Lines are becoming nonisolated.

TABLE VII - A (cont.)

$FF = 10^{-1}$

Transition (L,U)	N_e (cm^{-3})	Temp (^oK) 5000	6000	7000	8000	9000	10,000
$7S, 10P_{1/2}$	10^{16}	9.66(-6)	7.35(-6)	8.15(-6)	1.01(-5)	1.10(-5)	1.05(-5)
$7S, 10P_{3/2}$	10^{16}	9.69(-5)	7.38(-5)	8.35(-5)	1.01(-4)	1.12(-4)	1.08(-4)
$7S, 11P_{3/2}$	10^{16}	2.11(-5)	1.60(-5)	1.81(-5)	2.26(-5)	2.42(-5)	2.35(-5)
$7S, 12P_{3/2}$	10^{16}	5.86(-6)	4.45(-6)	5.01(-6)	6.32(-6)	6.74(-6)	6.52(-6)
$5D_{5/2}, 5F$	10^{16}	2.25(-1)	1.36(-1)	1.37(-1)	1.58(-1)	1.59(-1)	1.45(-1)
$5D_{5/2}, 6F$	10^{16}	3.02(-2)	1.82(-2)	1.83(-2)	2.10(-2)	2.11(-2)	1.95(-2)
$5D_{5/2}, 7F$	10^{16}	*	*	*	*	*	*
$5D_{5/2}, 8F$	10^{16}	*	*	*	*	*	*

* Lines are becoming nonisolated.

TABLE VII-B

Absorption Coefficient at Line Center of Hydrogen Lines

Transition	N_e	FF	Temp (^{0}K)*			
	—	—	10,000	12,000	16,000	20,000
H_α	10^{16}	10^{-3}	8.91(-1)			
H_α	10^{16}	10^{-2}	7.10(-1)			
H_α	10^{16}	10^{-1}	2.35(-1)	2.92(-1)		
H_β	10^{16}	10^{-3}	1.33(-2)			
H_β	10^{16}	10^{-2}	2.43(-3)			
H_β	10^{16}	10^{-1}	3.51(-3)	4.37(-3)		
H_γ	10^{16}	10^{-3}	3.85(-3)			
H_γ	10^{16}	10^{-2}	3.07(-3)			
H_γ	10^{16}	10^{-1}	1.02(-3)	1.27(-3)		
H_δ	10^{16}	10^{-3}	8.00(-4)			
H_δ	10^{16}	10^{-2}	6.37(-4)			
H_δ	10^{16}	10^{-1}	2.11(-4)	2.59(-4)		
H_α	10^{17}	10^{-3}	1.10(+1)	5.44(0)	1.72(0)	1.03(0)
H_α	10^{17}	10^{-2}	3.89(0)	4.80(0)	1.70(0)	1.01(0)
H_α	10^{17}	10^{-1}	5.20(-1)	2.19(0)	1.51(0)	9.07(-1)
H_β	10^{17}	10^{-3}	2.17(-1)	1.09(-1)	3.54(-2)	2.15(-2)
H_β	10^{17}	10^{-2}	7.71(-2)	9.61(-2)	3.49(-2)	2.13(-2)
H_β	10^{17}	10^{-1}	1.04(-2)	4.37(-2)	3.11(-2)	1.90(-2)
H_γ	10^{17}	10^{-3}	5.88(-2)	2.79(-2)	8.14(-3)	4.54(-3)
H_γ	10^{17}	10^{-2}	2.09(-2)	2.46(-2)	8.04(-3)	4.48(-3)
H_γ	10^{17}	10^{-1}	2.81(-3)	1.12(-2)	7.16(-3)	4.00(-3)
H_δ	10^{18}	10^{-3}	-	7.78(+1)	2.65(+1)	1.27(+1)
H_δ	10^{18}	10^{-2}	1.05(+1)	4.03(+1)	2.55(+1)	1.25(+1)
H_δ	10^{18}	10^{-1}	1.10(0)	6.91(0)	1.88(+1)	1.11(+1)

* The bracket encloses the power of ten by which the entry should be multiplied.

where λ_o is in Å, N_2 in cm^{-3}. The g's are statistical weights as before. The population densities N_2 in Eq. (34) and N_1 in Eq. (32) are given from statistical mechanics as

$$N_i = \frac{g_i}{g_G} N_G \, e^{-E_i/kT} \tag{35}$$

where N_G is the number of atoms in the ground state and E_i is the excitation energy of the state i. The ground state atom densities can be deduced from concentration calculations presented in Figs. 1 - 4 of this report. More results of this kind are shown in Appendix B.

Intensities of the hydrogen lines as given by Eq. (34) are presented in Table VIII. Figures 21 and 22 are plots of the cesium intensities vs temperature. Some hydrogen intensities are plotted in Figs. 23 and 24. At higher temperatures than plotted, the cesium lines merge into other lines and can no longer be used. Hydrogen lines at lower than $10{,}000^{\circ}K$ are becoming optically thick. Gas temperature throughout the range from $5000^{\circ}K$ to $20{,}000^{\circ}K$ can be determined from the line intensities plotted in Figs. 21 - 24. The procedure is as follows:

1. Determine electron density N_e measuring half widths at half maximum intensity of the lines of Table V and comparing with the widths of Table VI.

2. The concentration curves of Figs. 1 - 4 of this report and of Figs. 3, 5, 7 and 9 in Appendix B can be used to determine a first estimate of temperature from knowledge of the electron density, total pressure and seed fraction. This is not very sensitive above $15{,}000^{\circ}K$.

3. Below about $10{,}000^{\circ}K$ the absolute intensity of cesium lines can be compared with Figs. 21 and 22 to determine temperature. Care must be taken to ensure that the lines used are optically thin. The value of $k_o x$ must be less than about 0.25. The preliminary estimate of temperature from step 2 can be used to determine k_o from Table VII.

4. Above $10{,}000^{\circ}K$ the absolute intensity of hydrogen lines can be compared with Figs. 23 and 24 to determine temperature. Care must be taken to insure that the lines are optically thin.

The procedure described above is recommended as the best spectroscopic technique for temperature measurement. The hydrogen lines included are very strong, and the cesium lines are strong enough to be observed in most experimental situations.

Relative line intensity ratios can also be used to determine temperature. The technique was described in the last annual report (Appendix A) and is generally well known (Ref. 16). Care must again be taken to use only lines that are optically thin. This technique requires plotting intensity ratios (suitably modified) against the binding energies of the upper states involved in the atomic transition. It is less sensitive when applied to the lines of Table V than using absolute line intensities and is for this reason not recommended as strongly. However, it is simpler experimentally and is a procedure that is often used.

Finally, emission in the continua may also be used to determine temperature as discussed in the next paragraph.

E. CONTINUUM EMISSION

The absorption coefficient of Sec. III, part B of this report can be used in Kirchoff's law to determine the emission of the

TABLE VIII

Hydrogen Balmer Series Line Intensities

N_e (cm^{-3})	Transition	Temp (^oK)	FF * 10^{-3}	10^{-2}	10^{-1}
10^{16}	H_α	10,000	2.14(1)	1.71(0)	5.67(-1)
	H_β	10,000	4.56(0)	3.63(-1)	1.20(-2)
	H_γ	10,000	1.63(0)	1.30(-1)	4.32(-2)
	H_δ	10,000	8.08(-1)	6.38(-2)	2.15(-2)
10^{17}	H_α	10,000	1.64(2)	5.81(1)	7.82(0)
	H_α	12,000	1.17(2)	1.04(2)	4.74(1)
	H_α	16,000	5.84(1)	5.75(2)	5.14(1)
	H_α	20,000	4.61(1)	4.57(1)	4.07(1)
	H_β	10,000	2.84(1)	2.50(1)	1.63(2)
	H_β	12,000	2.84(1)	1.63(1)	1.45(1)
	H_β	16,000	1.65(1)	1.42(1)	1.28(1)
	H_β	20,000	1.43(1)	1.42(1)	5.96(-1)
	H_γ	10,000	1.25(1)	4.44(0)	4.34(0)
	H_γ	12,000	1.01(1)	9.51(0)	4.34(0)
	H_γ	16,000	6.76(0)	6.68(0)	5.96(0)
	H_γ	20,000	6.19(0)	6.11(0)	5.46(0)
	H_δ	10,000	6.19(0)	2.21(0)	2.97(0)
	H_δ	12,000	5.54(0)	4.89(0)	2.23(0)

* The bracket encloses the power of ten by which the entry should be multiplied.

TABLE VIII (cont.)

Hydrogen Balmer Series Line Intensities

N_e (cm^{-3})	Transition	Temp (^oK)	10^{-3}	FF* 10^{-2}	10^{-1}
10^{17}	H_δ	16,000	3.62(0)	3.57(0)	3.19(0)
	H_δ	20,000	3.38(0)	3.57(0)	2.98(0)
10^{18}	H_α	10,000		8.15(2)	8.53(1)
	H_α	12,000	8.94(3)	4.63(3)	7.93(2)
	H_α	16,000	5.00(3)	4.31(3)	3.53(3)
	H_α	20,000	3.29(3)	3.25(3)	2.87(3)
	H_β	10,000		1.74(2)	1.82(1)
	H_β	12,000	2.16(3)	1.12(3)	1.92(2)
	H_β	16,000	1.41(3)	1.36(3)	9.99(2)
	H_β	20,000	1.03(3)	1.01(3)	9.01(2)
	H_γ	10,000		6.21(1)	6.51(0)
	H_γ	12,000	8.22(2)	4.25(2)	7.27(1)
	H_γ	16,000	5.77(2)	5.56(2)	4.09(2)
	H_γ	20,000	4.41(2)	4.34(2)	3.86(2)
	H_δ	10,000		3.08(1)	3.23(0)
	H_δ	12,000	4.21(2)	2.18(2)	3.74(1)
	H_δ	16,000	3.09(2)	2.97(2)	2.19(2)
	H_δ	20,000	2.40(2)	2.38(2)	2.11(2)

* The bracket encloses the power of ten by which the entry should be multiplied.

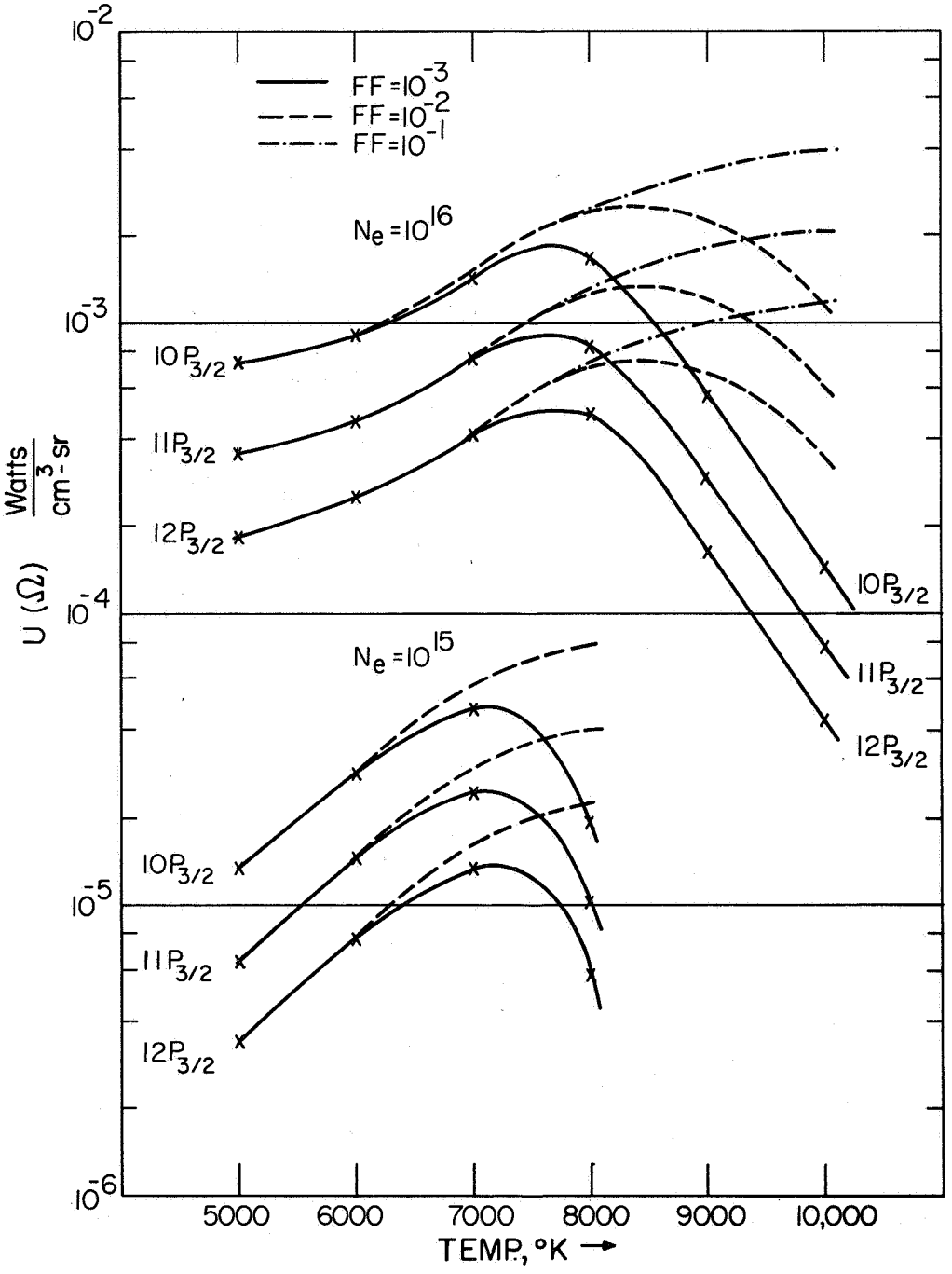

FIG. 21 $7S_{1/2}$, n $P_{3/2}$ cesium line intensities at $Ne = 10^{15}/cm^3$ and $10^{16}/cm^3$. The decreasing intensity at high temperature is due to decreasing cesium concentration.

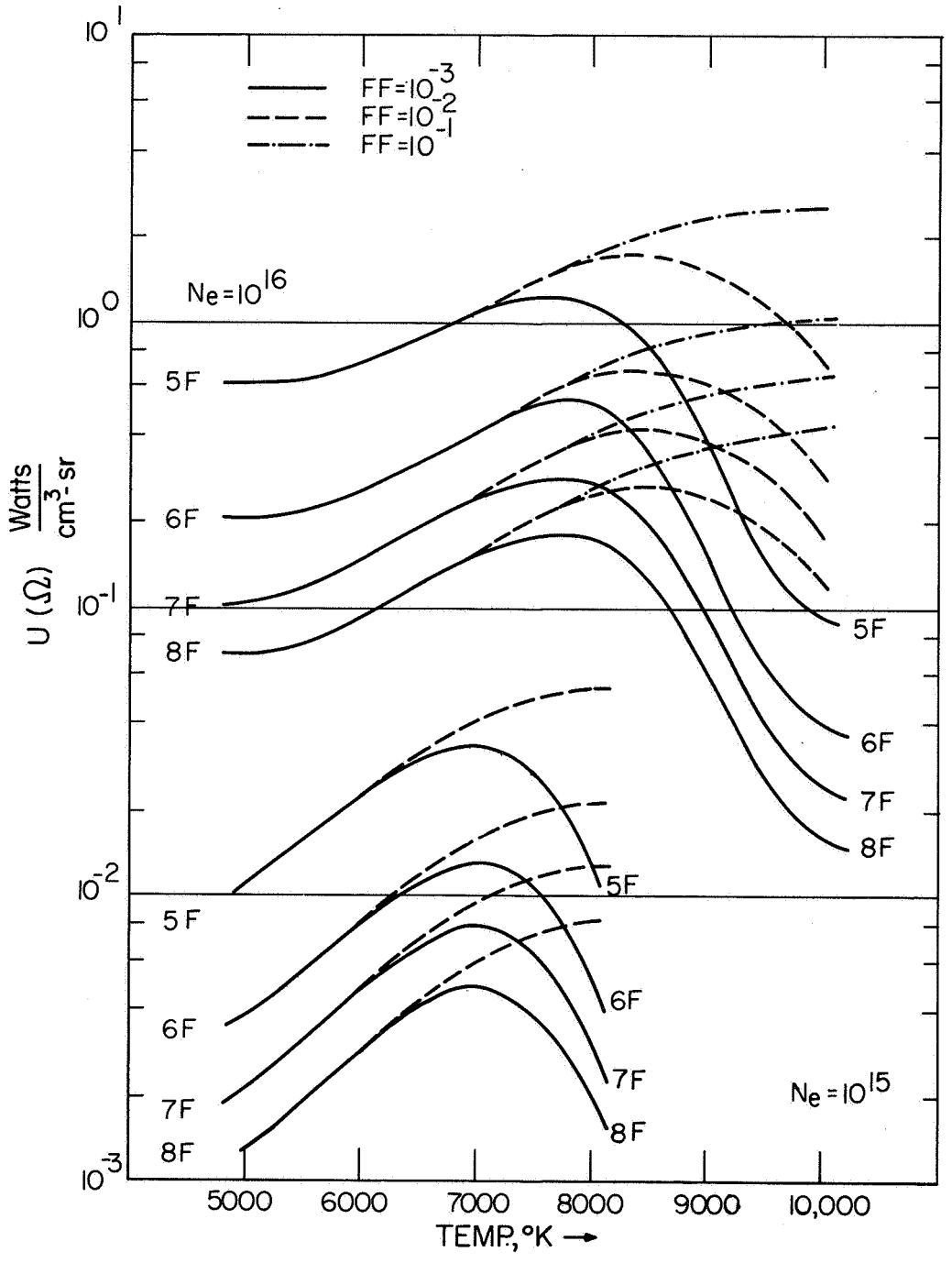

FIG. 22 $5D_{5/2}$, nF cesium line intensities at $Ne = 10^{15}/cm^3$ and $10^{16}/cm^3$.

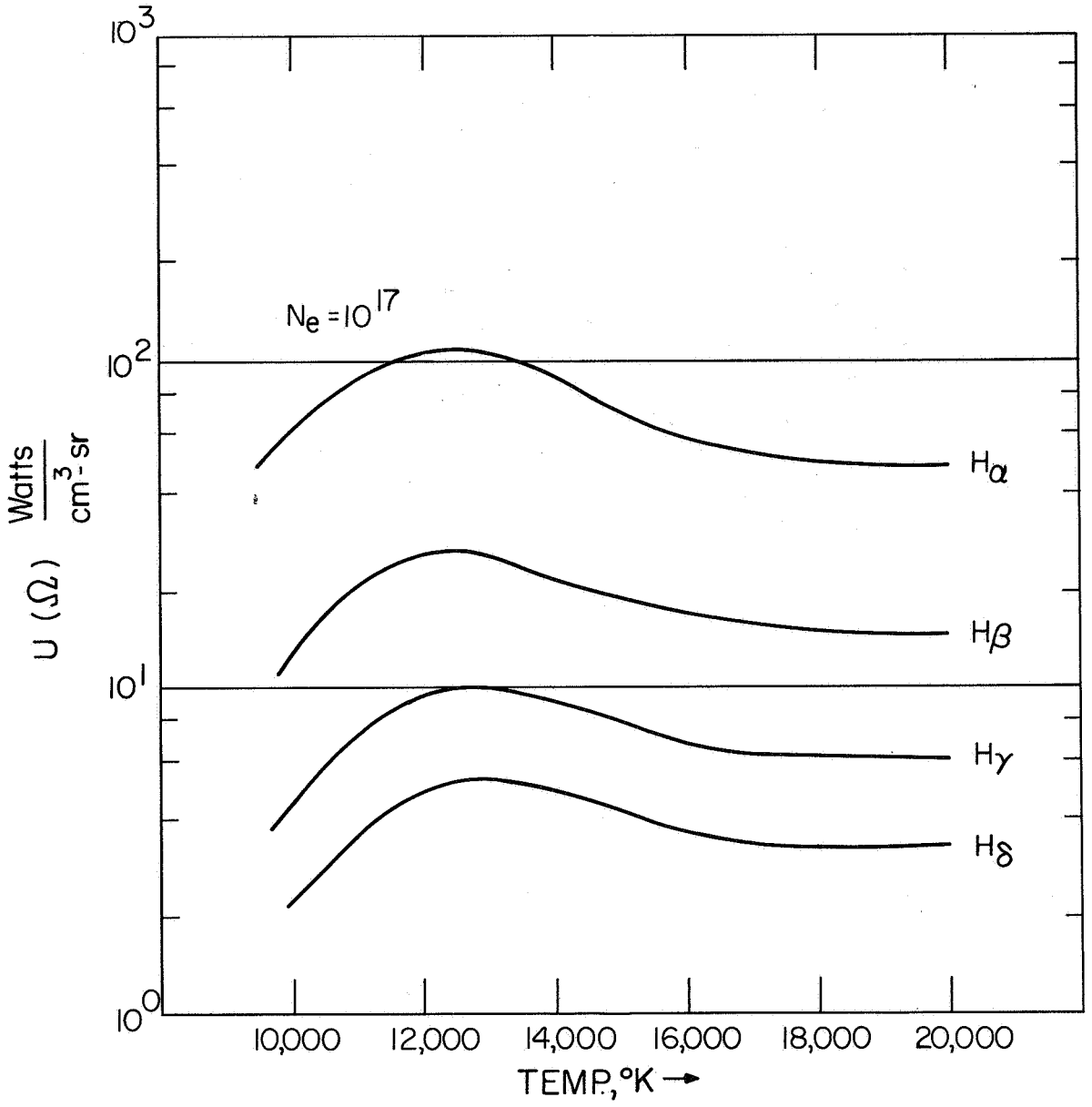

FIG. 23 Hydrogen line intensities at $Ne = 10^{17}/cm^3$ and $FF = 10^{-2}$. For other densities and seed fractions refer to Table VIII.

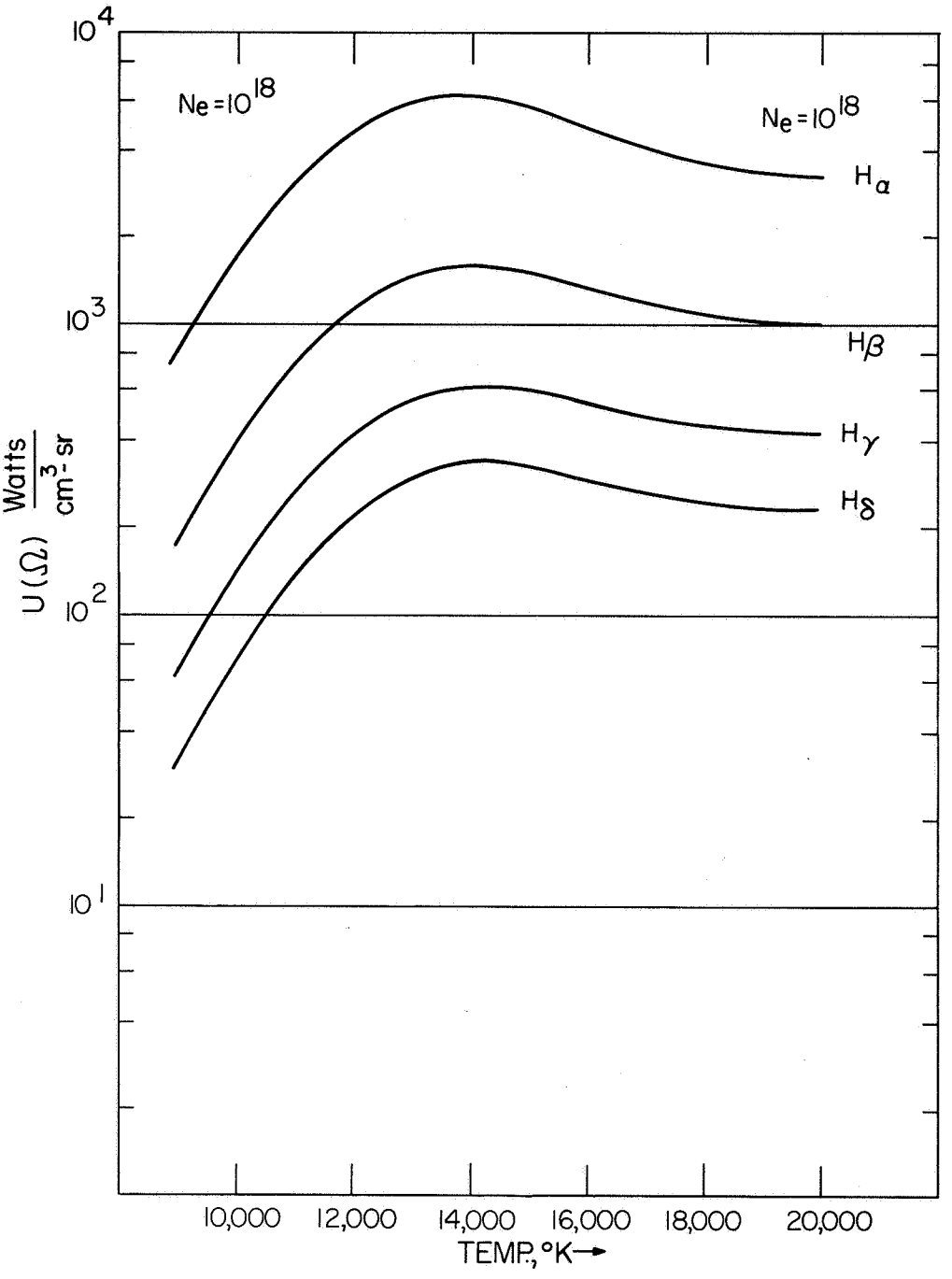

FIG. 24 Hydrogen line intensities at $Ne = 10^{18}/cm^3$ and $FF = 10^{-2}$. For other densities and seed fractions refer to Table VIII.

plasma. The procedure is not suitable for lines because the curves in this section do not show the detailed line shape. The continua between lines are suitable.

The power density emitted per unit solid angle and unit frequency interval from a system whose excited state populations are in equilibrium is given by Kirchoff's law as

$$j(\nu,\Omega) = k(\nu)\ B(\nu,T)\ \text{erg/cm}^3\text{-sec-Hz-sr} \tag{36}$$

The Planck function

$$B(\nu,T) = \frac{2h\nu^3}{c^2}\left(\frac{1}{e^{h\nu/kT} - 1}\right) \tag{37}$$

is tabulated in many places.[2]

The procedure is to choose a convenient frequency interval and to make an absolute measurement of $j(\nu,\Omega)d\nu$. The temperature can be deduced from knowledge of $k(\nu)$ and $B(\nu,T)$ as a function of temperature. The most sensitive region of the spectrum for the temperature range we are considering is from 1500 Å - 3000 Å, giving energy densities emitted from the plasma on the order of 10^{-6} W/cm^3-sr in a 1 Å interval.

Relative continuum measurements—that is, the shape of the continuum—can also be used to deduce temperatures. In this case the shape must be compared with the shape given by the $k(\nu)B(\nu,T)$ product.

F. SUMMARY AND CONCLUSIONS

This section has provided data and formulae to perform spectroscopic temperature measurements of cesium seeded high temperature hydrogen gas. Particular lines have been selected as most suitable over the 5000 - 20,000°K range, and their Stark broadened width, line center absorption coefficient, and emission energy density have been calculated. A procedure has been described using this information to determine temperatues. Continua can also be used in conjunction with Sec. III, part B to determine temperature.

Below 10,000°K the cesium lines of Table V are suitable for determining temperature. Above 10,000°K the lines are broadened and overlap. However, the Balmer lines of hydrogen can be used at the higher temperatures. The lines must be optically thin to determine temperature accurately and Table VII can be used to check the optical depth for the particular experimental arrangement.

IV. ARC JET

The art-jet facility consists of two main components: the arc jet itself and a ballast resistor. Separate from this is a straightforward three-phase full-wave-rectified power supply designed to deliver 200 A at 560 V in continuous operation. Three 37.5 kVA transformers are used to achieve this capability. A block diagram of the power supply is shown in Fig. 25. The main feed-current sensor and the low-voltage control and interlock system are provided to protect other equipment on the line which can fail catastrophically when power is shut off. These units sense the primary line current and will shut the arc down before tripping the main breaker when the line is overloaded. The rectifier consists of six 250 A silicon diodes. The ripple at the output of the rectifier is about 5 percent. This is reduced to 0.5 percent in the ballast and main filter section, which should prove adequate for our purposes.

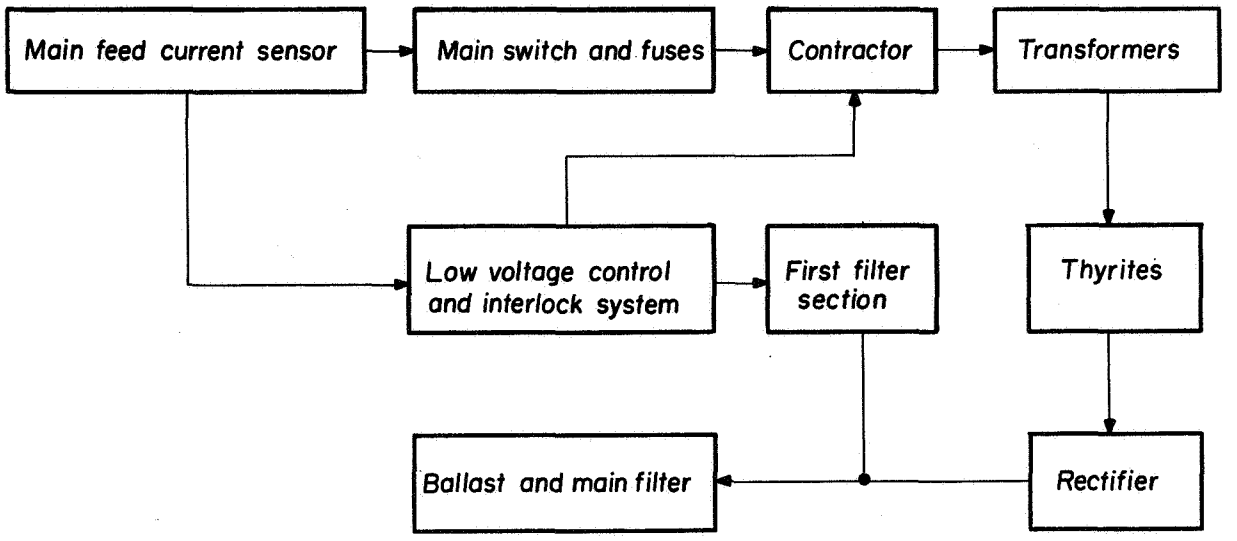

FIG. 25 Block diagram of 112 kW power supply.

Since the supply is unregulated, a variable ballast resistor is required to set the current. Because of the large amount of power which must be dissipated in this resistor, considerable effort has gone into the design in order to keep the cost within reasonable limits. The ballast resistor as designed is a three-decade device having tenths, units, and tens. In turn, each decade is made up in four sections having the value of one, two, three and four, with appropriately sized switches to short out unnecessary sections. The actual resistors are made from vitreous power units run in water. The power dissipation was calculated for the short circuit case at the 200 A maximum current. To maintain electrical isolation, a closed-loop system employing distilled water and a water-to-water heat exchanger is used. The actual container for the resistor bank is a polyethylene tank measured $2 \times 2 \times 3$ feet which is filled with 33 gallons of water and 3 pints of methanol, the latter to inhibit growth of algae. This tank and its associated heat exchanger and pump are mounted on wheels and become the bench that the arc jet is mounted on as shown in Fig. 26. All metering and controls for the main supply are included. Power and cooling water for the heat exchanger from the "house" lines are brought to it with flexible lines, assuring that the unit can be moved about to get optimum placement with respect to the optical equipment used for measurements.

The arc jet itself represents a considerable departure from our original design, which was quite similar to that described by Bott (Ref. 17). We have altered this basic design to incorporate the gas-flow techniques used by Morris et al (Ref. 18). A close-up photograph of the arc jet with hoses for gas and cooling water is shown in Fig. 27. In this system the cathode and anode areas are maintained in an atmosphere of argon and the center section contains the test gas. This is necessary when a chemically active gas such as air is being studied, since erosion of the anode can cause unstable operation and failure when air is allowed to enter the anode volume. The manner in which the test gas is excluded from the electrodes is

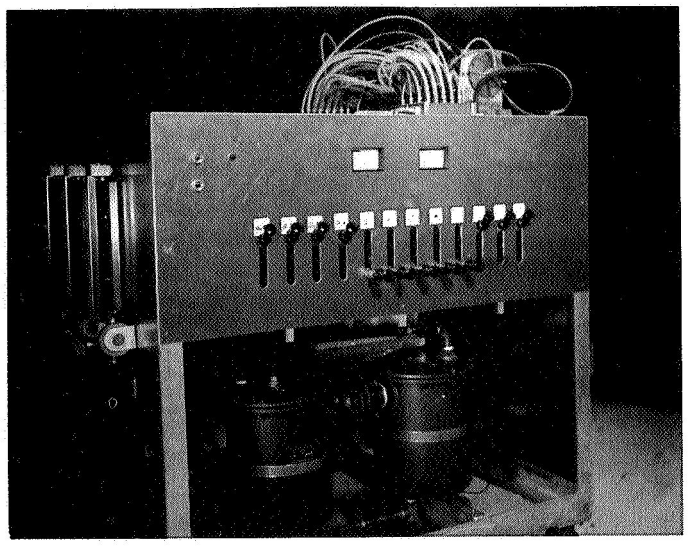

FIG. 26 Photograph of arc jet and auxiliary equipment. Part of the front panel is removed to show the heat exchanger. The switches determining the magnitude of the ballast resistor are "on" in the down position. The size of the individual resistors, from left to right, is 0.1, 0.2, 0.3, 0.4, 1, 2, 3, 4, 10, 20, 30, and 40 ohms, respectively. Three gas flow meters are mounted on the left side of the cart.

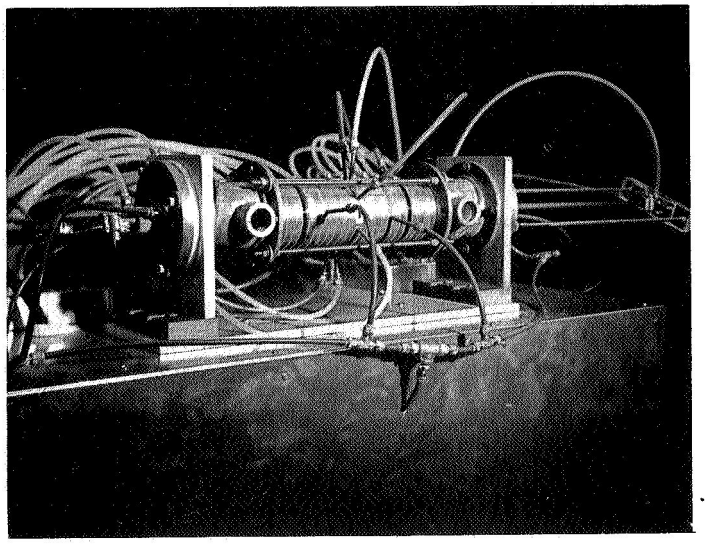

FIG. 27 Close-up photograph of arc jet. Before ignition of the arc the movable cathode (the electrode to the right) is in mechanical contact with the anode. The color code used on the hoses is blue for water inlets, white for water outlets, and green for gas inlets.

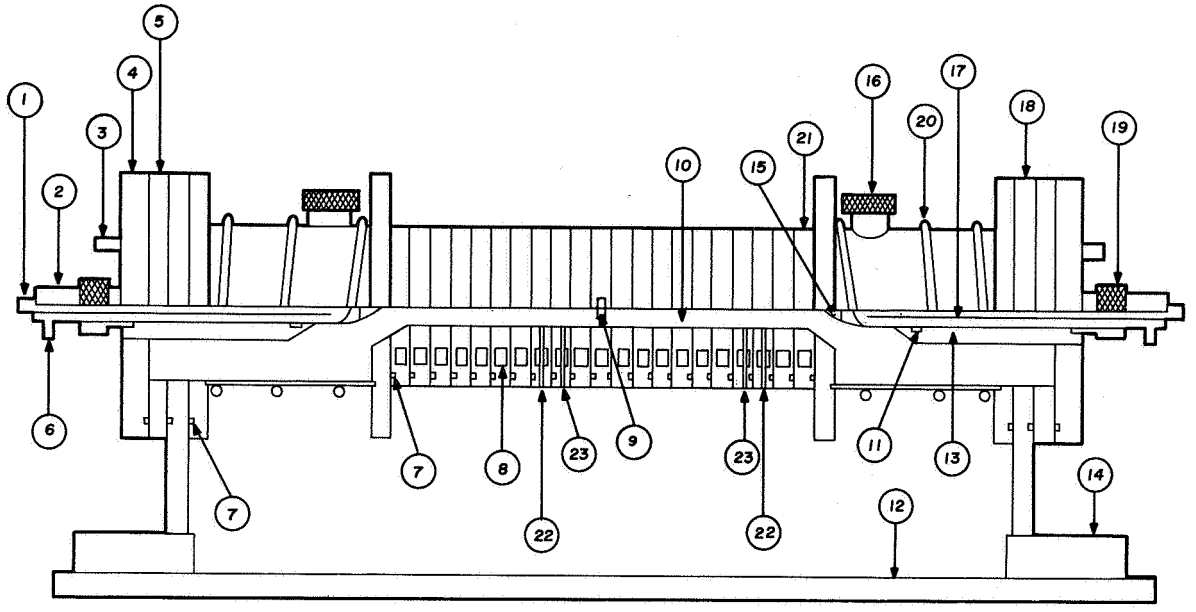

1 ELECTRODE COOLING WATER INLET
2 ELECTRODE BODY
3 END VOLUME GAS INLET
4 END PLATE
5 TEFLON INSULATING RING
6 ELECTRODE COOLING WATER OUTLET
7 "O" RING GAS SEALS
8 COOLING WATER PASSAGES
9 VIEWING PORT
10 ARC PASSAGE
11 ELECTRODE "O" RING SEAL & GUIDE
12 BASE PLATE
13 ELECTRODE SUPPORT
14 INSULATING ADJUSTABLE SPACER BLOCK
15 TUNGSTEN ELECTRODE TIP
16 END VOLUME VIEW PORT
17 ELECTRODE INNER COOLING WATER TUBE
18 SUPPORT PLATE
19 OUTER ELECTRODE SEAL & GUIDE
20 END VOLUME COOLING COILS
21 NOZZLE DISC
22 GAS EXHAUST PORTS
23 CTR. COLUMN GAS INLET PORTS

FIG. 28 Quarter-section schematic diagram of redesigned arc jet.

best described by reference to Fig. 28, which is a quarter-section schematic diagram of the arc. It can be seen that the arc jet is symmetrical. The inert gas enters the cathode and anode volume at 3 and is allowed to fill the chamber, leaving at the exhaust ports 22 located in the arc discs. The gas flow is approximately 1 standard cubic foot per minute. The arc is started by shorting the cathode and anode together and drawing them apart. A ballast resistor of 20 ohms is used during the starting period; this is decreased to 8 ohms as the electrodes are separated, giving a stable current of 50 A in argon. After the arc has stabilized the test gas (air or nitrogen) is admitted at the inlet ports 23 and the flow is increased until the spectrum indicates that none of the inert gas is left in the portion of the arc column being observed. This procedure eliminates the problem of attack at the electrodes, since only inert gas is located in that area. If desired, the arc can be operated in the conventional manner by sealing the inlet and outlet ports in the discs and allowing the gas to flow in at the cathode and exit at the anode, as was done in the low power prototype arc jet which was built during the first phase of the contract.

V. REFERENCES

1. Lasher, L. E., Wilson, K. H. and Grief, R.: Radiation from an Isothermal Hydrogen Plasma at Temperatures up to 40,000^{o}K, J. Quant. Spectry. Rad. Trans., Vol. 7, 1967, p. 305.
2. Allen, C. W.: Astrophysical Quantities, Athlone Press, University Press, University of London, 1964.
3. Olfe, D. B.: Equilibrium Emissivity Calculations for a Hydrogen Plasma at Temperatures up to 10,000^{o}K, J. Quant. Spectry. Rad. Trans., Vol. 7, 1967, p. 104.
4. Quarterly Progress Report No. 4, Contract No. NAS 12-86, Sperry Rand Research Center Report No. SRRC-CR-67-27.
5. Green, L. G., Rush, P. P. and Chandler, C. D.: Oscillator Strength and Matrix Elements for the Electric Dipole Moment for Hydrogen, Astrophys. J. Suppl. Series, Vol. 3, 1967, p. 37.

6. Bates, D. R. and Damgaard, A.: The Calculation of the Absolute Strengths of Spectral Lines, Phil. Trans. Roy. Soc. London, Vol. A242, 1949, p. 101.
7. Aller, L. H.: Astrophysics, 2nd ed., Ronald Press, N. Y., 1963.
8. Norcross, D. W. and Stone, P. M.: Radiative Recombination in Cesium, J. Quant. Spectry. Rad. Trans., Vol. 6, 1966, p. 277.
9. Griem, H. R.: Plasma Spectroscopy, McGraw Hill Book Co. Inc., N. Y., 1964.
10. Karzas, W. J. and Latter, R.: Electron Radiative Transitions in a Coulomb Field, Astrophys. J. Suppl., Vol. 6, 1961, p. 167.
11. Quarterly Progress Report No. 6, Contract No. NAS 12-86, Sperry Rand Research Center Report No. SRRC-CR-67-58.
12. Burgess, A. and Seaton, M. J.: A General Formula for the Calculation of Atomic Photoionization Cross Sections, Monthly Notices Roy. Astron. Soc., Vol. 120, 1959, p. 9.
13. Burgess, A.: Tables of Hydrogenic Photoionization Cross Sections and Recombination Coefficients, Memoirs Roy. Astron. Soc., Vol. 69, Part I, 1964.
14. Moore, C. W.: Atomic Energy Lines, Nat. Bur. Std. (U.S.) Circ. 467, 1949-1958, Vols. I, II and III.
15. Statz, H., Tang, C. L. and Koster, G. F.: Approximate Electromagnetic Transition Probabilities and Relative Electron Excitation Cross Sections for Rare-Gas Masers, J. Appl. Phys., Vol. 34, 1963, p. 2625.
16. Griem, H. R., Kolb, A. C. and Shen, K. Y.: Stark Broadening of Hydrogen Lines in Plasma, NRL Report 5455, 1960.
17. Bott, J. F.: A Spectroscopic Investigation of a Helium Plasma Arc, J. Quant. Spectry. Rad. Trans., Vol. 6, 1966, p. 807.
18. Morris, J. C., Krey, R. V. and Bach, G. R.: The Continuum Radiation of Oxygen and Nitrogen for Use in Plasma Temperature Determination, J. Quant. Spectry. Rad. Trans., Vol. 6, 1966, p. 727.

APPENDIX A

ULTRAHIGH TEMPERATURE ELECTRONIC MEASURING TECHNIQUES

Final Report for the Period 1 December 1965
thru 30 November 1966
Contract No. NAS 12-86

NASA CR-
SRRC-CR-67-10

ULTRAHIGH TEMPERATURE ELECTRONIC MEASUREMENT TECHNIQUE

by

R. H. CURRY and P. M. STONE

MARCH 1967

Final Report for the Period 1 December 1965 thru 30 November 1966

Prepared Under Contract No. NAS 12-86

by

SPERRY RAND RESEARCH CENTER
SPERRY RAND CORPORATION
SUDBURY, MASSACHUSETTS 01776

NATIONAL AERONAUTICS AND SPACE ADMINISTRATION

TABLE OF CONTENTS

LIST OF ILLUSTRATIONS

SUMMARY

This investigation was undertaken in order to develop a real-time technique for the measurement of gas temperatures above 5000°K in an air or nitrogen plasma. The methods of temperature measurement considered were Doppler line broadening, line intensity ratios, line-to-continuum intensity ratios, and measurement of particle density with subsequent calculation of temperature. Each method was evaluated in terms of radiation available from an air plasma over the temperature range from 5000°K - 24,000°K at light densities from 10 times normal density to 10^{-6} times normal density. Two methods were found to cover this range adequately. These were line intensity ratios and Doppler broadening. The line-intensity-ratio method is only valid if equilibrium between the heavy particles and the electrons—such as in shock tubes after equilibration has taken place or in electrical discharges at high pressures and moderate electrical fields—can be expected. The method also fails at electron densities below $10^{15} - 10^{16}/cm^3$ because of departures from equilibrium between the excited-states and the free electrons. At high atom densities the effects of self-absorption must be taken into account. Doppler line broadening is a direct measure of gas temperature and can be used whenever optically thin lines are available whose shapes are dominated by the Doppler effect. Stark broadening due to electrons has been found to be the only important competing broadening mechanism, and is important only above electron densities of $10^{15} - 10^{16}/cm^3$. Thus, line intensity ratios can be used at high densities and Doppler broadening at lower densities. A real-time temperature-measuring system employing these methods would use photomultiplier tubes as detectors and incorporate an independent means of measuring electron density, such as Stark broadening or two-wavelength interferometry.

INTRODUCTION

The purpose of this investigation was to develop a real-time technique for the measurement of gas temperature above 5000°K in an air plasma over a wide range of densities. The specific techniques to be considered are Doppler line broadening, ratio of line intensities, ratio of line-to-continuum intensities, and measurement of particle density with subsequent calculation of temperature. Various instrumental approaches are considered, including a comparison of film and photomultiplier techniques, the use of microphotometry for spatial and time resolution, and the means of generating a laboratory plasma covering the desired range of temperature and density.

One of the major efforts in this study and the one on which most of the others depend is the calculation of the line emission spectrum and particle densities in equilibrium air between 5000°K and 24,000°K. Seven temperatures, each with eight total particle densities, were considered over this range. The highest density considered ($\rho/\rho_0 = 10$ at 24,000°K) was $6.24 \times 10^{20}/cm^3$, while the lowest ($\rho/\rho_0 = 10^{-6}$ at 5000°K) was $5.26 \times 10^{13}/cm^3$. Thus, 56 sets of data were obtained, each containing absolute intensities for 1584 lines of 14 constituents over the wavelength range from 3000 Å to 13,000 Å.

A literature search revealed that, although much work has been reported on the continuum radiation of heated air, little has been reported on line radiation. Recently, however, extensive oscillator strengths have been reported for the constituents of high-temperature air as well as Stark broadening parameters for these same constituents. In this study these values were used extensively in order to calculate line radiation. Self-absorption of spectral lines has been shown to be important only at high densities and temperatures. The line intensity ratio methods have been evaluated in terms of four criteria considered important in making accurate measurements. It has been shown that while the technique using lines from the same ionization stage of an element is useful at low temperatures, at high temperatures there is not a sufficient energy spread between upper excited states to provide adequate sensitivity for this method.

Line intensity ratios for lines from subsequent ionization stages of the same element can be used, however, as long as Saha equilibrium can be expected between the two levels of ionization. The meaning of the temperature measured by line-intensity-ratio methods is not always clear. If equilibrium between the free electrons and the excited states is expected, then line-intensity-ratio methods give the electron temperature T_e. This may not be equal to the gas temperature T_g, as is often the case for low-pressure electrical discharges or shocks where sufficient collisions have not taken place to equilibrate the various energy modes. The range of applicability of these assumptions has been assessed. Such considerations also apply to the measurement of line-to-continuum intensity ratios.

Of the methods of temperature measurement considered, only Doppler line broadening yields the gas temperature directly. Thus, considerable effort has been expended in order to define the exact limits of applicability of this technique. Stark broadening has been found to be the only

important competing line-broadening mechanism. Upper limits of the method have been assessed for each constituent, and Voight profiles have ben constructed for nitrogen to show the error caused in assuming a Doppler shape only at high electron densities.

Another important mechanism which can cause errors in the measured Doppler shape is the effect of instrument width. The importance of this mechanism has been assessed by the Voight method in order to determine the resolution requirements of the spectroscopic instruments to be used in an experimental study of Doppler-and Stark-broadened lines.

A general study of the limitations and advantages of both film and photomultiplier techniques has been made. The main concerns of this study were accuracy, time resolution capability, spatial resolution capability, importance of instrument effects, and applicability to real-time measurements. This conclusion of this study is that both techniques are useful in a general research program, while photomultiplier techniques would be used exclusively in any instrument designed to make real-time temperature measurements.

Work has been done on non-spectroscopic methods which depend on the macroscopic properties of the gas mixture. The two which appear most promising are the measurement of velocity of sound changes and measurement of refractive index changes. Consideration was given to measuring the composition of the gas by measurement of absolute intensities of the components. These measurements, along with the measurement of the electron density, provide a way of checking the equality of the electron and gas temperatures and the validity of other equilibrium assumptions.

Two experimental approaches appear most fruitful in experimentally verifying the calculations. These are the wall-stabilized arc jet and the electromagnetic T-tube. Prototypes of both of these diodes were constructed and operated. The former is a device which, in air, can generate a plasma having arc temperatures up to 15,000°K, while the latter is a type of shock tube capable of producing equilibrium shocks with temperatures in excess of 20,000°K. With these two devices, both types of deviations from equilibrium discussed above can be studied experimentally.

TECHNICAL DISCUSSION

Line Intensity Calculations

In conducting a program such as this, it is first necessary to define the plasma under investigation. To do this, we have chosen to use the work of Gilmore,[1] which contains a thermodynamic calculation of the composition of equilibrium air over the temperature range from 5000°K to 24,000°K and a wide range of densities. This calculation, although ten years old, is in satisfactory agreement with more recent work.[2,3] It takes into consideration 29 different molecular, atomic and ionic species as well as electrons. The standard density of air is taken as 1.2931×10^{-3} gm/cm^3. This value is still used in the most recent National Bureau of Standards calculations.[2] Gilmore's work was chosen over that of Moechel and Weston[3] because of the

inclusion of a greater number of species and more accurate presentation of data. The National Bureau of Standards' calculations extend only up to 15,000°K.

The data as presented by Gilmore are in tabular form. The concentration of each constituent is given as the number of particles per air atom for each temperature and density. In order to change these concentrations into particles per cm^3, the equation

$$N = 5.355 \times 10^{19} (\rho/\rho_p)\ \psi \qquad (1)$$

has been used, where ψ is the number of particles per air atom given by Gilmore. This manner of stating concentration is much more common in spectroscopic calculations and is necessary for direct use of most intensity equations. Table 1 lists the species considered and their concentrations at the highest and lowest total densities covered by the calculation.

To calculate the line emission spectrum of a given system, one must know the oscillator strengths of a great number of lines of each element. Fortunately, Griem[4] has recently published a series of calculated absorption oscillator strengths using the Coulomb approximation of Bates and Damgaard. This procedure is probably accurate to 20% for most of the elements of interest here. Serious deviations from L-S coupling are found in OII and ArII, causing inaccuracies in the oscillator strengths for these ions. We have used these oscillator strengths except for ArII and for some transitions in ArI where experimental values were used instead. The statistical weights and excitation energies of all of the lines are those given by Moore.[5]

The emitted intensity, I, in watts/cm^3-sr is given by

$$I = \frac{2\pi e^2 h}{m\lambda^3} N_U \frac{g_L}{g_U} f_{LU} \qquad (2)$$

where subscripts L and U refer to the lower and upper states, respectively, and f_{LU} is the absorption oscillator strength. N_U is the population of the upper state and (in equilibrium) is given by

$$N_U = \frac{g_U}{g_1} N_1 e^{-E_U/kT} \qquad (3)$$

where N_1 is the number density of the ground state atoms and E_U is the energy of the upper state.

TABLE 1

CONSTITUENTS OF HIGH TEMPERATURE AIR

Constituents	N (Max)	N (Min)	λ(Å)
C	6.21(16)	6.75(9)	10,691.40
C^+	2.32(16)	1.30(9)	6,578.00
N	3.42(20)	4.00(13)	8,680.20
N^+	7.49(19)	1.28(10)	5,679.60
N^{++}	4.99(15)	8.03(-10)	4,097.30
N^{+++}	1.97(7)	-	3,478.70
O	9.69(19)	1.13(13)	7,772.00
O^+	1.48(19)	6.48(9)	4,649.10
O^{++}	3.46(14)	3.41(-15)	3,759.90
O^{+++}	1.14(5)	-	3,063.50
Ne	1.03(16)	1.07(9)	6,402.20
Ne^+	3.51(14)	7.44(-2)	3,694.20
Ar	1.73(18)	2.51(11)	8,115.30
Ar^+	7.82(17)	1.18(7)	4,348.10
O^-	5.03(17)	3.26(3)	
Ar^{++}	4.60(14)	1.69(-10)	
CO_2	-	2.29(1)	
NO_2	-	3.74(-1)	
O_3	-	1.74(-5)	
CO	1.18(14)	5.06(8)	
CO^+	4.66(13)	4.99(4)	
N_2	8.19(17)	1.00(12)	
N_2^+	3.79(17)	4.03(7)	
NO	2.93(17)	6.80(8)	
NO^+	2.43(17)	4.58(9)	
O_2^-	4.89(14)	4.99(-4)	
O_2	3.56(16)	1.79(6)	
O_2^+	1.77(16)	4.96(4)	
e^-	9.06(19)	2.52(10)	

Substituting the value for N_U in Eq. (3) and evaluating the constants, we obtain

$$I = 1.0542 \times 10^7 \frac{g_L f_{LU} N_1 e^{-E_U/kT}}{g_1 \lambda^3} \qquad (4)$$

A computer program was written for calculations of N_1 using Gilmore's data and Eq. (1), the excited state populations from Eq. (3), and the intensities of each line from Eq. (4). All of the composition data, oscillator strengths, statistical weights, and energy level data used in these calculations have been placed on punch cards and are available for future use.

Intensity calculations were performed for the following temperatures: 5000°K, 6000°K, 7000°K, 8000°K, 12,000°K, 18,000°K and 24,000°K. For each temperature, densities (ρ/ρ_0) of 10, 1, 10^{-1}, 10^{-2}, 10^{-3}, 10^{-4}, 10^{-5}, and 10^{-6} were considered. Of the 29 constituents listed in Table 1, only the first 14 emit line radiation. Column three of this table gives the wavelength of the strongest line of each element. The intensities of these lines are plotted as a function of temperature for each of the densities in Figs. 1-8.

Comparison of Fig. 1 with the composition data reveals some interesting similarities and differences. Most noteworthy is the difference in the behavior of the intensity of ArI and ArII. Although the ArI concentration remains relatively constant over most of the temperature range, the intensity of the ArI line at 8115.30 Å increases more than ten orders of magnitude due to the temperature increase. The increase in intensity of the ArII line at 4348.10 Å is even more striking. The most striking difference between the intensity data for the high density case and those for the low density case shown in Fig. 8 is the increase in the intensity of ionized species relative to neutral species. Thus, above 14,000°K, the most intense lines in the spectrum are those of NII rather than NI as in the high density case. The Ar lines show quite different behavior in the low density case. Here the ArI line does not continue to increase with temperature, but reaches maximum intensity at about 11,000°K and then begins to decrease. The ArII line increases in intensity up to about 17,000°K and then remains nearly constant. The over-all intensity is much greater in the high density case. At high densities and temperatures the possibility of self-absorption must be considered for the strongest lines.

Although it is generally assumed that lines that do not terminate in the ground state, are fairly broad, and do not suffer seriously from self-absorption, the assumptions should always be checked. This has been done in the present case by the following method: A general equation for the intensity of a spectral line [$I(\nu)$] is:

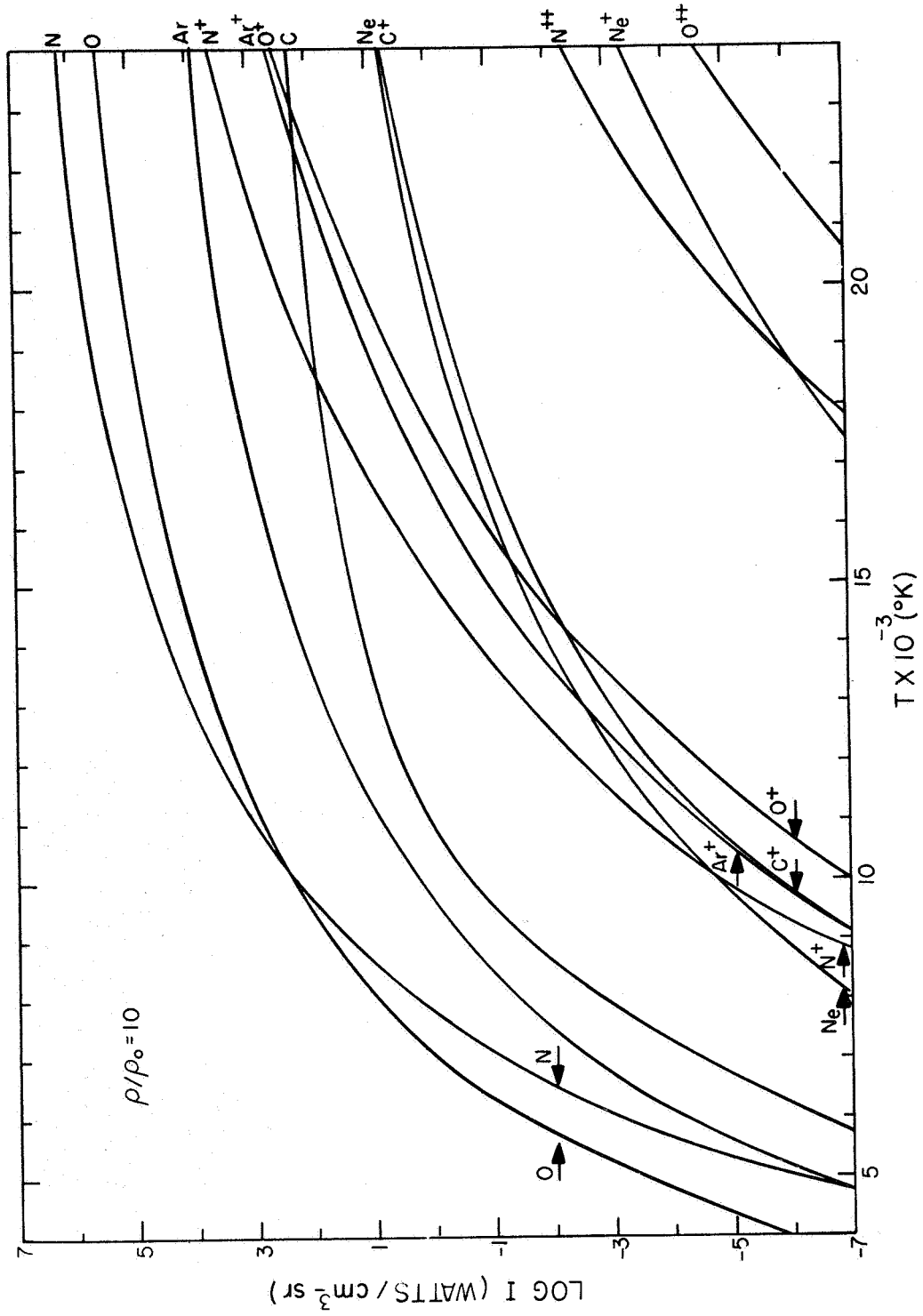

Figure 1 Intensity of strongest lines of hot equilibrium air at a density $\rho/\rho_o = 10$ from 5000 - 24000°K.

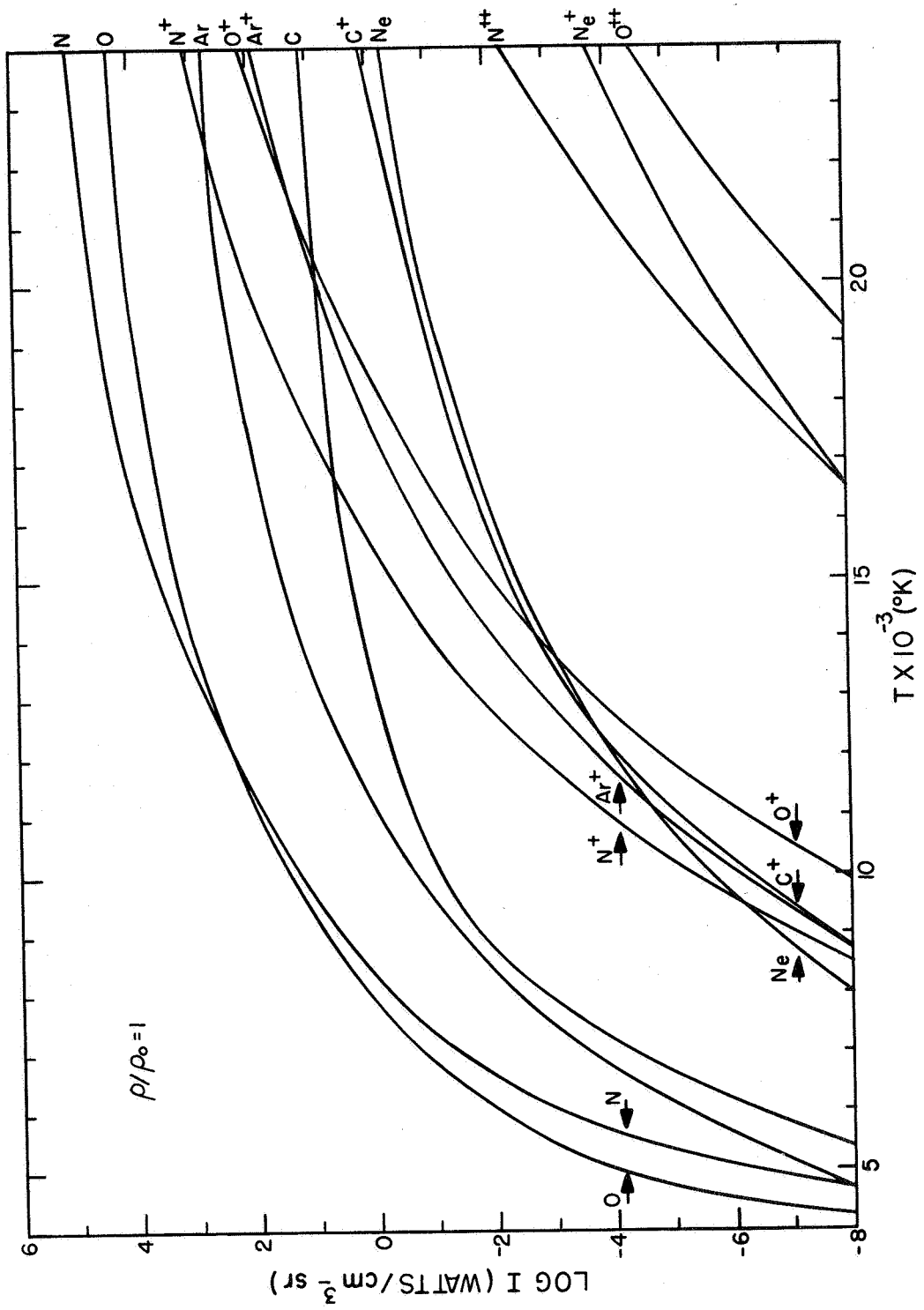

Figure 2 Intensity of strongest lines of hot equilibrium air at a density $\rho/\rho_o = 1$ from 5000 - 24000°K.

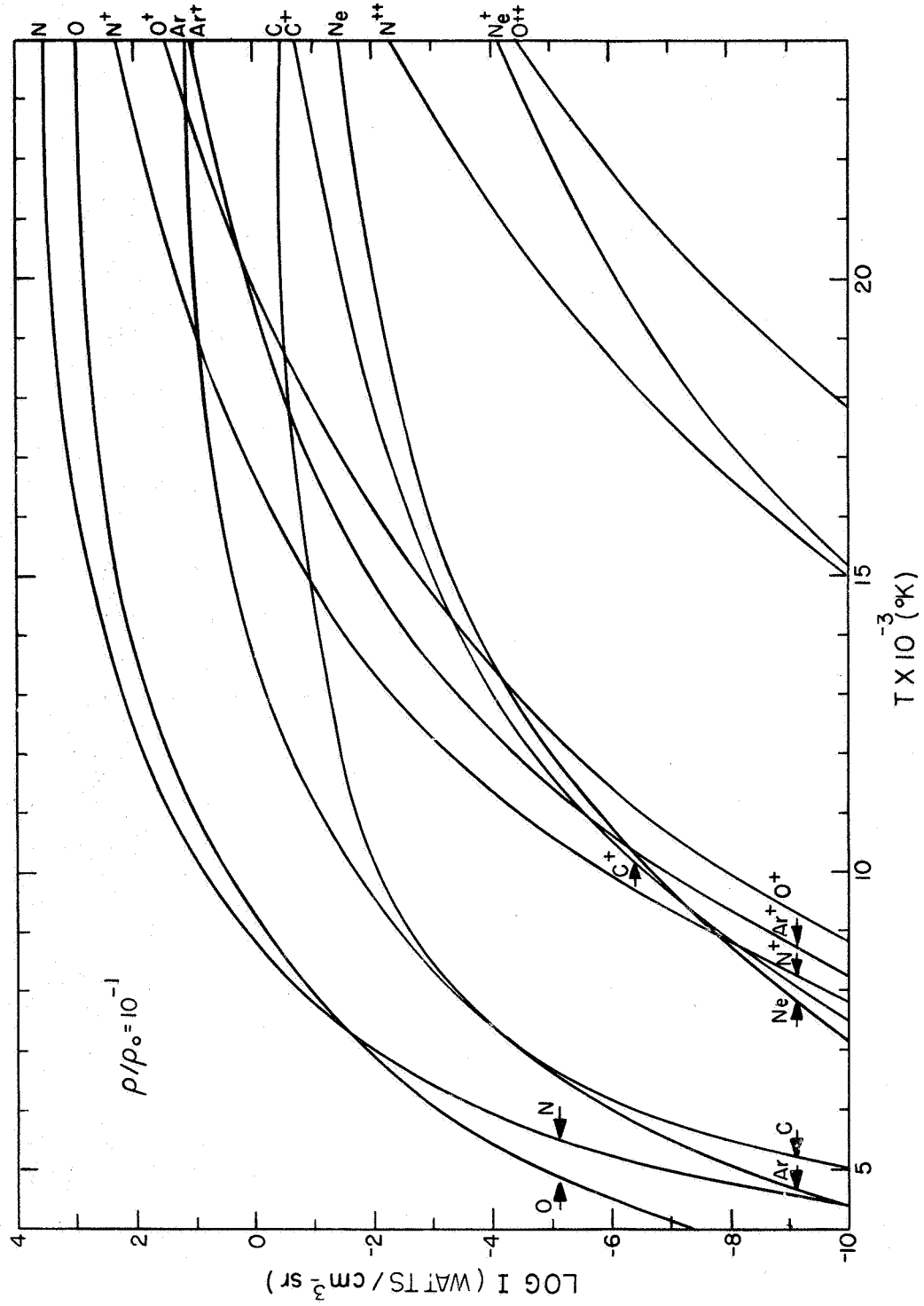

Figure 3 Intensity of strongest lines of hot equilibrium air at a density $\rho/\rho_0 = 10^{-1}$ from 5000 - 24000°K.

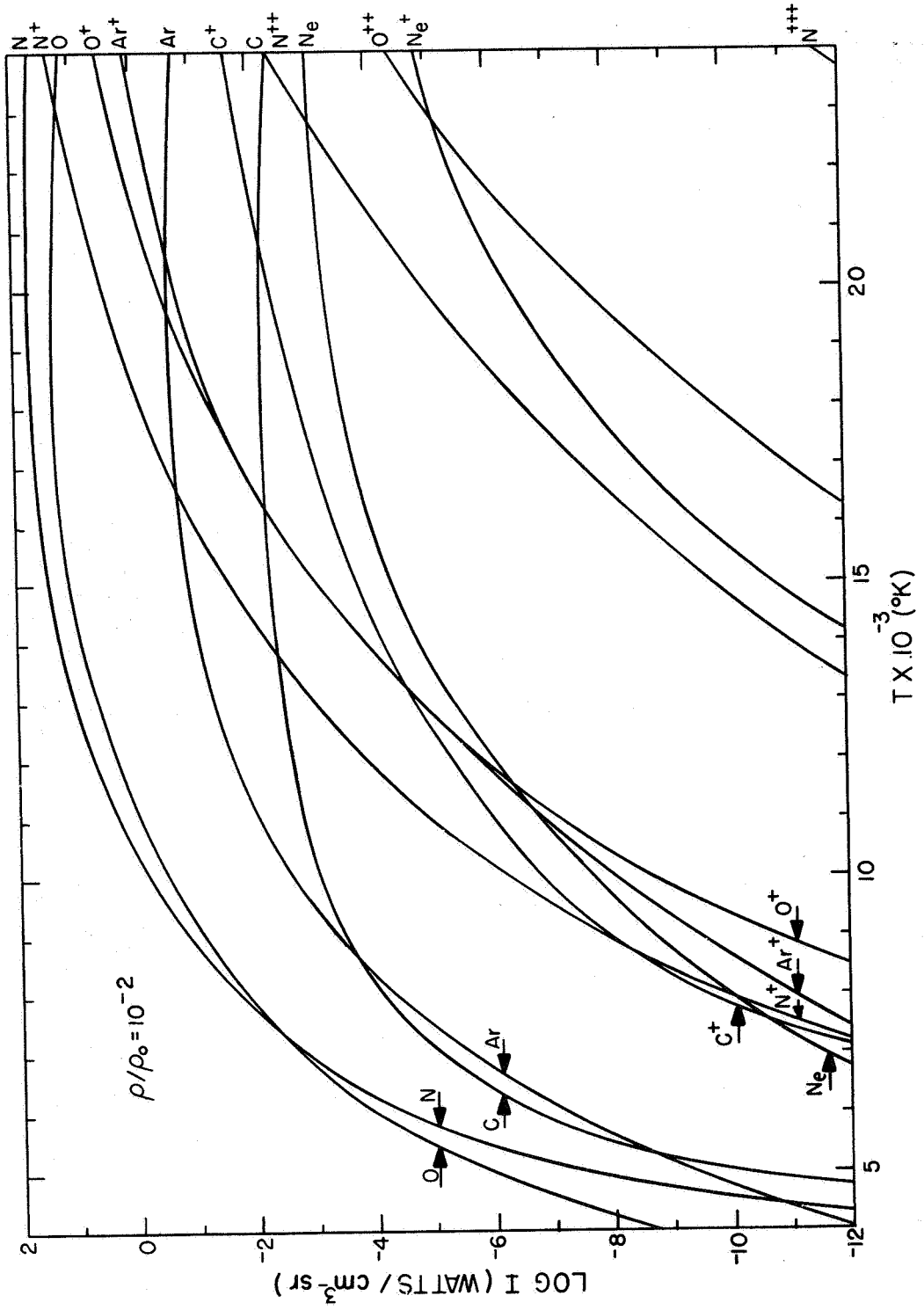

Figure 4 Intensity of strongest lines of hot equilibrium air at a density $\rho/\rho_o = 10^{-2}$ from 5000 - 24000°K.

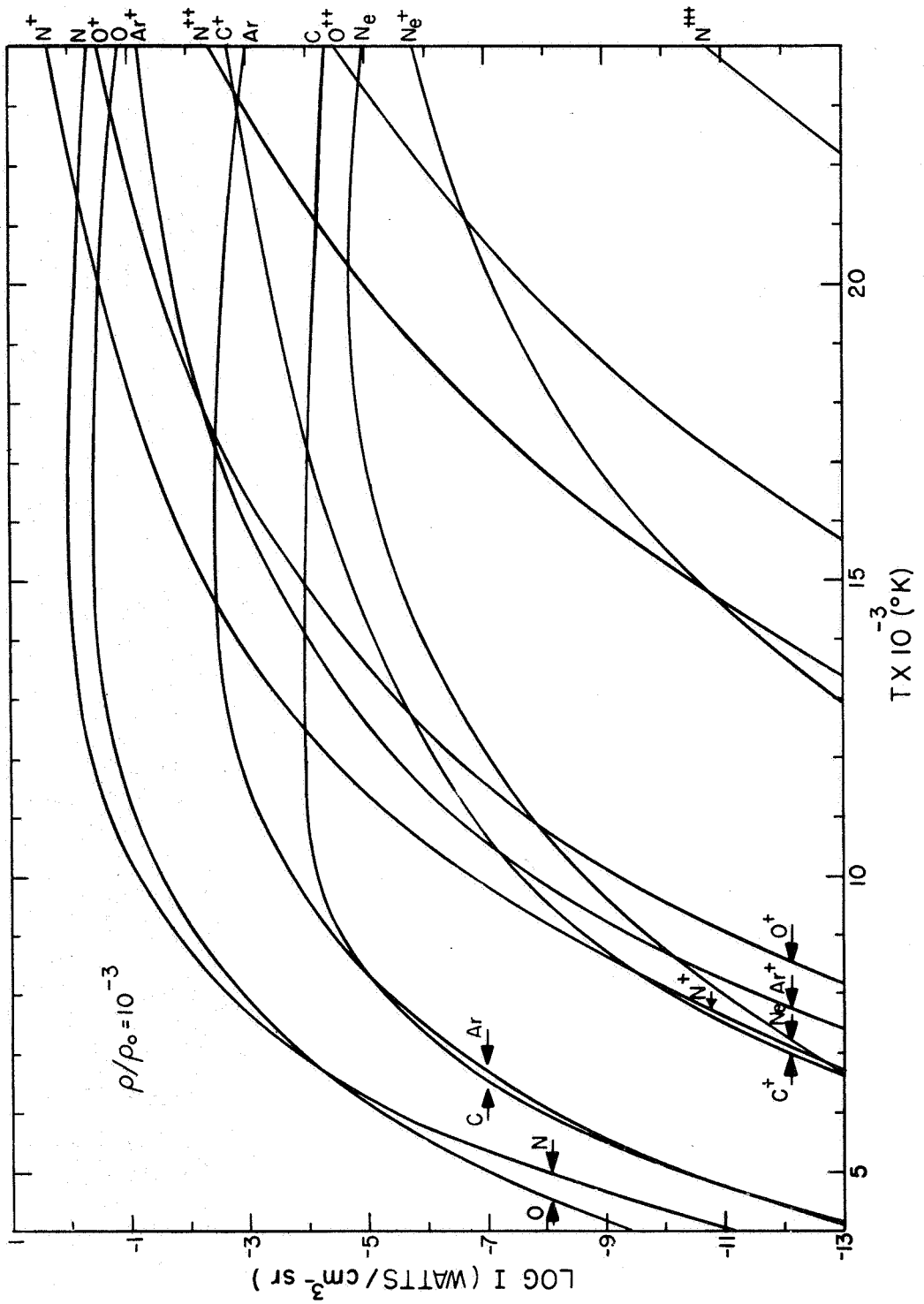

Figure 5 Intensity of strongest lines of hot equilibrium air at a density $\rho/\rho_o = 10^{-3}$ from 5000 - 24000°K.

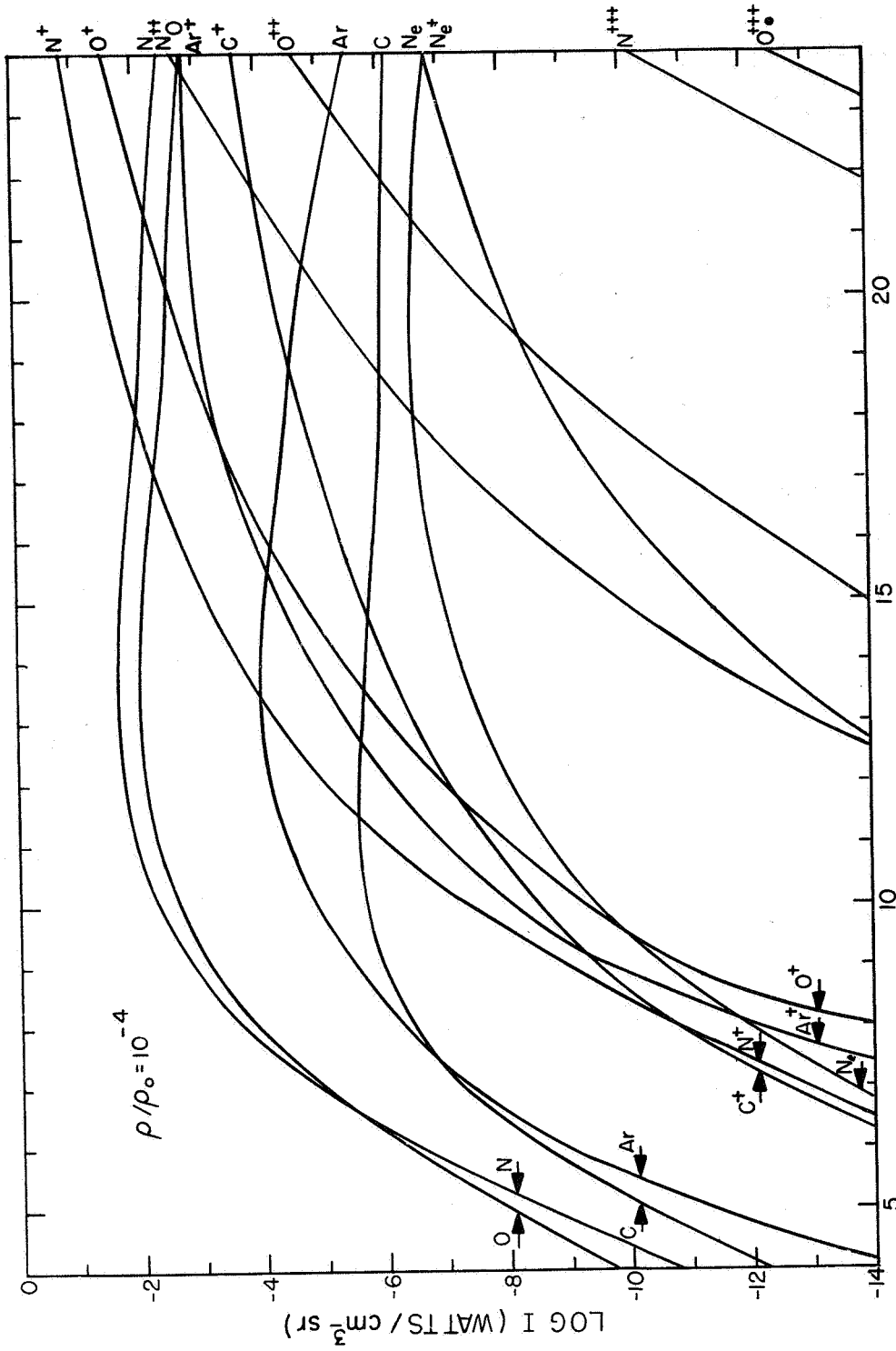

Figure 6 Intensity of strongest lines of hot equilibrium air at a density $\rho/\rho_0 = 10^{-4}$ from 5000 - 24000°K.

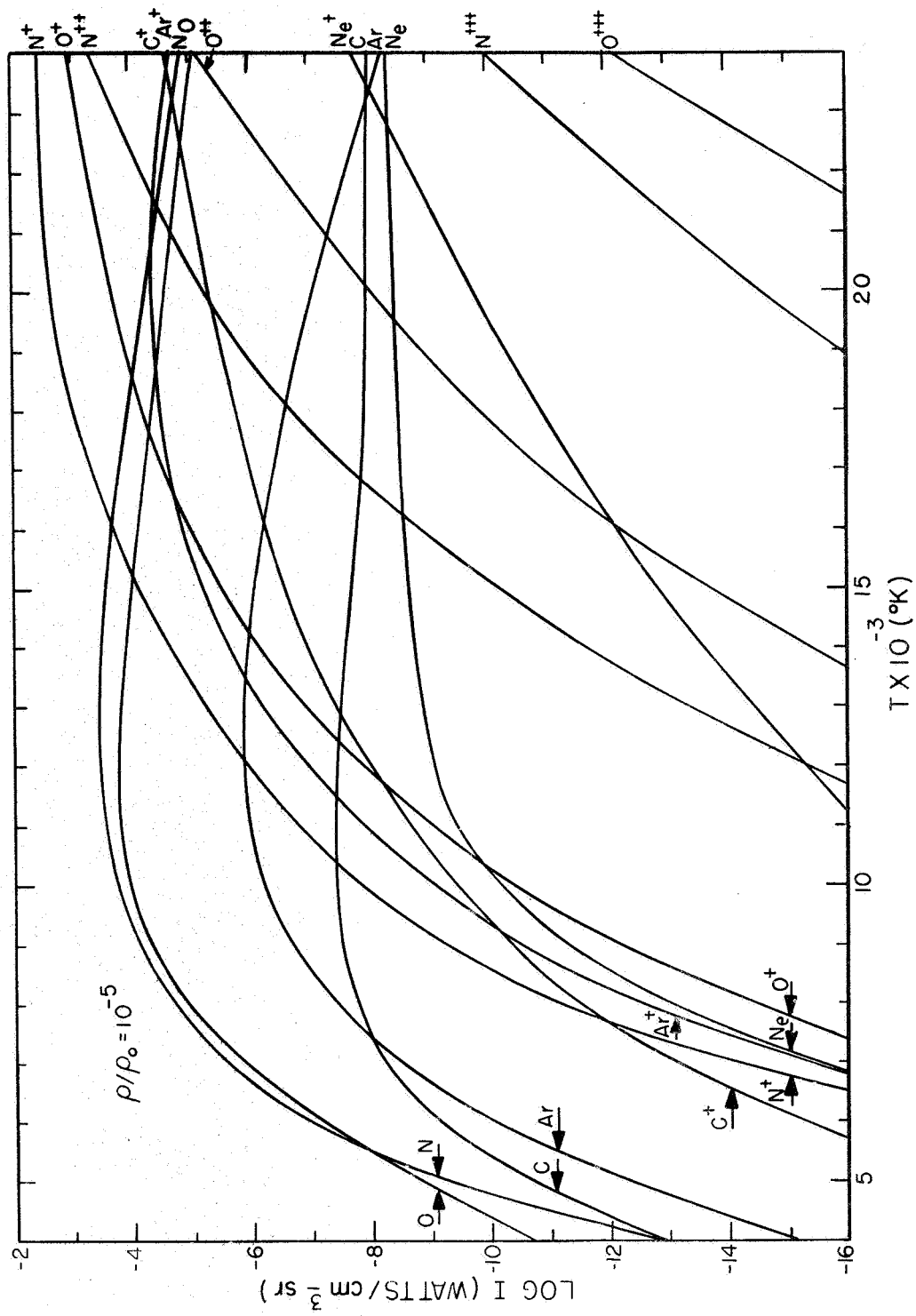

Figure 7 Intensity of strongest lines of hot equilibrium air at a density $\rho/\rho_0 = 10^{-5}$ from 5000 - 24000°K.

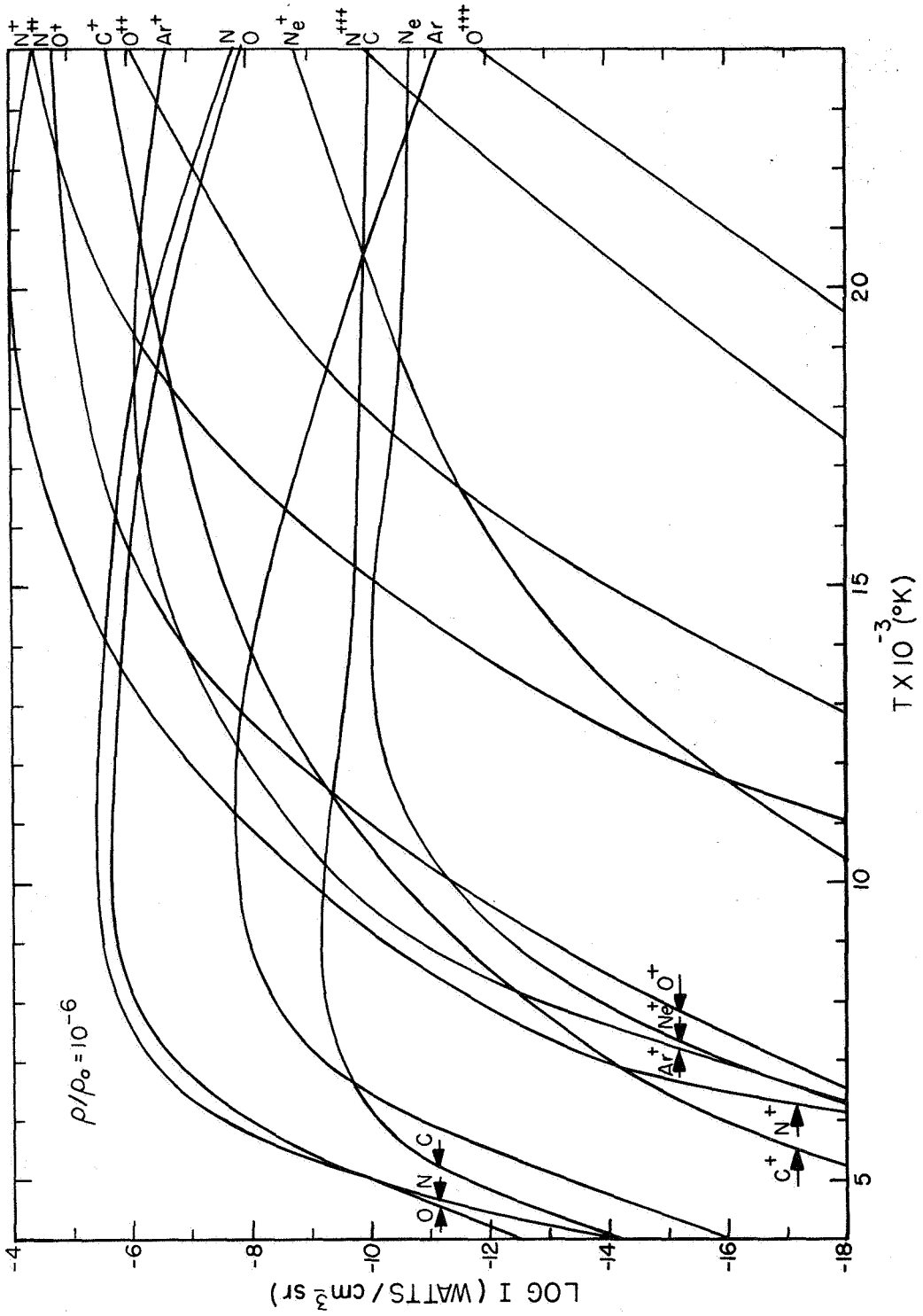

Figure 8 Intensity of strongest lines of hot equilibrium air at a density $\rho/\rho_o = 10^{-6}$ from 5000 - 24000°K.

$$I(\nu) = \frac{AN_U}{BN_L}\left(1 - e^{\frac{-h\nu N_L S(\nu)Bx}{4\pi}}\right) \qquad (5)$$

where A and B are the Einstein emission and absorption coefficients, respectively; N_U and N_L are the populations of the upper and lower states; ν is the frequency of the line; x is the path length; and $S(\nu)$ is the shape function of the line. If the exponent is small with respect to unity, then, to first order, the optically thin result which is equivalent to Eq. (2),

$$I(\nu) = \frac{h\nu\, N_U A\, S(\nu)x}{4\pi} \qquad (6)$$

is obtained by expansion. If the exponent is large, the intensity will obtain a maximum value

$$I(\nu) = \frac{N_U A}{N_L B} \quad , \qquad (7)$$

which is the blackbody intensity at frequency ν and the temperature corresponding to N_U/N_L.

Thus, in order to evaluate the importance of self-absorption it is necessary to evaluate the magnitude of the exponent in Eq. (5). To do this, we approximate the line shape as a square shape of width $1/\Gamma$. Substituting and evaluating Eq. (5) in terms of f value, we get

$$\frac{h\nu N_L Bx}{4\pi\Gamma} = 7.13 \times 10^{-22}\, \frac{\lambda^2 f N_L x}{\Delta\lambda} \qquad (8)$$

where $\Delta\lambda$ is the width in angstroms, which for a Stark broadened line in nitrogen is given to a sufficient approximation by $10^{-18}\, N_e$. It can be seen from this equation that wide lines will be absorbed less than narrow ones. The lines which have been chosen for our conditions of neutral density, electron density, and temperature all have values for the exponent which indicate that self-absorption may be important at ρ/ρ_0 values greater than unity at high temperatures. Corrections can be made for self-absorption if it does not become too severe. In any event, at high temperatures and densities, many lines of each element are available for intensity measurements. Self-absorption can be minimized or eliminated by choosing lines having low oscillator strengths. Recently Churchill et al.[6] have published absorption coefficients

(the experiment in Eq. (5)) of heated air due to molecular free-free and free-bound contributions. However, they averaged over photon energy spreads of 0.10 eV, and thus their data are not directly applicable to the present problem. In general, their data indicate quantitatively that these types of absorption will be of little consequence for reasonable path lengths. Their work is also based on Gilmore's composition data.[1]

Line Intensity Ratios

A number of spectral lines have been chosen for relative-intensity temperature measurement according to the following criteria:

(1) Freedom from self-absorption

(2) Freedom from spectral interference

(3) Sufficient intensity throughout temperature and density range

(4) Maximum spread in excitation energy.

In addition to this, lines have been chosen which lie within the useful range of present day photocathodes and spectroscopic films (3000 Å to 9000Å).

Table 2 gives a list of lines which are suitable for use in temperature measurement. These lines were all found to be suitably intense over a wide range of densities and temperatures and, within the limits described above, free from self-absorption. In addition, they are free from spectral interference and fall in the most workable region of the spectrum. Even though these lines appear to be the best according to the above criteria, this list cannot be considered exhaustive. Other lines may be just as good or better, especially at high temperatures and densities.

Also listed in Table 2 are the upper state energies of the lines. Since the measurement of temperature using lines from the same ionization state depends on the equation

$$\ell n \frac{I'\lambda'^3 g'f'}{I\lambda'^3 gf} = \frac{E' - E}{kT} \qquad (9)$$

it is obvious that a maximum spread in excitation energy between the two lines is desirable to achieve maximum accuracy for the method, since at $E' - E \approx kT$ the errors in the oscillator strengths become important. Since these are typically 30 per cent, a similar temperature error can be expected. Unfortunately, for an air (or nitrogen) plasma at high temperature, the level structure of the atoms limits the choice to lines having excitation energies which differ by only 3 - 6 eV. Since the maximum temperature being considered corresponds to ~ 2 eV, it can be seen that the error in the oscillator strengths will severely limit the accuracy of the technique. The lines listed in Table 2 represent the best energy spreads available consistent with the other criteria.

Table 2

Lines Suitable for Intensity Ratio Temperature Measurements

Species	Wavelength Å	Upper State Term	E_U eV	E_L eV	Effective Principal Quantum Number (n*)	Oscillator Strength (f_{LU})
NI						
	8686.1	$3p^4D^0$	11.70	10.28	2.21	0.242
	8683.4	$3p^4D^0$	11.71	10.29	2.21	0.324
	6008.5	$4d^2P$	13.61	11.55	3.94	0.039
	8567.7	$3p^2P^0$	12.07	10.63	2.37	0.118
	5747.4	$7s^4P$	14.09	11.94	5.84	0.00117
	5752.6	$5d^4P$	13.94	11.79	4.92	0.00185
NII						
	5351.2	$3d^5P$	30.15	27.84	-	0.120
	6888.7	$3d^5P$	30.15	28.36	-	0.282
	4677.9	$4f'^1D$	26.11	23.47	4.01	1.013
	4530.4	$4f'^1G$	26.10	23.36	4.00	0.909
	3006.9	$4s'^1P^0$	24.43	20.32	3.28	0.073
	5679.6	$3p^3D$	20.58	18.40	2.48	0.357
	5676.0	$3p^3D$	20.56	18.38	2.46	0.424
OI						
	7772.0	3^5P	10.69	9.11	2.18	0.432
	9266.0	3^5D^0	12.03	10.69	2.98	0.685
	7952.2	$3p'^3F$	14.04	12.49	-	0.435
	5404.9	$5d'^3G$	16.32	14.04	-	0.0129
OII						
	4649.1	$3p^4D^0$	25.55	22.90	2.40	0.353
ArI						
	8014.8	$4p^3$	13.04	11.50	2.27	0.076
	4259.4	5p10	14.67	11.78	3.15	
ArII						
	4420.9	$4p^4P^0$	19.18	16.39	2.56	0.00521
	4013.9	$4p^4D^0$	19.41	16.34	2.59	0.00869
	3249.8	$4d^4P$	23.02	19.22	3.48	0.168
	3559.5	$4d^2F$	23.06	19.60	3.50	0.203
	3350.9	$4d'^2F$	24.72	21.04	4.43	0.162
	3026.8	$4d'^2S$	25.34	21.26	5.01	0.0801

This difficulty is further shown in Fig. 9, which is a plot of the intensity ratios of several of the lines as a function of temperature. Since the energy spread for the oxygen atom lines is greatest, the ratio of these lines shows the greatest change with temperature. Also shown in Fig. 9 is the intensity ratio of NII 5679.6/NI 8683.4 x N_e. This ratio shows the greatest sensitivity to temperature, since the difference in excitation energy between these lines is 23.41 eV. The ratio of intensities of lines from subsequent ionization states is related to the temperature by

$$\frac{I'}{I} = \frac{1.17 \times 10^{22}}{N_e} \left(\frac{T}{18,000}\right)^{3/2} \frac{f'g'\lambda^3}{fg\lambda'^3} \exp\left(-\frac{E' + E_\infty - E - \Delta E_\infty}{kT}\right) \quad (10)$$

where E_∞ is the ionization energy and ΔE_∞ is the lowering of the ionization energy. Determination of temperature by this technique requires the measurement of two intensities and the electron density. The electron density can be measured by measuring the Stark width of NII 3006 Å. The equilibrium calculations agree with Eq. (10) to better than 10 per cent. The method is usable as long as the Saha equation is rigorously obeyed.

Each of the curves in Fig. 9 is marked with several arrows with a number beside each. These numbers are ρ/ρ_0 values. The arrow locations for each ρ/ρ_0 denote the temperatures below which these lines cannot be used because of insufficient intensity. Thus, for OI 7772.2/OI 5404.9, the lower limit at $\rho/\rho_0 = 10$ is about 6400°K, while at $\rho/\rho_0 = 10^{-4}$ the cutoff is 9300°K. These values were arrived at by assuming that below intensities of 0.1 $\mu W/cm^3$ sr, quantitative measurements could not be made. This figure was arrived at through absolute intensity measurements reported in the literature.[7] However, it must be considered only approximate since optical systems vary greatly. The lines discussed here, although representative of the most favorable circumstances, are not the only ones available for use. Many other lines of each atom or ion are available. Those given here are illustrative of the general situation which obtains in this plasma.

Several conditions must be met if line intensity ratios or line-to-continuum intensity ratios are to be used for gas temperature measurements. The most stringent condition is that the electron and gas temperatures must be equal. This can only be achieved under controlled experimental conditions such as in arcs at or near atmospheric pressure with low electric fields or in shocks under certain conditions. Another is that the free electrons and the excited states being studied must be in equilibrium. This will generally be true for states of high principal quantum number (n) at high electron densities, but as n and N_e decrease the rates of population and depopulation for the excited states become unequal and the relative line intensities no longer give the electron temperature. For hydrogenic atoms and ions, the lowest electron density for which equilibrium will be found is given by Griem[4] (Eq. 6-55) as

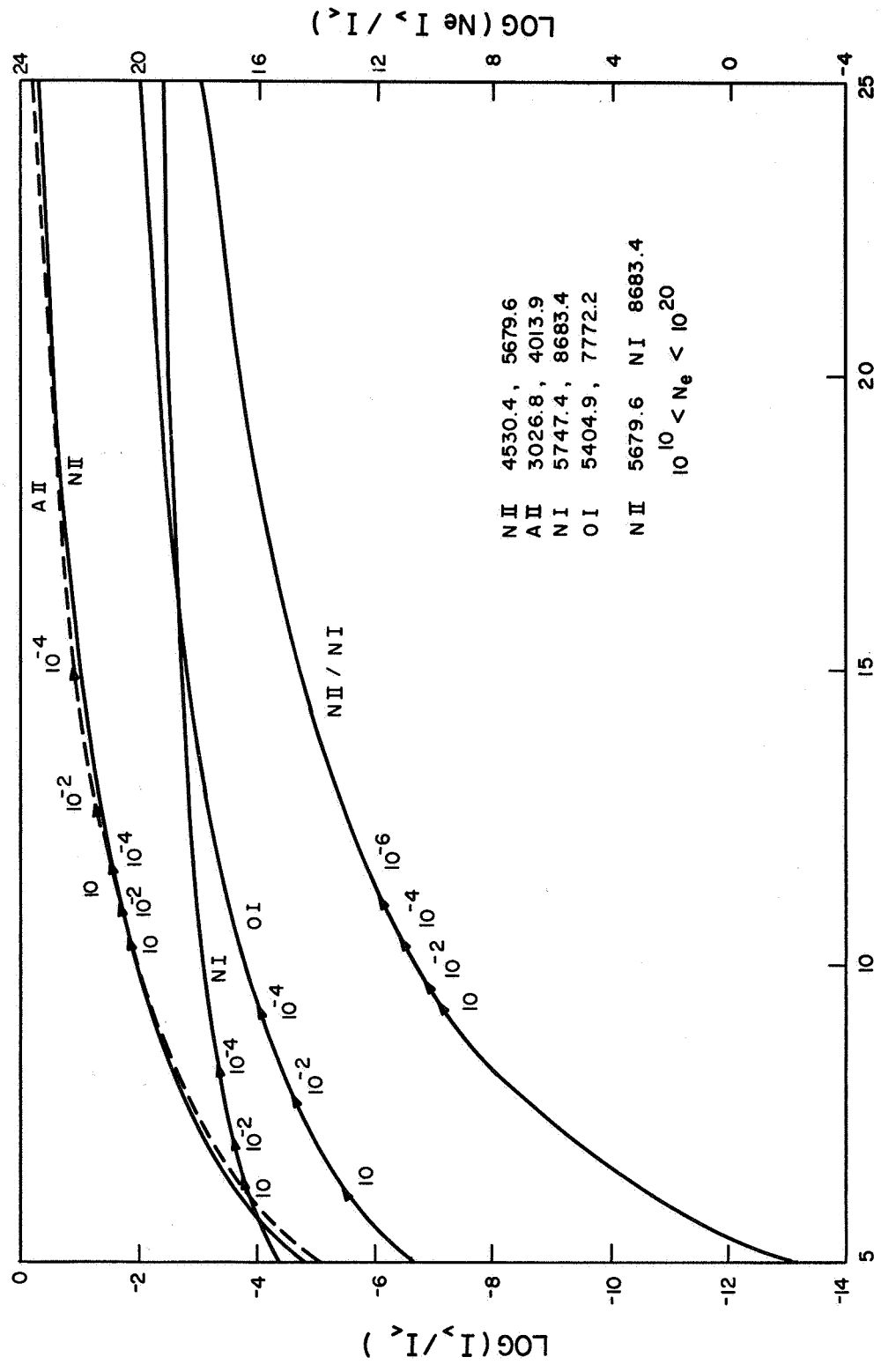

Figure 9 Intensity ratios of lines for several species as a function of temperature. Arrows on curves indicate minimum ρ/ρ_o values for which the line pair can be used at the indicated temperature. The right hand axis applies only to the NII/NI curve.

$$N_e \geq 7 \times 10^{18} \frac{z^7}{n^{17/2}} \left(\frac{kT}{z^2 E_H} \right)^{1/2} \qquad (11)$$

where z is the number of effective charges, E_H is the ionization energy of hydrogen, and n is the principal quantum number (hydrogenic). The effective hydrogenic quantum numbers for the states listed in Table 1 show a minimum value of 2.2 . For this state to be in equilibrium with all states above it and with the free electrons, the electron density (at 2 eV) must be $\geq 5 \times 10^{16}$. For higher lying states, say $n^* = 3$, an electron density of only 2×10^{14} would be required at this temperature. These figures are strictly valid only for hydrogenic atoms, and the atoms of an air plasma do not fulfill this requirement. Detailed calculations have recently been carried out by Kulander[8], who indicates that at 20,000°K an electron density of $\sim 10^{18}/cm^3$ would be required for complete equilibrium between the $3P^4D^0$ level of nitrogen and the free electrons. However, Kulander's assumption that the plasma is optically thin at all frequencies does not appear to be justified. Self-absorption of resonance radiation will tend to keep the lower states in equilibrium and decrease the density limit at which relative excited-state populations will correspond to the electron temperature. The importance of this phenomenon has recently been shown (for cesium) by Norcross and Stone.[9] Thus, the lower density given by the hydrogenic calculations is probably a better approximation than the more rigorous but incomplete work of Kulander. It is obvious that considerably more work is required in such calculations for air constituents before pricise predictions can be made.

Line-to-Continuum Intensities

The fundamental problems which are encountered in using line intensity ratios for temperature measurement are also found when line-to-continuum intensity ratios are used. Griem[4] (p. 279) has stated that the method is restricted to pure gases, mainly hydrogen and helium. Recently, however, Morris et al.[10] have experimentally measured the temperature dependence of the continuum radiation of oxygen and nitrogen at 4348 Å and 4955 Å , respectively, over the temperature range from 9000 to 14,000°K . An arc jet was used for these observations. They measured temperatures by measuring absolute intensities of the NI 4935 Å and OI 4368 Å lines. They found that these lines were optically thin and local thermodynamic equilibrium prevailed at all but the lowest temperatures. Application of their results in a program comparing various methods of temperature measurement should prove interesting. More work appears to be necessary before the method is of general applicability in an air plasma. The method covers the same temperature region as the ion/atom line intensity ratios discussed previously. Since theoretical interpretation is much more difficult, it offers no advantage over the line intensity method.

Doppler Broadening

Of the methods of temperature measurement considered here, this is the only one which measures the gas temperature directly. It appears then that this method offers the most promise in the region in which it can be used. The task which has been undertaken is the definition of the range of utility,

considering such things as competing broadening mechanisms, useful intensities, and instrumental bandpass requirements. For the conditions encountered in the temperature and density range of primary interest here, the only important competing broadening mechanism which will be encountered is Stark broadening due to electrons. Ion broadening is generally negligible. Thus, the upper limit of Doppler temperature measurements will be determined by the electron density at which Stark broadening dominates the profile. The lower limit will be determined by the intensity at which the line becomes too weak for quantitative intensity measurements.

The cutoff value chosen for the intensity ratio measurements (10^{-7} W/cm^3-sr) was also used here.

To calculate Doppler widths for all of the lines, the equation

$$\frac{w_D}{\lambda} = \left(\frac{2kT \ln 2}{Mc^2}\right)^{1/2} \tag{12}$$

was plotted for each constituent of importance. In this equation w_D is the Doppler (half-half) width, λ the wavelength at the line center, and M is the mass of the atom. The plots of w_D/λ vs. T are shown in Fig.10 for the five monatomic constituents which make up an air plasma. Stark broadening calculations were made using the parameters given by Griem[4] The (half) half-width for Stark broadened lines is given by

$$w_S \approx [1 + 1.75\,\alpha\,(1 - 0.75\,r)]w \tag{13}$$

where

$$r = \frac{\text{mean interparticle distance}}{\text{Debye distance}} = \left(\frac{e^2}{4\pi\epsilon_0 kT}\right)^{1/2} N_e^{1/6}$$

This quantity (r) is negligible for our conditions. Values of w and α, the ion broadening parameter, are given by Griem for many lines of interest to us over the temperature range from 2500 to 80,000°K . For most of these lines α is also negligible and we can conclude that $w_S \approx w$, i.e., the Stark halfwidth is determined solely by electron effects. This simplifies the calculation considerably, since w scales directly with the electron density. Qualitative results of these calculations are shown in Fig. 11 for the N I line at 4254.70 Å. This graph shows that Doppler broadening dominates the line shape for $N_e \leq 10^{15}$/cm^3 . Above this value, Stark broadening is the dominant factor. Figure 12 indicates the electron density range which can be expected for the plasma which we have considered. It is obvious that in the high density case, Doppler line widths cannot be used to measure gas temperature except at very low temperatures. In the low density case, however, the electron density never exceeds 1.06 x 10^{14}/cm^3 and this technique is useful throughout the entire temperature range. The insensitive behavior of the Doppler width with temperature as shown in Fig. 11 is also of interest. The half width only varies from 0.029 Å at 5000°K to 0.075 Å at 20,000°K . For this line, an instrument having a bandpass of at least 0.003 Å would be required in order that no instrument corrections need be made.

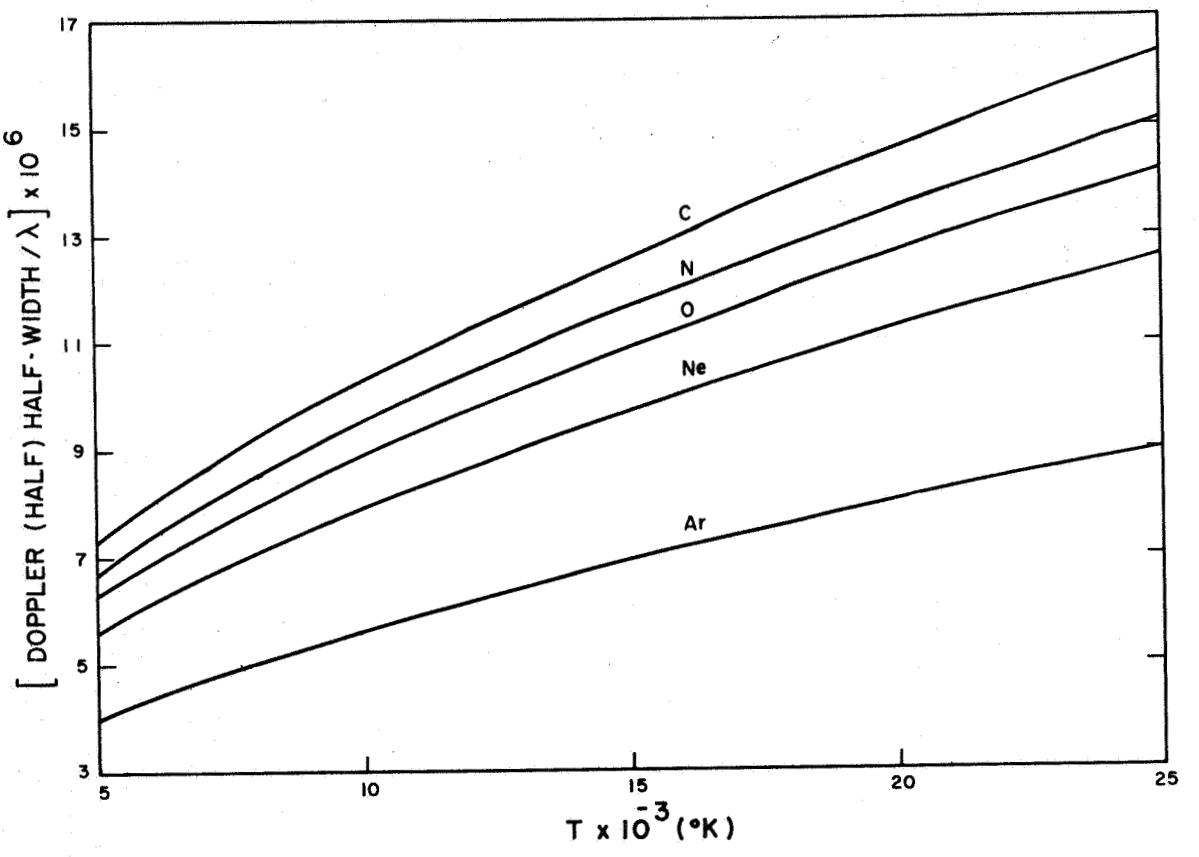

Figure 10 Curves of w_D/λ vs gas temperature for five monatomic constituents of an air plasma.

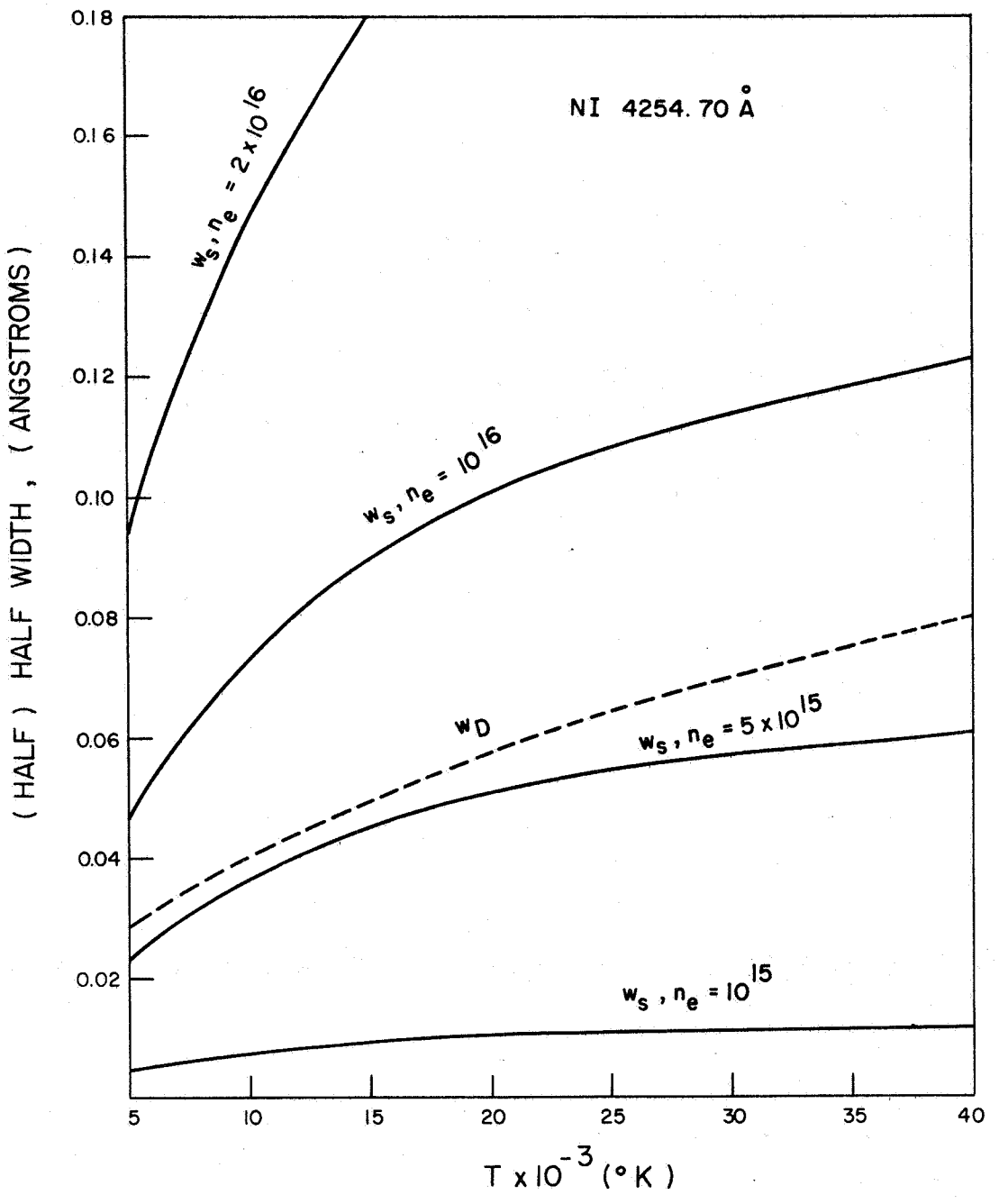

Figure 11 (Half) half widths for Doppler and Stark broadening of NI 4254.70 Å as a function of temperature.

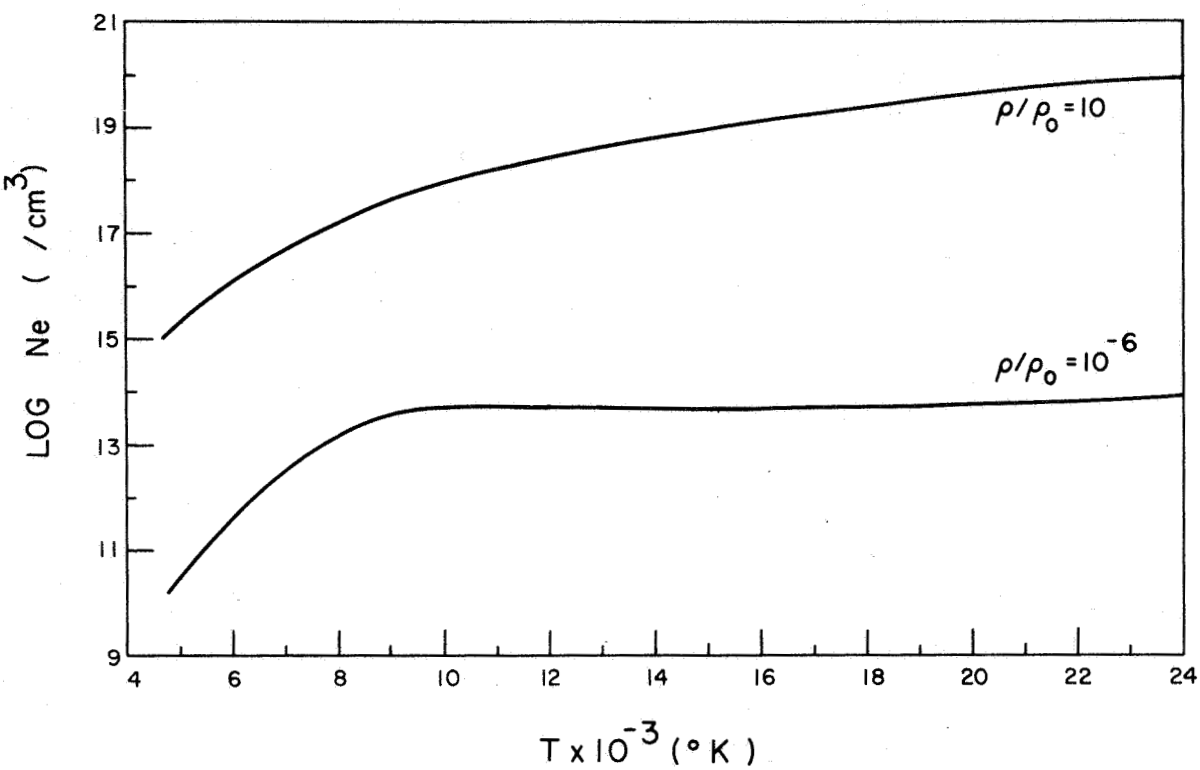

Figure 12 Electron density of hot equilibrium air at high and low particle density as a function of temperature.

In order to assess the exact error due to competing broadening mechanisms, Voight profiles were constructed for several lines. A computer program was written which allows the construction of a line profile for any line broadened by two mechanisms - one of which has a Gaussian profile (Doppler) and the other a dispersion profile (Stark). This method uses the tabulation of Voight functions given by Van de Holst and Reesinck.[11] Lines of given Gaussian widths and dispersion widths can then be folded together to give resultant profiles. The resultant deviation of the half-width from the pure Gaussian half-width will give a temperature with an error twice that of the half-width error. Illustrations of this are given in Figs. 13, 14, 15, and 16. Figure 13 gives plots of the (half) half-widths of the nitrogen line at 8680.2 Å for Doppler broadening and for Stark broadening at three values of electron density. Figures 14, 15 and 16 are the resultant profiles of this line at 10,000°K. Figure 15 represents the situation at $N_e = 1.35 \times 10^{15}/cm^3$, the point where $w_D/w_S = 13.2$. Here the full Doppler half-width is 0.166 Å and the full Stark half-width is 0.0126 Å. The resultant profile given by the solid line has a nearly Gaussian shape and a half-width of 0.172 Å. This leads to an error of 3.6 percent in the width and a corresponding error of 7.2 percent in the temperature. As the electron density becomes greater, the error becomes very large. Figure 15 shows the case where the Stark width is 0.0492 Å ($w_D/w_S = 3.42$). Here the resultant profile has a half-width of 0.192 Å, giving a temperature error of 31 percent. The profile is seen to have strong wing intensity, corresponding to a mixture of dispersion and Gaussian profiles. The extreme situation is illustrated in Fig. 16. In this case the Stark width is 0.094 Å ($w_D/w_S = 1.88$). The resultant profile is more nearly pure dispersion and the error in the half-width leads to a temperature error of 64 percent. All of these curves are normalized to unit integrated intensity. This nitrogen atomic line has been used here because it represents the most favorable case for Doppler broadening, monatomic nitrogen being the lightest species found in this plasma.

From this type of consideration, the upper density cutoff for Doppler broadening was taken as the point where the Stark width is about 10 percent of the Doppler width. The result of these considerations is shown in Fig. 17. These are curves of equilibrium electron density vs. gas temperature for the gas density of interest here. The horizontal lines at the side of the plot indicate the electron density at which the Stark width is 10 percent of the Doppler width for the most intense line of each species indicated. This is generally the line which has the greatest Doppler-to-Stark-width ratio. It can be seen that ion lines have the highest cutoff because of their generally lower Stark widths. However, intensity considerations limit their use over a wide range. This is indicated by the two cases illustrated by the dashed lines. The area inside the lines indicates the region of temperature and electron densities over which Doppler widths of nitrogen (NI 8680.20 Å) and nitrogen ion (NII 5679.6 Å) lines can be used for gas temperature measurements. The horizontal lines are the $w_D \approx 10\ w_S$ cutoff as before, while the curved lines are the intensity cutoff. The nitrogen ion case is the most favorable of all species for reasons of intensity, but can only be used above 10,000°K - 12,000°K at electron densities below $1 \times 10^{16}/cm^3$. The nitrogen atomic line can be used down to 5000°K - 6000°K , but only at electron densities below $2 \times 10^{15}/cm^3$. There is also an upper limit intensity cutoff for the atomic line, indicated by the diagonal line at the right-hand side of the plot.

It is clear from the above discussion that selection of $w_D/w_S \approx 10$ as the cutoff point is somewhat severe, since corrections can be made when Stark broadening is the only competing mechanism. However, this cutoff is realistic when the measurement is to be made automatically because the exact nature of the competing broadening mechanism may not be clear and corrections may be difficult.

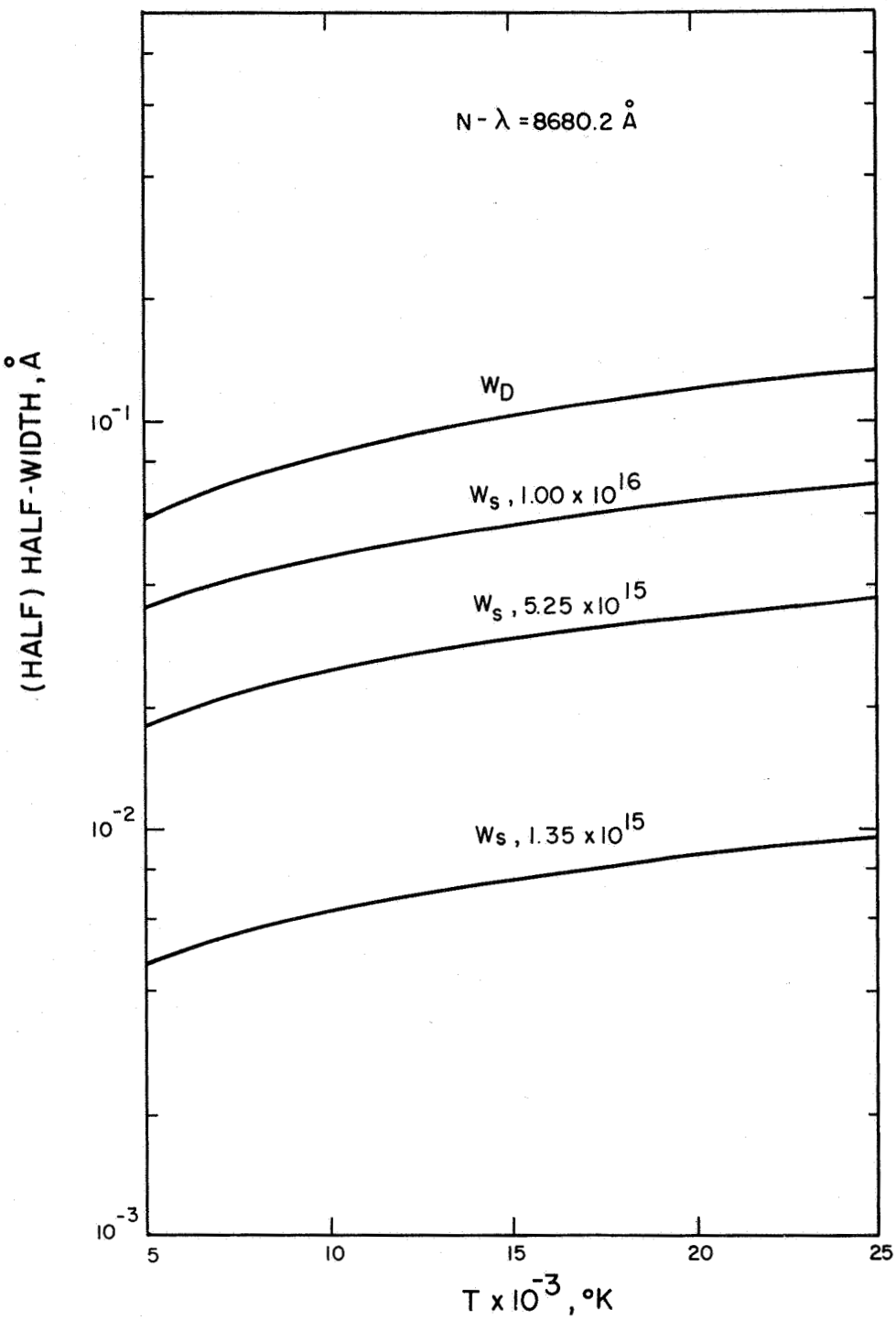

Figure 13 (Half) half widths for Doppler broadening and Stark broadening at three electron densities as a function of temperature for NI 8680.2 Å.

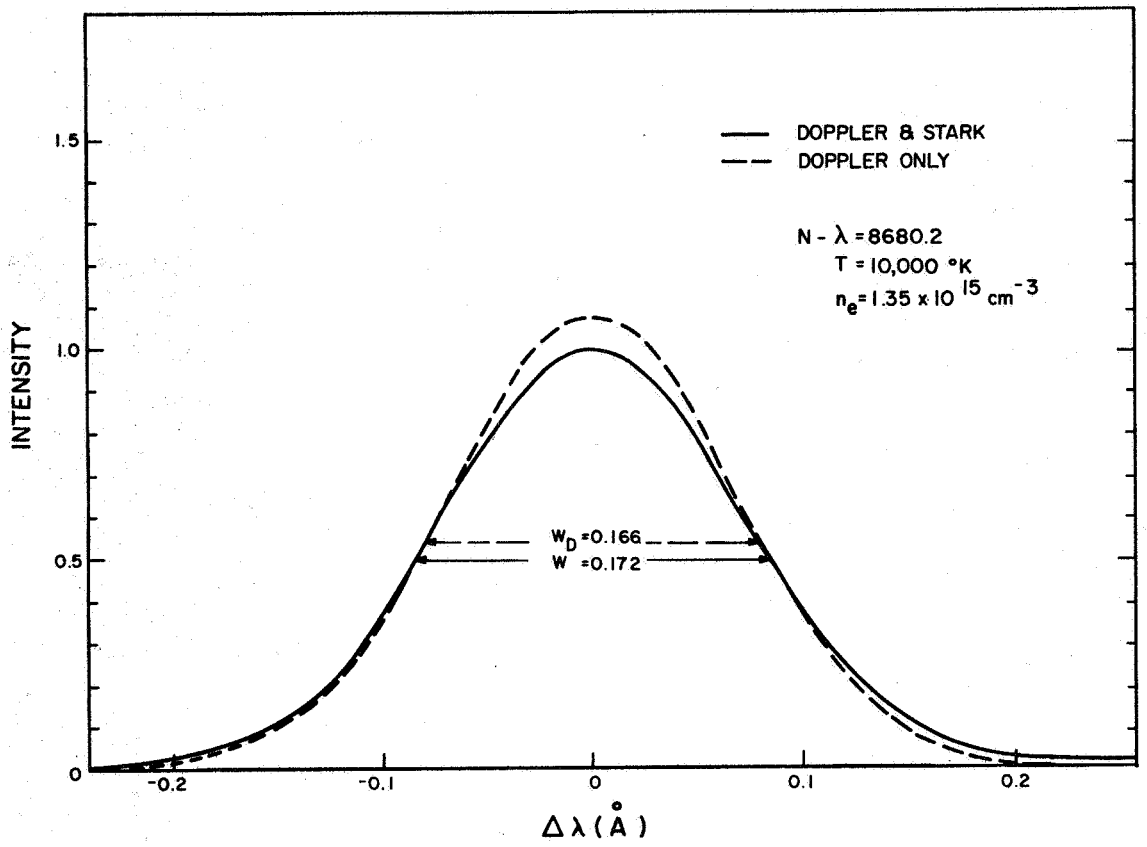

Figure 14 Profiles for NI 8680.2 at 10,000°K. Dashed line is Doppler profile. Solid line is resultant profile when a Stark shape having a width corresponding to an electron density of $1.35 \times 10^{15}/cm^3$ is folded with the Doppler shape.

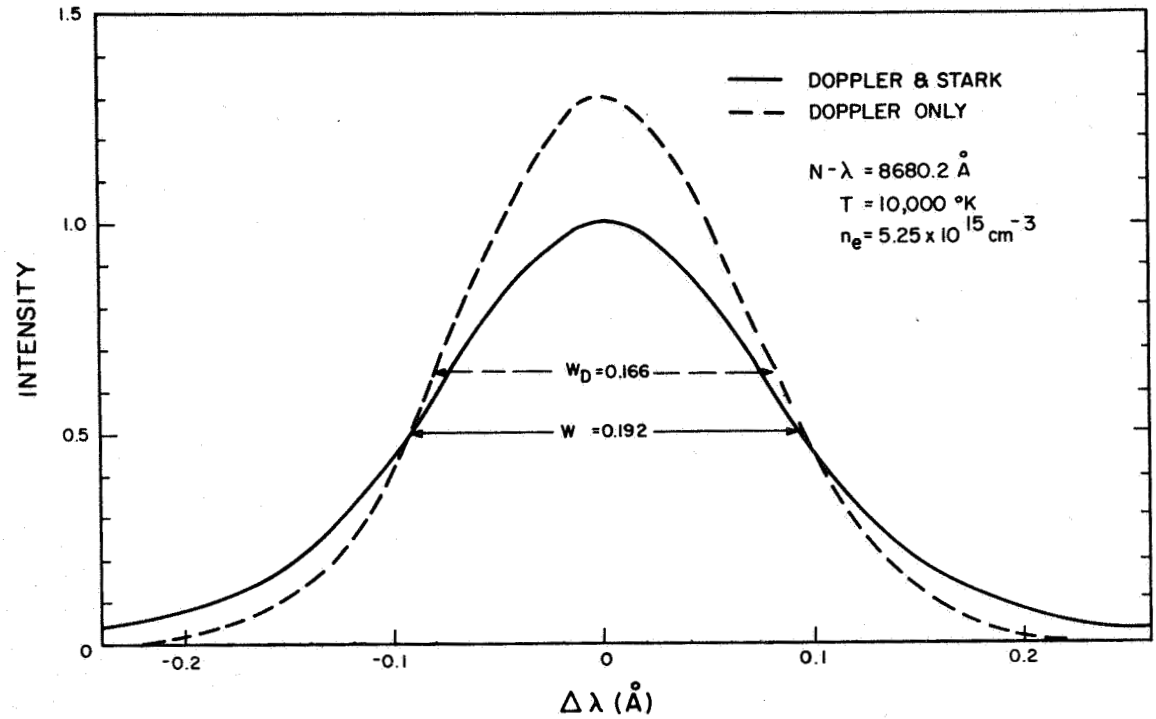

Figure 15 Profiles of NI 8680.2 at 10,000°K. Same as Fig. 14 except Stark width corresponds to $n_e = 5.25 \times 10^{15}/cm^3$.

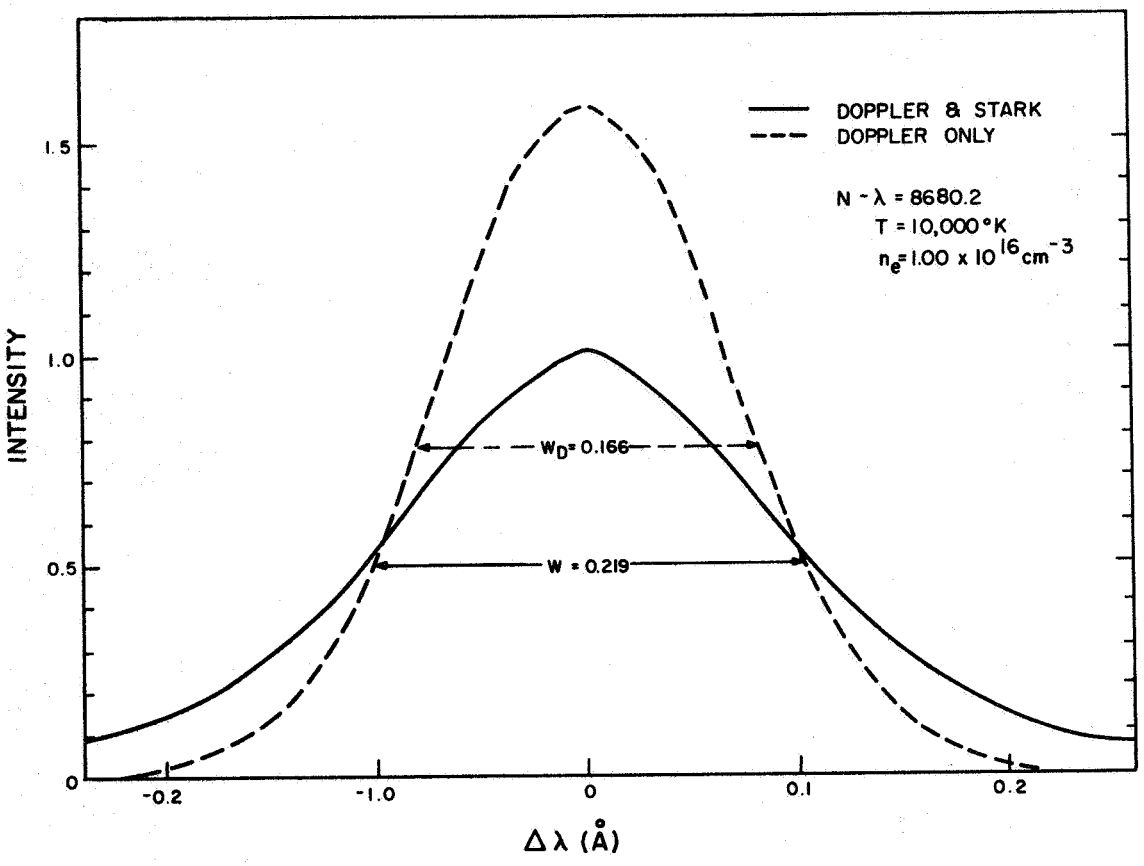

Figure 16 Same as Fig. 14 except $n_e = 1.00 \times 10^{16}/cm^3$.

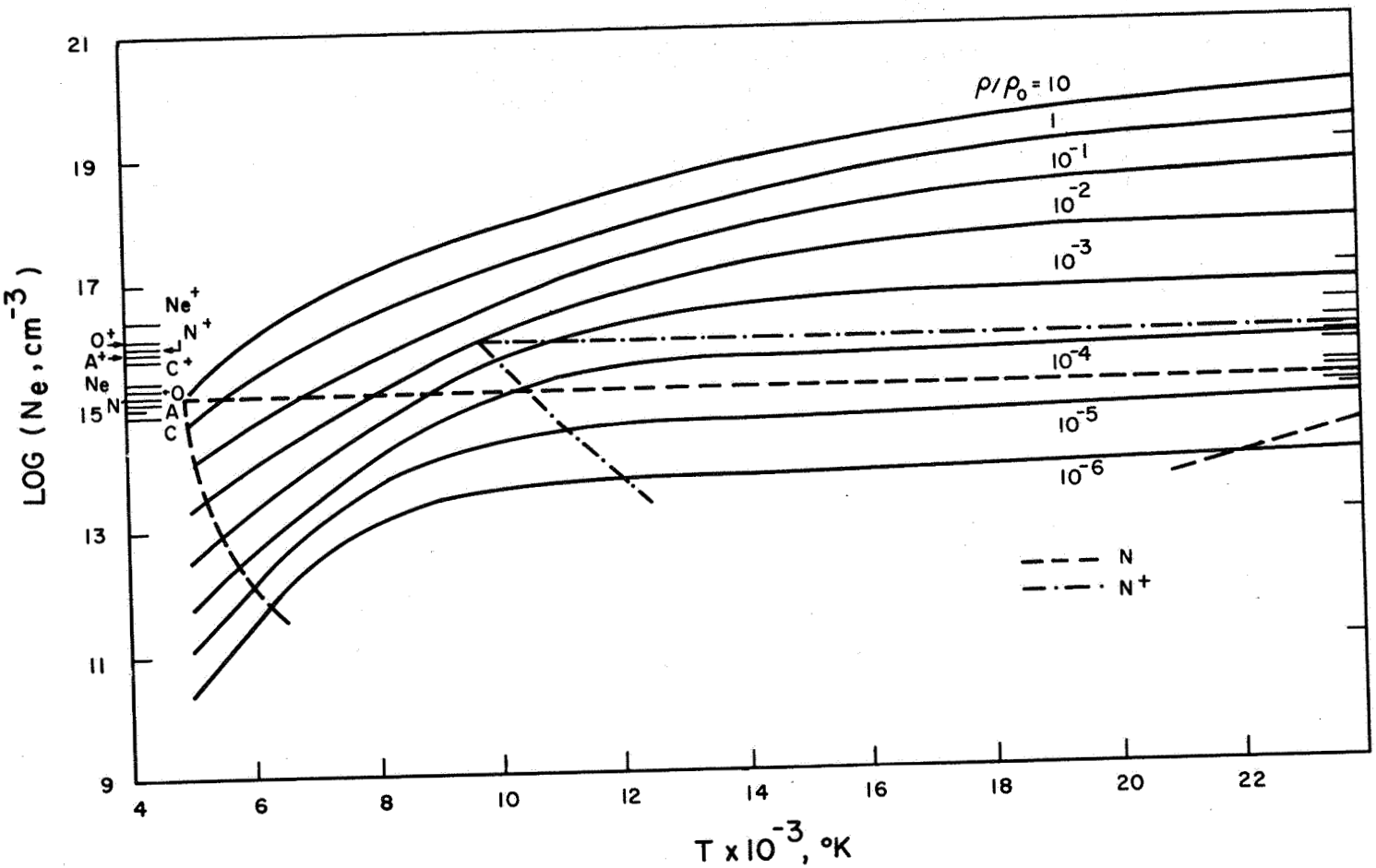

Figure 17 Equilibrium air electron density vs temperature for various ρ/ρ_0 values. Maximum values of electron density for which the best lines of each species can be used are shown on left. For N and N^+ the total range of utility including high and low intensity cutoffs is shown.

Another possible form of broadening is that due to instrumental bandpass. The degree of distortion of the Doppler line profile due to this mechanism can be determined and corrected for in a manner similar to that used when Stark broadening is present. Analysis shows that a slit function of triangular form can be approximated by a Gaussian function to an accuracy of about four percent. Using the Voight method,[11] the Doppler width and the instrument width fold together as

$$\omega_o = 2[w_D = 0.232\ S(\lambda)^2]^{1/2} \qquad (14)$$

where ω_o is the whole half-width of the observed line, w_D is the true Doppler half-half width, and $S(\lambda)$ is the spectral slit width of the instrument (equal to the reciprocal linear dispersion at the exit slit in Å/mm times the physical slit width in mm). This equation is plotted in Fig. 18 for various values of the spectral slit width. These values are typical of modern commercially available spectrometers. For a true Doppler (half-half) width of 0.10 Å, corresponding to a temperature of 14,000°K for NI 8680.2 Å (see Fig. 13), a full spectral slit width of 0.10 Å would result in an observed profile of 0.22 Å (full-half) or 0.11 Å (half-half). This corresponds to an apparent temperature of 17,000°K, giving an error of 21.4 percent. Fortunately because the folding together of the two Gaussian shapes results in another Gaussian shape, this effect can be corrected easily as long as the true width is an appreciable fraction of the instrument width. The slit function can be accurately measured by canning a line width has a width which is small compared to the slit width. Such lines are found in low pressure gas discharges.

Figure 18 is also useful in selecting a spectrometer for use in making line broadening measurements so as to minimize the effect of instrumental broadening. For the nitrogen line mentioned above, the minimum Doppler width to be measured is 0.059 Å at 5000°K. Figure 18 shows that at this width an instrument with a full spectral slit width of 0.05 Å could be used if the corrections described above can be made. If an instrument having a slit width of 0.01 Å were available, no correction would be necessary because the curve for 0.01 Å is coincident with the dashed curve for an infinitely narrow slit at this Doppler width. In this case, Stark broadening corrections could be made accurately within the limits discussed previously.

Measurement of Particle Density with Subsequent Calculation of Temperature

This method of temperature measurement is comprised of some of the other methods discussed in previous sections. For example, the use of line intensity ratios for temperature measurement depends on Saha equilibrium between the two ionization stages. The quantity which is actually measured is the ratio of the ion and atom populations, related by

$$\frac{N_+ N_e}{N_o} = \frac{U_+}{U_o}\ 2\ \frac{(2\pi mkT)^{3/2}}{h^3}\ \exp(-E_\infty/kT) \qquad (15)$$

where U_+ and U_o are the partition functions for the ion and atom, respectively, and the other symbols have their usual meanings. For an air plasma consisting of oxygen, nitrogen, carbon, and rare gases, a

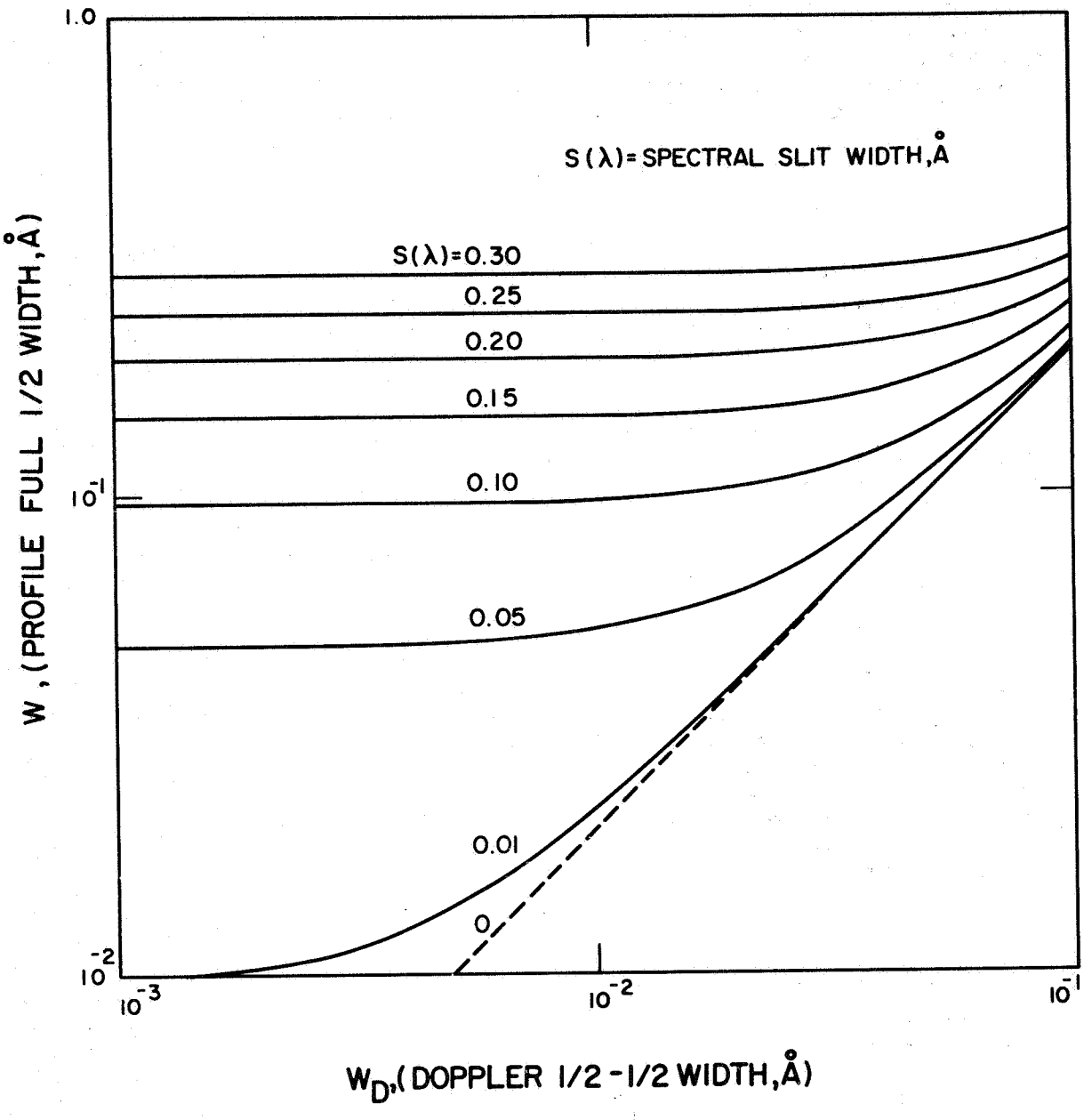

Figure 18 Doppler width vs observed width for various values of spectral slit width assuming a triangular slit function.

number of simultaneous equations must be solved. These are the Saha equations for each constituent, the known relative abundances, and the particle and charge balance equations. When $T_g = T_e$ competing equations similar to Eq. (4) can be solved. In this case it is necessary to measure the electron density and the absolute intensity of one optically thin line of each species. In an air plasma of the composition considered here, the method is cumbersome but can be used with relative ease in one or two component plasmas to check the existence of thermal equilibrium.

The importance of measuring electron densities is clear in establishing the existence of equilibrium. As has been shown recently by McLean and Ramsden[12], optical interferometry can be a valuable tool in determining the electron density in a plasma. Since the refractivity of electrons is negative and proportional to the square of the wavelength at which the observations are made, and the refractivity of the atomic and molecular components is positive and nearly independent of wavelength, simultaneous measurements at two wavelengths can be used to separate the electron contribution from that of the atomic and molecular constituents. The density measured in this fashion can then be used in solving the equations discussed above. This can be a particularly valuable tool in regimes where Stark broadening cannot be used to make these measurements.

Relative Merits of Film and Photomultiplier Techniques

In this section the inherent advantages and disadvantages of both film and photomultiplier techniques are discussed, as are their application to real time and time resolved measurements at the wavelengths of interest in the study. Excellent reviews of this subject are to be found in Sawyer's book[13] and the article by Turner.[14]

Photographic films and plates still are the most widely used detectors for spectroscopy in the visible and ultraviolet portions of the spectrum. However, many factors inherent in the photographic process make this detector undesirable for quantitative measurements, particularly where real-time results are needed. The basic limitation of the photographic process is in the non-linearity of response. This response is given by the well-known H and D curve or the D log E curve. From these curves it is found that a minimum exposure exists, below which no blackening of the photographic plate is observed. Above this point, there is a straight line portion where the density and the log of the exposure are related in an approximately straight-line manner. At high exposures there is a point where an increase in exposure no longer increases the density: this point is called the saturation density. Thus quantitative measurements are limited to the straight-line portion of the curve, severely restricting the dynamic range of the film. This limitation can be obviated to some degree by the use of neutral density filters in the case of high intensity sources, or the use of long exposure times for low density sources in steady state. If the H and D curves were reproducible for each emulsion, the non-linearity and low dynamic range would be relatively minor problems. However, the shape of the curve is strongly sensitive to the type of developer used, the developer temperature and the development time, and even varies from plate to plate within the

same emulsion type due to variations in emulsion thickness, etc. Thus, for maximum accuracy it is important that provision be made for calibration of each plate or film in the wavelength range of interest. This can be accomplished by focusing a suitable source such as a tungsten strip lamp or an iron arc onto the slit of the spectrograph so that the slit is uniformly illuminated at all points. A rotating step sector or step filter is then used to reduce the exposure in known steps. Usually the difference in steps is 1.585. It is then possible to construct a curve of density (which is measured with a microphotometer) versus the relative exposure from the step factor; i.e., the ratio of densitometer readings of two adjacent steps is known to be equivalent to a change in expsoure of 1.585. Several points of varying density are measured and the complete characteristic curve of the emulsion is constructed. The desired lines are then photometered and their intensities are reduced to exposure through use of this curve.

One major source of error in film spectroscopy is the Eberhard effect. This effect manifests itself as an abnormally light area adjacent to a dark area such as a spectral line. The Eberhard effect arises from local depletion of developer in the dark area. It can be minimized by constant agitation of the developing tray, but is never completely eliminated and is often the limiting factor in the accuracy of photographic techniques.

Another major difficulty which is especially important for short duration sources is failure of the reciprocity law. The reciprocity law states that the total energy received by the film is equal to the product of the incident radiant flux and the exposure time. For very long (10^2 to 10^3 seconds) or very short (10^{-5} to 10^{-6} second) exposures this law no longer holds. This problem can be alleviated by using a calibrating source having an exposure time approximately equal to that of the discharge being studied, as has been done by Bronfin et al.[15]

It is obvious from this brief discussion that in processing films extreme care must be taken to obtain quantitative intensity information. Because of this, the time required to obtain quantitative data is long compared to that required when photomultiplier detectors are employed. One to two hours must be considered a minimum time for the processing, densitometry, and data reduction required for spectroscopic temperature measurements by any technique. Thus, real time measurements using films are not feasible. Even if the processing time can be eliminated by use of Polaroid type films, calibration and data reduction still require considerable time. Films are, however, unexcelled in qualitative applications. Wavelengths can be measured within an accuracy of 0.05 Å or better using a spectrograph of moderate dispersion (11 Å/mm). In addition, all of the spectral features are recorded simultaneously, so that temporal variations in the plasma are averaged equally for all lines, bands, and continua. This, along with the fact that a wide range of the spectrum is covered in a single exposure, make the film spectrograph ideal for survey work. The gross features of the spectrum are observed, lines can be chosen for quantitative intensity measurement and/or line broadening measurement, and unexpected features such as the present of impurities are revealed. In this laboratory a 1.5 meter Wadsworth spectrograph is used for this type of work. This instrument covers the wavelength range from 4200 Å -

9000 Å (first order) and has a reciprocal linear dispersion of 10.8 Å/mm. This makes it ideal for survey work, but because of the difficulties outlined above this instrument is never used for quantitative intensity measurements.

Time resolution for film spectrographs can be accomplished in two ways: either by use of a high speed shutter (such as a Kerr cell) or a streak camera in place of the stationary film. The former technique is presently used in this laboratory. With this device, exposure times as short as 0.5 ns can be obtained. One limitation the Kerr cell shutter has is its inability to operate in the ultraviolet portion of the spectrum, caused by the high bias voltages required and the low transmission of nitrobenzene (the fluid used in the cell) in the ultraviolet region. Another limitation is the relatively low rejection ratio; i.e., the open-closed transmission ratio. This ratio is typically 1000 and can lead to erroneous results for extremely bright sources unless another shutter is used to reject most of the unwanted light. The theory of the Kerr cell shutter is well known and need not be discussed here.[16] Streak cameras have the advantage of giving the time dependent behavior of the spectrum and can achieve time resolutions of 0.5 μs. These devices have been used successfully by many laboratories in shock tube spectroscopy, but largely for qualitative and not quantitative measurements.

The photomultiplier tube is a flux sensitive device, and when short time constant electronics are used a time resolution of 0.01 μs can be easily obtained. The much greater sensitivity of the photomultiplier tube allows us to take advantage of its time resolution capability. Often this cannot be done with film as the detector because of the low light levels associated with exposures of microseconds or less. In the case of steady state plasmas, amplifiers having response times of one or two seconds can be used to average out high frequency fluctuations. In addition, the photomultiplier has the advantage of linear response over almost all of its operating range. This greatly simplifies the task of data reduction since time-consuming response calibrations are not necessary. A single calibration with a standard lamp, with infrequent periodic rechecks, is sufficient in most applications. Since the photomultiplier tube is a transducer which converts radiant energy to an electrical signal, its advantages for real time measurements are obvious. The intensity ratio of two lines can be measured nearly instantaneously and converted to a temperature automatically. Line width measurements can be made using several photomultipliers spaced at known intervals from the line center and Voight profiles constructed by use of a computer. It is clear that any real-time measurement system will ultimately use photomultiplier tubes as detectors. However, an experimental research program devoted to determining the proper lines for use in these measurements will make judicious use of both film and photomultiplier techniques as outlined here.

Experimental Approach

Two experimental devices, the arc jet and the electromagnetic shock tube, are necessary for complete experimental verification of the calculations made in this study. The arc jet is a highly reproducible, cylindrically symmetric source of high temperature lines, bands, and continua .

This device operates at high power levels in air (typically 8 kW) and is capable of producing temperatures of 10-15,000°K over a pressure range from 0.1 - 1 atmosphere. A schematic diagram is shown in Fig. 19. An interesting feature of this type of discharge is the inequality between the gas and electron temperature.

As has been pointed out by Lochte-Holtgreven,[17] there will always be a difference between the electron and the gas temperature because the electrons are gaining energy from the electric field. This difference is given by:

$$\frac{T_e - T_g}{T_e} = \frac{(\lambda eE)^2 M}{\left(\frac{3}{2}kT_e\right)^2 4m}$$

where M and m are the masses of the gas and electron, respectively; λ is the electron mean-free-path, and E is the electric field strength.

The temperature difference is proportional to the square of the electric field strength and the mean-free-path. Since the electric fields can be quite high, a real difference can exist between T_e and T_g even at atmospheric pressure. At lower pressures, where the mean-free-path becomes long, very large differences can exist. Consequently, this instrument should prove valuable in determining the error in equating gas and electron temperatures.

A layout of the electromagnetic T-tube is shown in Fig. 20 along with the required circuitry (except for the charging supply). By creating an auxiliary spark across the switch, the trigger circuit (2) allows the switch (4, 7) to be broken down at any desired voltage less than the breakdown potential of the switch. The energy stored in the capacitor with the induced magnetic fields creates a shock which propagates down the tube (8). The reflected shock is a homogeneous layer of high temperature gas. The T-tube has many of the same characteristics as the conventional diaphragm-type shock tube, but has the advantages of being simpler in construction and easier to operate. It is not possible to calculate the temperature and densities as in diaphragm shock tubes because the shock produced has many of the characteristics of a blast wave rather than a time shock. This is unimportant for this investigation, however. The plasma produced in this device is in equilibrium at low pressures (0.1 - 10 torr) at temperatures up to 20,000°K. This range complements the higher pressure plasma produced by the arc jet and provides a medium for studying the methods of temperature measurement where equality between T_g and T_e can be expected.

Both of these devices are presently under construction, as is the necessary instrumentation for studying the methods of temperature measurement outlined in the previous sections.

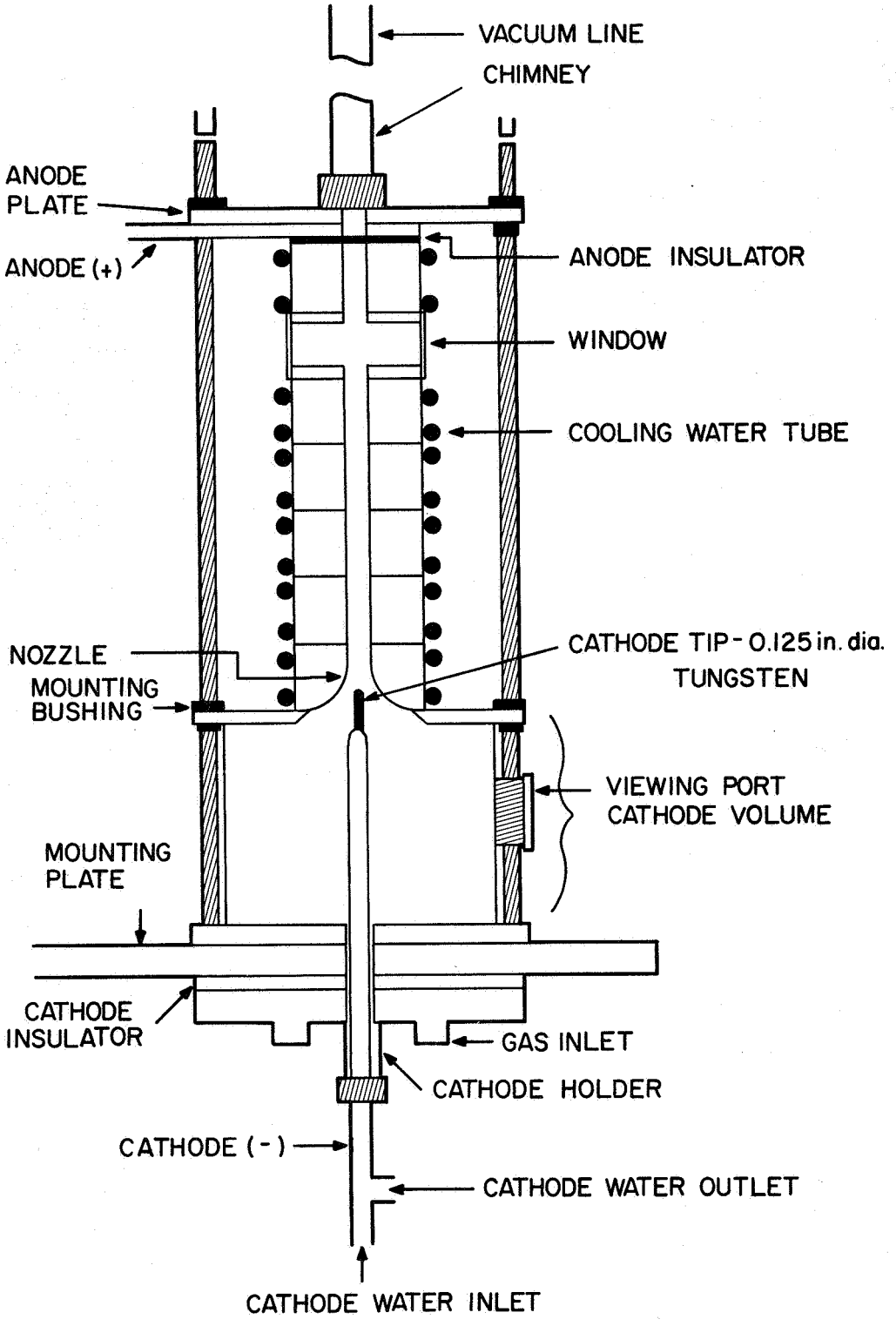

Figure 19 Schematic diagram of wall stabilized arc jet.

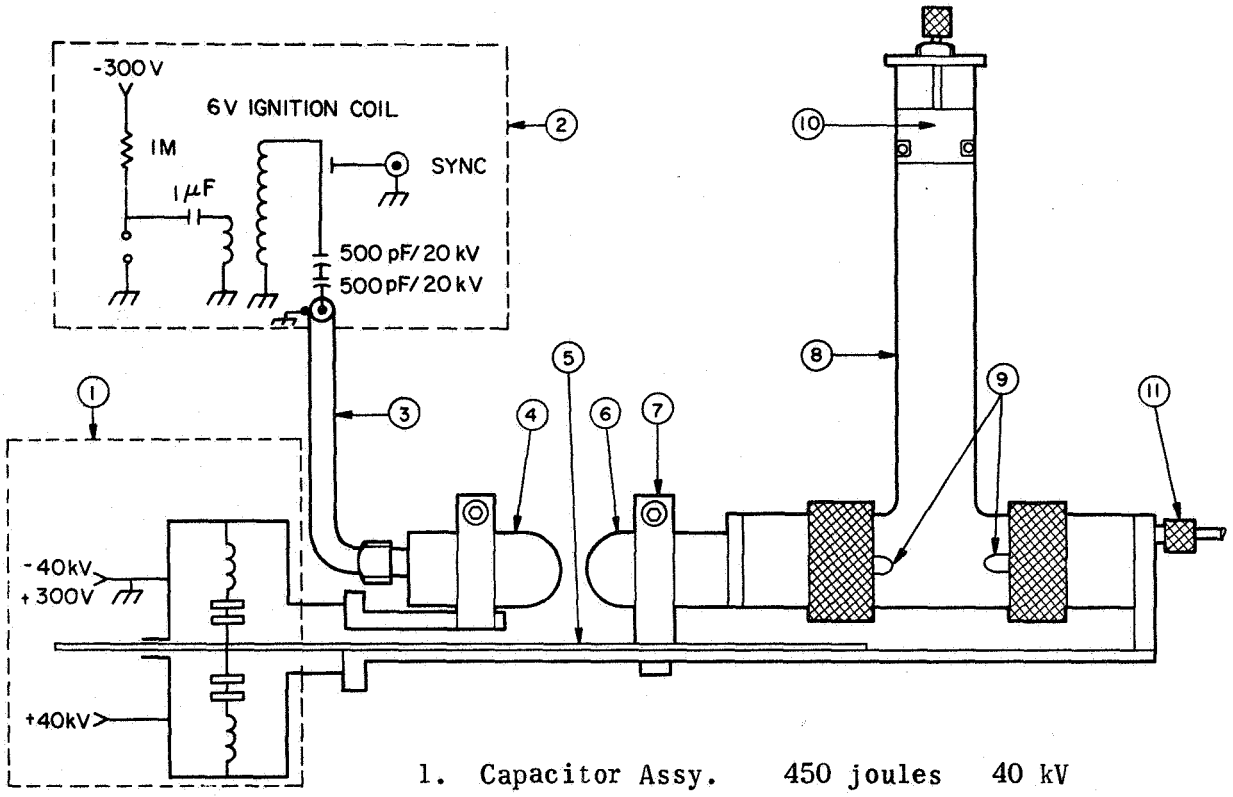

1. Capacitor Assy. 450 joules 40 kV
2. Trigger Assy.
3. Trigger Cable RG 8/v
4. Adjustable Switch Electrode
5. Mylar Insulating Sheet
6. Fixed Switch Electrode
7. Electrode Support
8. Quartz Shock Tube
9. Electrodes
10. Adjustable End Seal
11. Connection to Vacuum & Filling System

Figure 20 Schematic diagram of electromagnetic T-tube and associated circuitry.

CONCLUSIONS

It is clear from Figs. 9 and 17 that no single method of temperature measurement is adequate over the entire range of temperatures and densities considered here. Two methods appear to overlap sufficiently to cover a large portion of the desired range, however. For high pressures, the method which appears most promising is the measurement of line intensity ratios. Between 6000°K and 10,000°K the intensity ratio of the two oxygen I lines shown in Fig. 9 shows the most sensitivity to temperature. This ratio can be used only at ρ/ρ_o values of 10 at the lowest temperatures. At lower pressures nitrogen I lines must be used. Above 10,000°K the ratio of a nitrogen ion line to a nitrogen atom line should be used. This measurement requires a determination of electron density, which can also provide a check on the presence of equilibrium in the system. At high densities this can be accomlished through Stark broadening measurements, as indicated previously. At low densities, where Doppler broadening dominates, another method of electron density measurement (e.g., wavelength interferometry) would be required.

Even in plasmas where equality between the gas and electron temperatures can be assumed, the line-intensity-ratio method fails below electron densities of approximately $10^{15} - 10^{16}/cm^3$ because of the departure from equilibrium between the excited states and the free electrons. It is fortunate that at these lower densities Doppler broadening can be used to measure the gas temperature, as indicated in Fig. 17. Doppler broadening of a nitrogen atom line can be used at low temperatures below an electron density of $2 \times 10^{15}/cm^3$, while above 10-12,000°K the density limit is raised to $1 \times 10^{16}/cm^3$ as the nitrogen ion line becomes available.

These considerations lead to several requirements which any real-time temperature measuring system must possess. Such a system must be capable of measuring a number of different line intensities and correcting for background radiation. The instrument must also have a variable bandpass because high dispersion is required for making line broadening measurements, while relatively low dispersion is necessary for making line intensity measurements. An independent means of measuring electron density, such as a two wavelength interferometer, must be provided in order to determine whether intensity measurements or line broadening measurements are to be made. Photomultipliers would be used as detectors in order to establish a real time capability. Their signals would be fed directly to a computer which would perform the necessary calculations and determine the temperature instantaneously. The same computer could also be used to determine which method of temperature measurement is appropriate to the electron density range being studied.

REFERENCES

1. F. R. Gilmore, Project Rand Research Memorandum RM-1543 (1955).

2. J. Hilsenrath and M. Klein, Arnold Engineering Development Center Report AEDC-TR-65-58 (1965).

3. W. E. Moechel and Kenneth C. Weston, NACA Technical Note #4265 (1958).

4. H. Griem, Plasma Spectroscopy, McGraw-Hill, New York (1964).

5. C. Moore, A Multiplet Table of Astrophysical Interest, NBS Technical Note 36 (1959).

6. D. R. Churchill, B. H. Armstrong, R. R. Johnston, and K. G. Müller, J. Quant. Spectrosc. Rad. Transfer 6, 371 (1966).

7. C. B. Collins and W. W. Robertson, J. Chem. Phys. 40, 2202 (1964).

8. J. L. Kulander, J. Quant. Spectrosc. Rad. Transfer 5, 253 (1965).

9. D. W. Norcross and P. M. Stone, Proceedings of the 26th Annual Conf. on Physical Electronics, Cambridge (1966), p. 96.

10. J. C. Morris, R. V. Krey, and G. R. Bach, J. Quant. Spectrosc. Rad. Transfer 6, 727 (1966).

11. H. C. Van de Holst and J.J.M. Reesinck, Astrophys. J. 106, 121 (1947).

12. E. A. McLean and S. A. Ramsden, Phys. Rev. 140, A1122 (1965).

13. R. A. Sawyer, Experimental Spectroscopy, Dover, New York (1963).

14. E. B. Turner (Ed. R. H. Huddlestone and S. L. Leonard), Plasma Diagnostic Techniques, Academic Press, New York (1965), p. 319.

15. B. R. Bronfin, E. A. McLean, and H. R. Griem, J. Opt. Soc. America 52, 224 (1962).

16. F. G. Dunnington, Phys. Rev. 38, 1506 (1931).

17. W. Lochte-Holtgreven, Reports on Progress in Physics, 21, Physical Society London (1958). p. 312.

ABSTRACT

A theoretical investigation was undertaken to develop a real-time temperature-measurement technique over the temperature range from $5000^{o}K$ - $24{,}000^{o}K$ from 10 times normal density to 10^{-6} times normal density. Two spectroscopic methods were found to cover the range adequately. Above electron densities of 10^{15} - $10^{16}/cm^{3}$ line intensity ratios can be used, and below these densities Doppler line broadening is preferred. Calculations of the atomic and ionic radiation of air over this temperature and density range have been performed, a conceptual real-time temperature-measurement system has been outlined, and recommendations have been made for experimental investigation of this problem.

APPENDIX B

ULTRAHIGH TEMPERATURE MEASURING TECHNIQUES

Quarterly Progress Report No. 5
Contract No. NAS 12-86

SRRC-CR-67-41

ULTRA-HIGH TEMPERATURE MEASURING TECHNIQUES

Quarterly Progress Report No. 5
covering the period
1 May 1967 - 31 July 1967
Contract No. NAS 12-86

Prepared for: NASA/Electronics Research Center
575 Technology Square
Cambridge, Massachusetts

Principal Investigators: Dr. Ronald H. Curry
Dr. Philip M. Stone

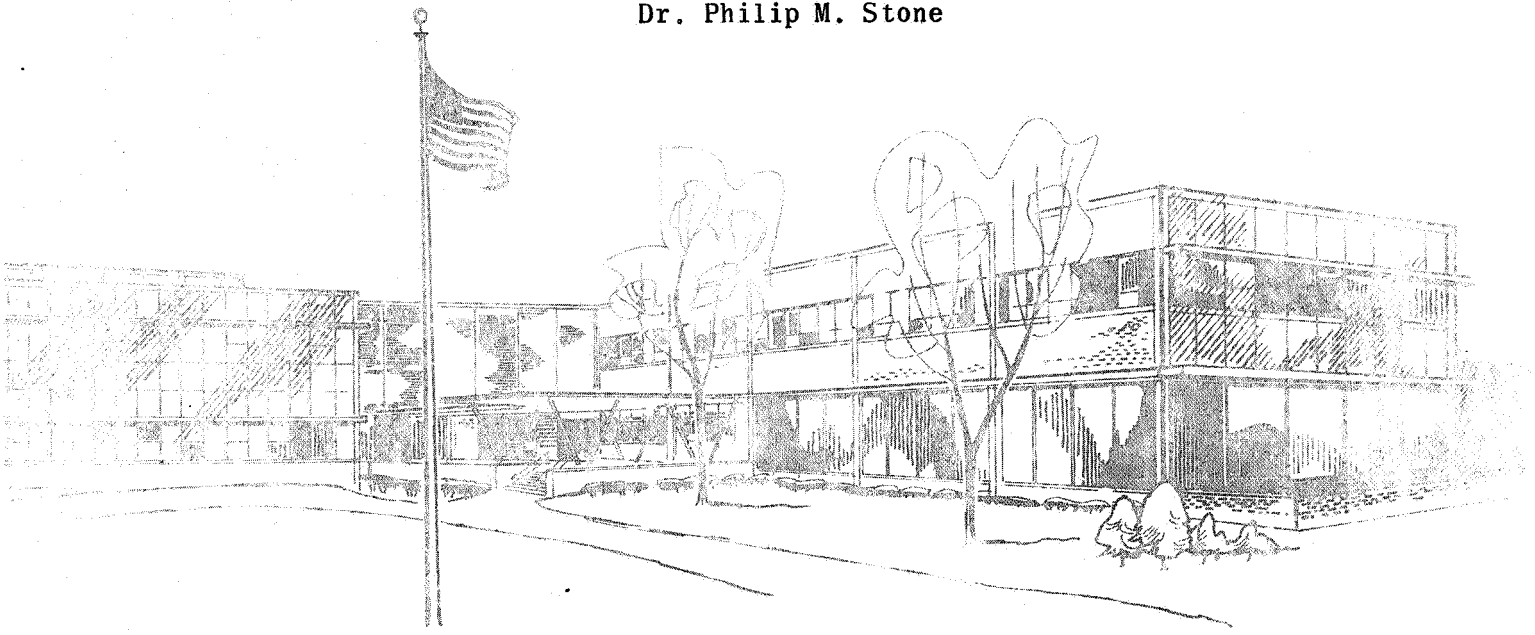

SPERRY RAND RESEARCH CENTER
SUDBURY, MASSACHUSETTS

TABLE OF CONTENTS

LIST OF ILLUSTRATIONS

I. INTRODUCTION

The purpose of this investigation is to conduct experimental and theoretical investigations into methods of determining the kinetic temperature of an air or nitrogen plasma over a wide range of densities. A wall stabilized arc jet is to be used to generate the plasma to be studied.

In addition to the effort on the high-temperature air plasma, a theoretical investigation of the absorption of radiation from a very hot (up to 50,000^{o}K) source is being conducted. This includes a calculation of the photoabsorption coefficients in the far-ultraviolet region for cesium-seeded hydrogen plasmas and the evaluation of methods of temperature measurement for such plasmas.

During this quarter further progress has been made toward evaluating the photoabsorption coefficient of the cesium-seeded hydrogen plasma. The equations describing the absorption rates for free-free, free-bound and bound-bound transitions have been prepared for computer solution, and procedures for obtaining the rates have been decided. In addition, the line and continua that are important for absorption in the far ultraviolet (4-25 eV photons) have been determined.

The arc jet is now near final assembly. The ballast resistor has been completed and assembly of the resistor, power supply and arc jet in an operational frame is progressing. The high resolution monochromator has been used to measure actual line shapes in a cesium plasma in preparation for its use in this program.

II. PHOTOABSORPTION COEFFICIENT OF CESIUM-SEEDED HYDROGEN

(i) General

Detailed calculations of the relative and absolute densities of the various species present in a high temperature cesium-seeded hydrogen plasma have been completed. Cesium seed fractions from 10^{-3} to 10^{-1} are considered. These results identify the regions of plasma temperature, pressure, and photon energy over which it will be most practical and useful to consider the contribution of cesium to the total opacity of the plasma.

Initial calculations of the photoabsorption coefficient will be confined to the pressure range of 10^{-1} to 10^{2} atm. The lower limit was chosen arbitrarily, but for pressures much above 10^{2} atm, the lowering of the ionization potential ΔE discussed in Quarterly Progress Report No. 4 becomes so large as to bring into question the validity of the equation for the partition function of cesium.

Figure 1 shows that hydrogen molecules constitute less than 20% of the hydrogen partial pressure at temperatures above 5000^{0}K in the pressure range of interest.[1] Hence error due to the neglect of photoabsorption by the line spectrum of H_2 is minimized by confining the investigation to plasma temperatures above 5000^{0}K. Above $20,000^{0}$K both ground state Cs^{+++} and highly excited Cs^{+} begin to become present in significant amounts. Very little is known about the atomic characteristics of these species, and it was decided to limit concern to plasma temperatures below $20,000^{0}$K.

The objective of this study is to determine the absorption of radiant energy from a very hot ($50,000^{0}$K) source. The emittance of a blackbody at $50,000^{0}$K is maximum at a photon energy of about 12 eV (1000 Å). About 80 percent of the total energy emitted is concentrated in the region 4 to 25 eV (500 Å to 3000 Å).[2] This energy region also encompasses almost all of the interesting photoabsorption regions of the Cs-H plasma and is the energy range that will be investigated.

In summary, the ranges of parameters which will be considered in initial calculations of the photoabsorption coefficient of a high temperature cesium-seeded hydrogen plasma are:

Plasma Pressure:	10^{-1} - 10^{2} atmospheres
Plasma Temperature:	5000 - 20,000^{o}K
Photon Energy:	4 - 25 eV

(ii) Particle Concentrations

Figures 2 through 10 are detailed plots of concentrations of the various species present in the Cs - H plasma. In these plots H_t represents the total concentration of hydrogen monotonic species (H, H^+) and Cs_t represents the total concentration of cesium monotonic species (C, C^+, C^{++}). Molecular hydrogen is present in significant concentrations only at low temperatures. Species such as H_2^+, H^- and Cs^{+++} are not present anywhere in the range of parameters being considered. The variable P is the sum of H_t, Cs_t, and the electron density N_e.

The ratio of H to H_t is plotted in Fig. 2 for the full range of electron density which is present in the cesium-seeded hydrogen plasma for the ranges of temperature, pressure and cesium seed being considered. The degree of ionization of hydrogen is independent of the seeding, as will be discussed below.

Figures 3, 5, 7 and 9 are plots of the electron density obtained from various combinations of cesium seeding, temperature and pressure. They differ slightly from similar plots in Quarterly Progress Report No. 4 because of improvements in energy level data. Figure 2 shows that the degree of ionization of hydrogen is nearly independent of N_e at low temperatures. At high temperatures, on the other hand, the degree of ionization does depend on N_e but N_e is independent of seed fraction (Figs. 3, 5, 7, 9). Hence the lack of any significant variation of the hydrogen ionization with seeding over these temperature and pressure ranges.

The relative concentrations of the cesium species and H_t are plotted in Figs. 4, 6, 8 and 10 for seeding fractions of 10^{-1}, 10^{-2} and 10^{-3}. The concentration of Cs^+ is seen to be a significant fraction of

Cs_t at all temperatures and pressures. The Cs concentration is significant at low temperatures but not high, and the reverse is true for Cs^{++}.

It should be noted that the relative concentration of any cesium species and H for particular conditions of temperature, pressure and seeding is easily obtained by using Figs. 3 through 10 in conjunction with Fig. 2.

Figure 11 summarizes the information in Figs. 2 through 10 in a simple fashion. The temperature and pressure region of concern is divided into three regions, in which the listed cesium species constitute more than one percent of the total cesium concentration for seedings of 10^{-3} to 10^{-1}. This plot gives a rough idea of the species expected to be the dominant contributors to photoabsorption. More detailed consideration of the relative populations of the bound levels of the individual species is contained in the next section.

(iii) Photoabsorption Coefficient

The opacity calculation must include bound-bound transitions (line absorption), bound-free transitions (photoionization), and free-free transitions (inverse Bremsstrahlung). As previously mentioned, the photoabsorption coefficient will be calculated over the far ultraviolet region ($4\ eV \leq h\nu \leq 25\ eV$). This frequency range includes most of the emission from a $50{,}000^{0}K$ blackbody source.

The absorption coefficient, cm^{-1}, can be written

$$K(\nu,T) = \sum_{i,j} \frac{h\nu_{ij}}{4\pi} N_i B_{ij} S_{ij}(\nu) + \sum_{i} N_i \sigma_{ie}(\nu,T) + N_e \sigma_{ee}(\nu,T) \qquad (1)$$

where the three terms represent bound-bound, bound-free and free-free absorption, respectively. B_{ij} is the Einstein absorption coefficient

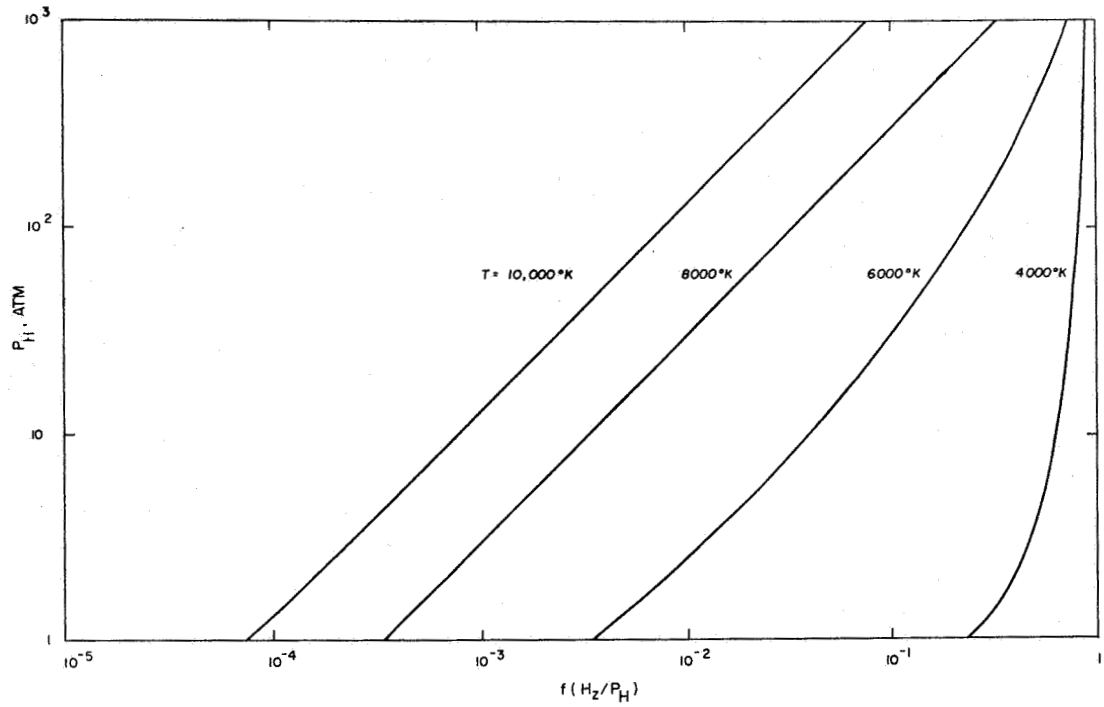

FIG. 1 Ratio of the partial pressure of H_2 to the total hydrogen pressure ($H_2 + H + H^+$) for various temperatures.

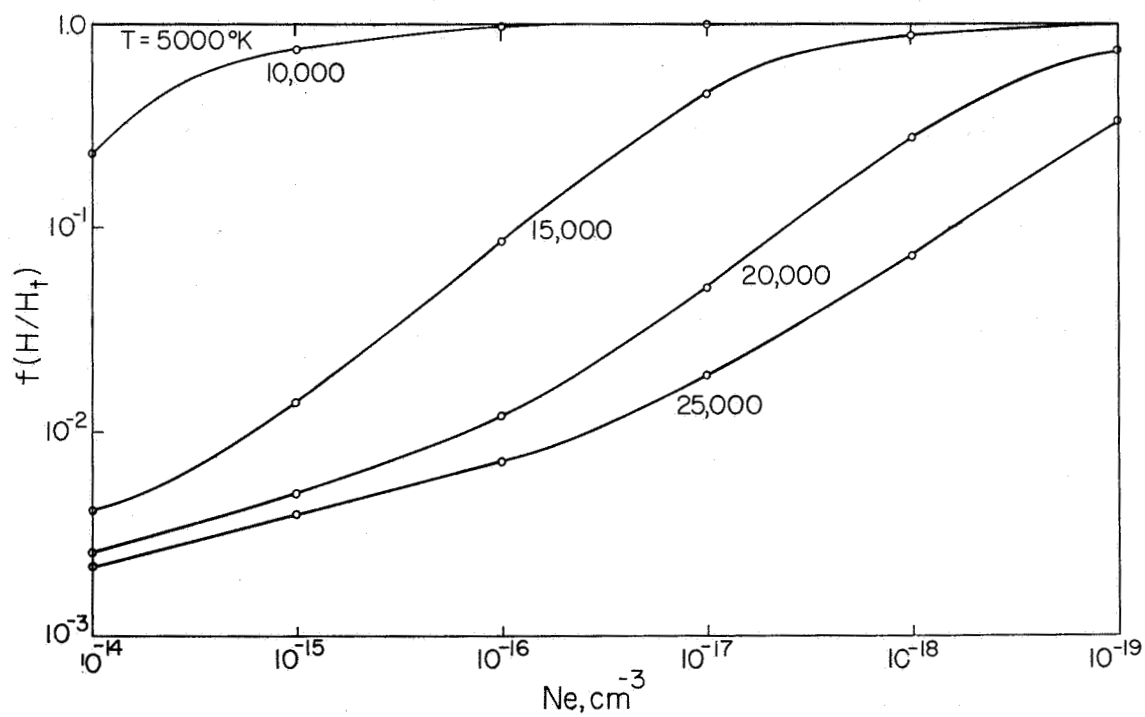

FIG. 2 The degree of ionization of hydrogen ($H/H + H^+$) vs electron density. This quantity is essentially independent of cesium seed fraction as discussed in the text.

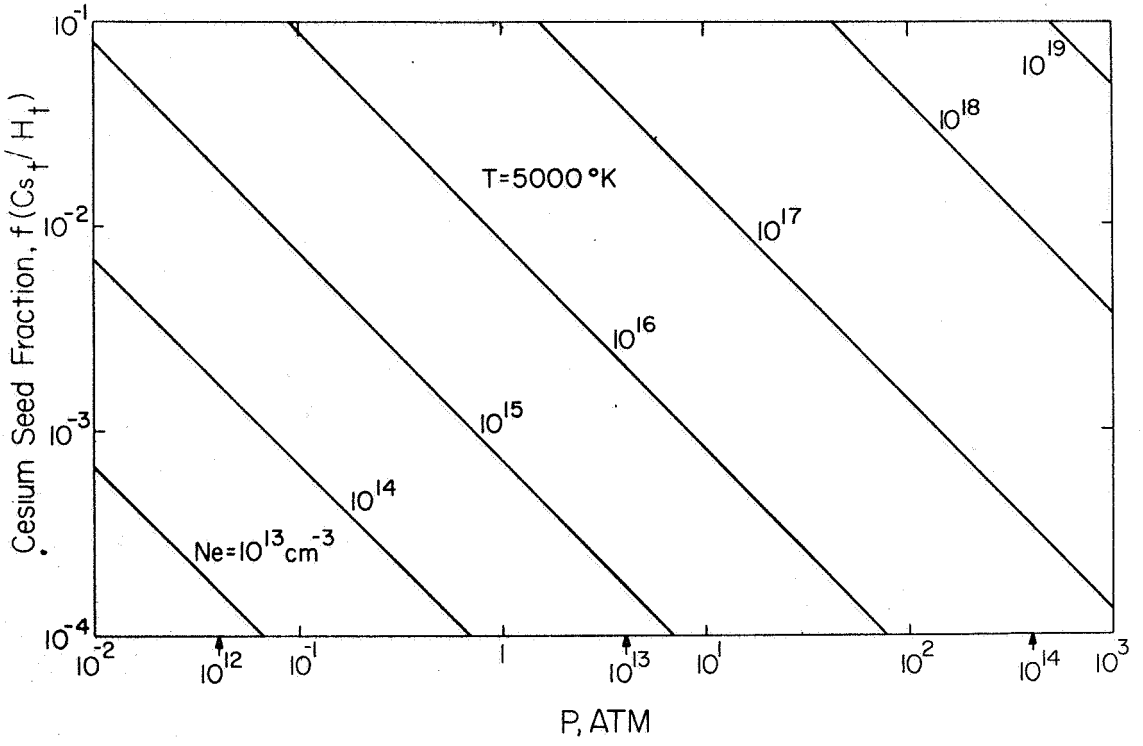

FIG. 3 Electron density in a cesium-hydrogen plasma at 5000°K as a function of cesium seeding. The ratio of Cs particles (atoms plus ions) to hydrogen particles (atoms plus ions) is plotted vs the total pressure of monatomic species and electrons. The electron density in a pure hydrogen plasma is indicated by the arrows. The additional partial pressures of H_2 is plotted in Fig. 1.

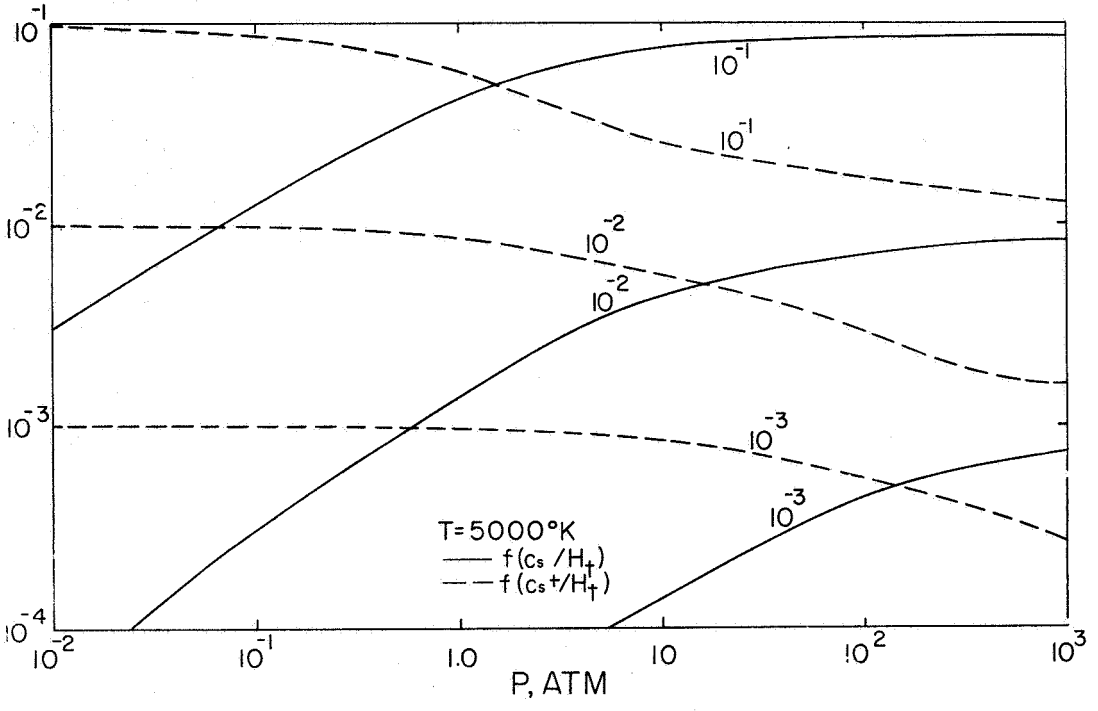

FIG. 4 The ratio of Cs atoms and of Cs^+ ions to hydrogen particles (atoms and ions) vs total pressure at 5000°K for seed fractions $f(Cs_t/H_t)$ of 10^{-1}, 10^{-2} and 10^{-3}.

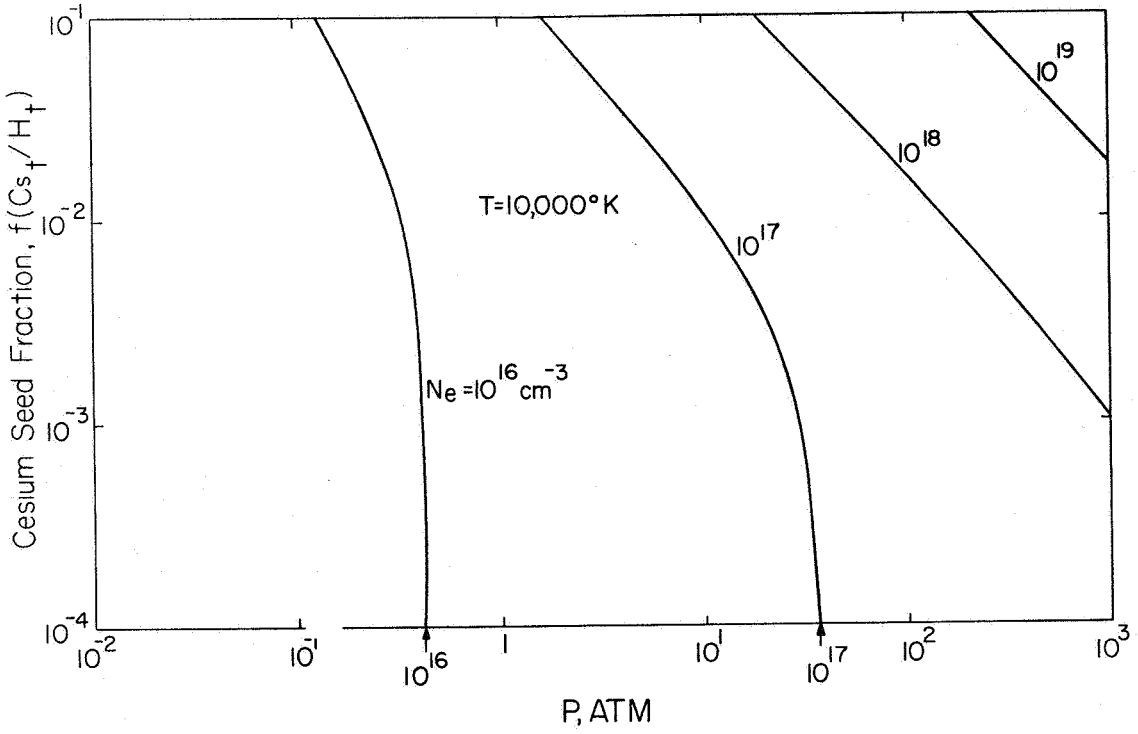

FIG. 5 Electron density in a cesium-hydrogen plasma at 10,000°K as a function of cesium seeding. Nomenclature is the same as Fig. 3.

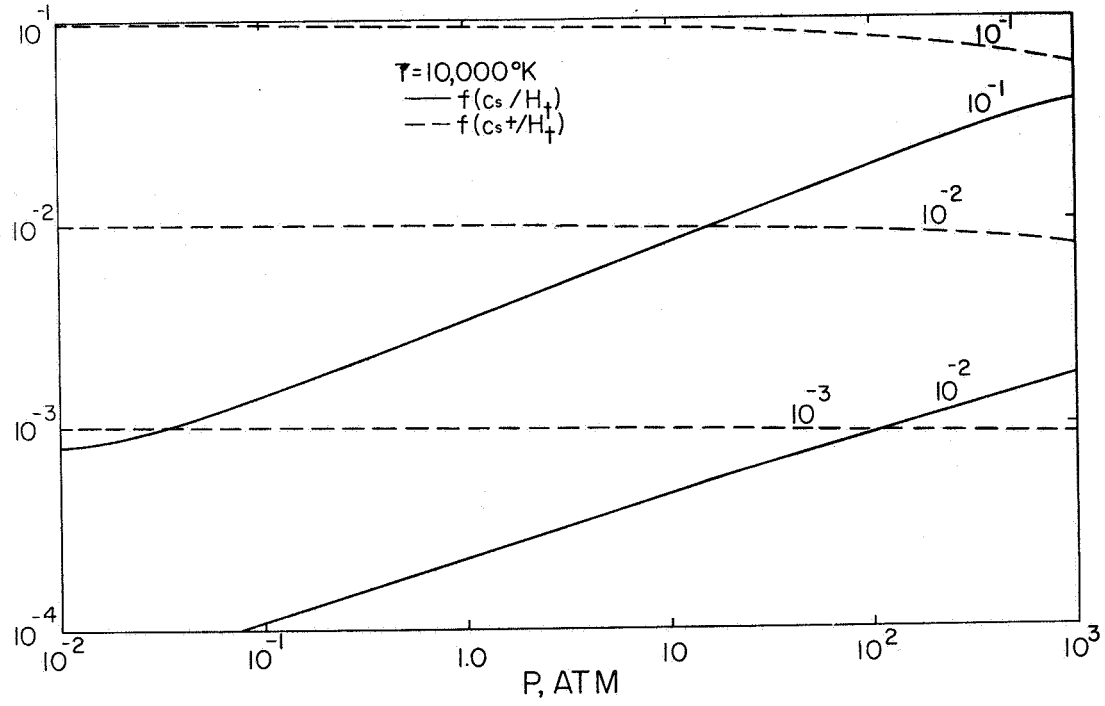

FIG. 6 The ratio of Cs atoms and of Cs^+ ions to hydrogen particles (atoms and ions) at 10,000°K. Nomenclature is the same as Fig. 4.

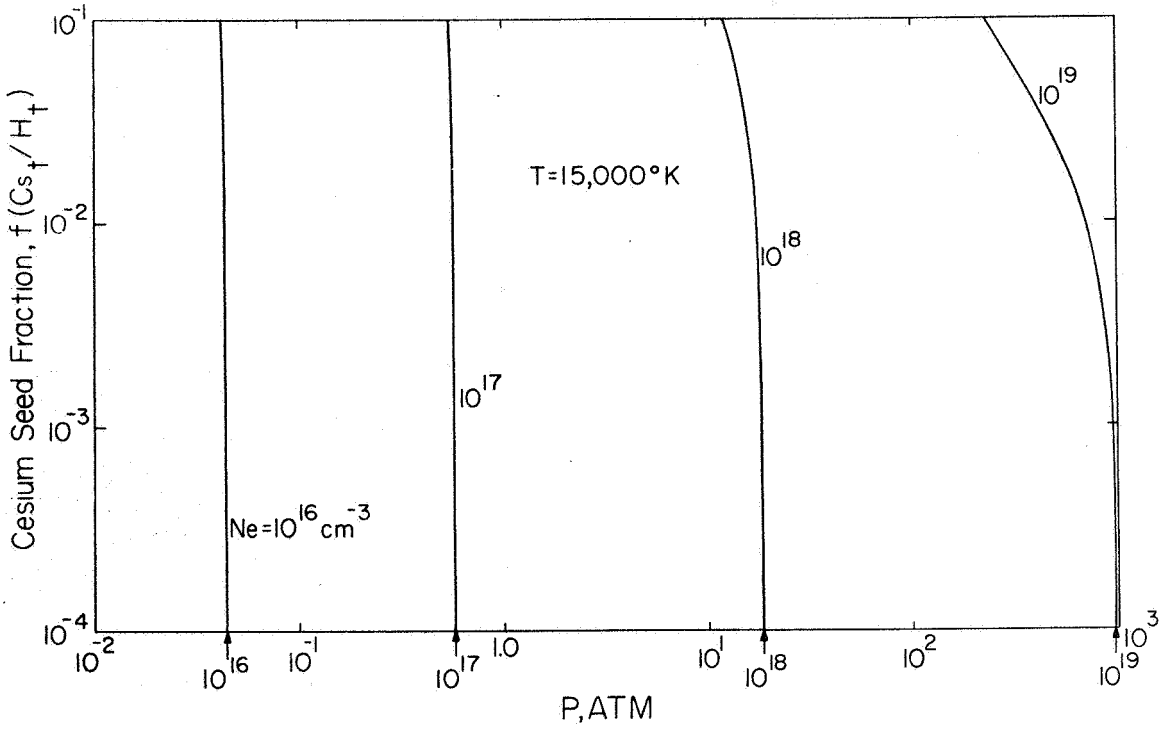

FIG. 7 Electron density in a cesium-hydrogen plasma at 15,000°K. Nomenclature is the same as Fig. 3.

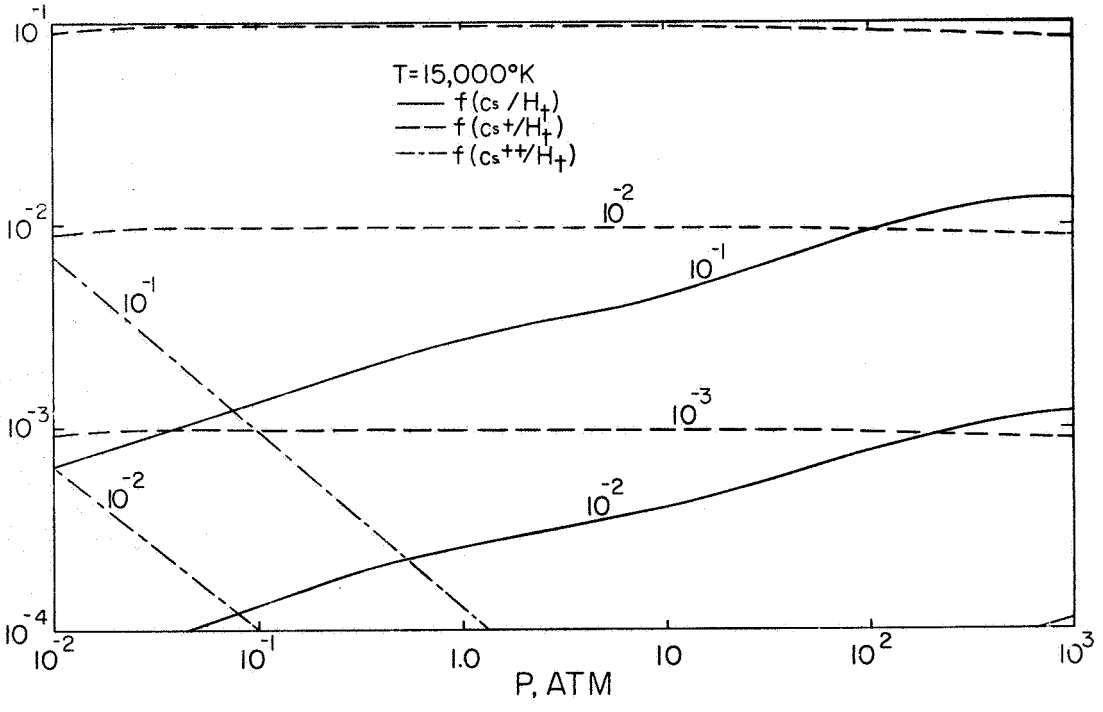

FIG. 8 Ratio of Cs atoms and of Cs^+ ions to hydrogen particles (atoms and ions) at 15,000°K. Nomenclature is the same as Fig. 4.

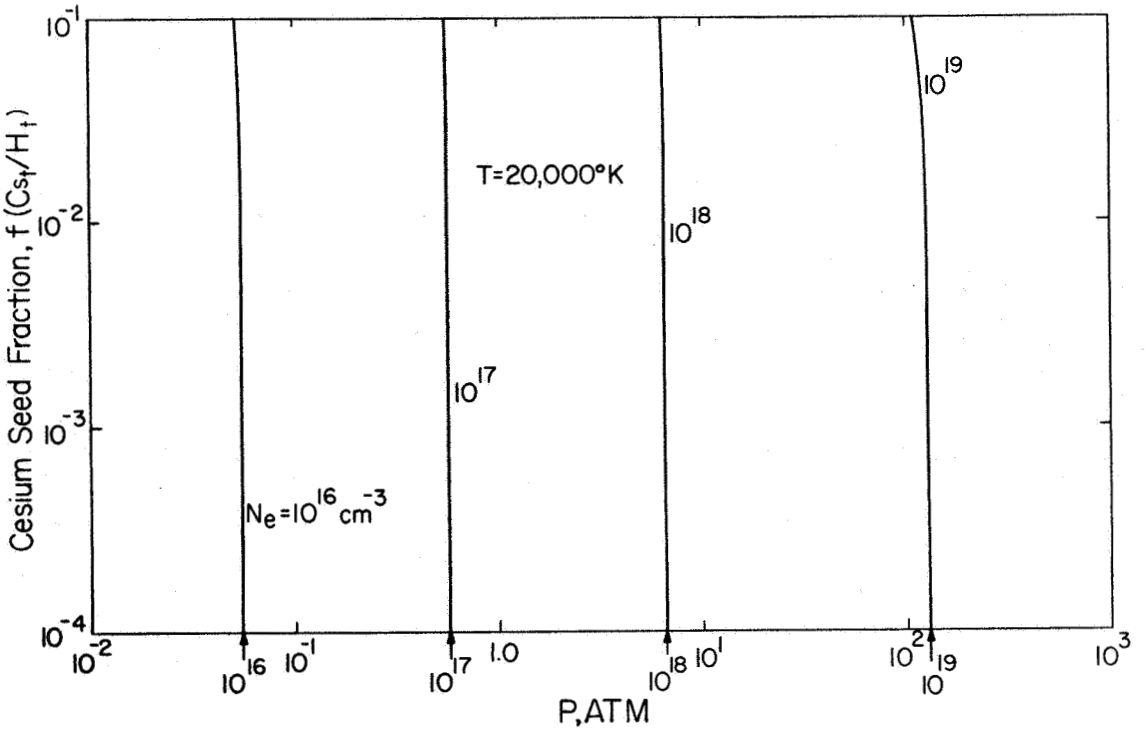

FIG. 9 Electron density in a cesium-hydrogen plasma at 20,000°K. Nomenclature is the same as Fig. 3.

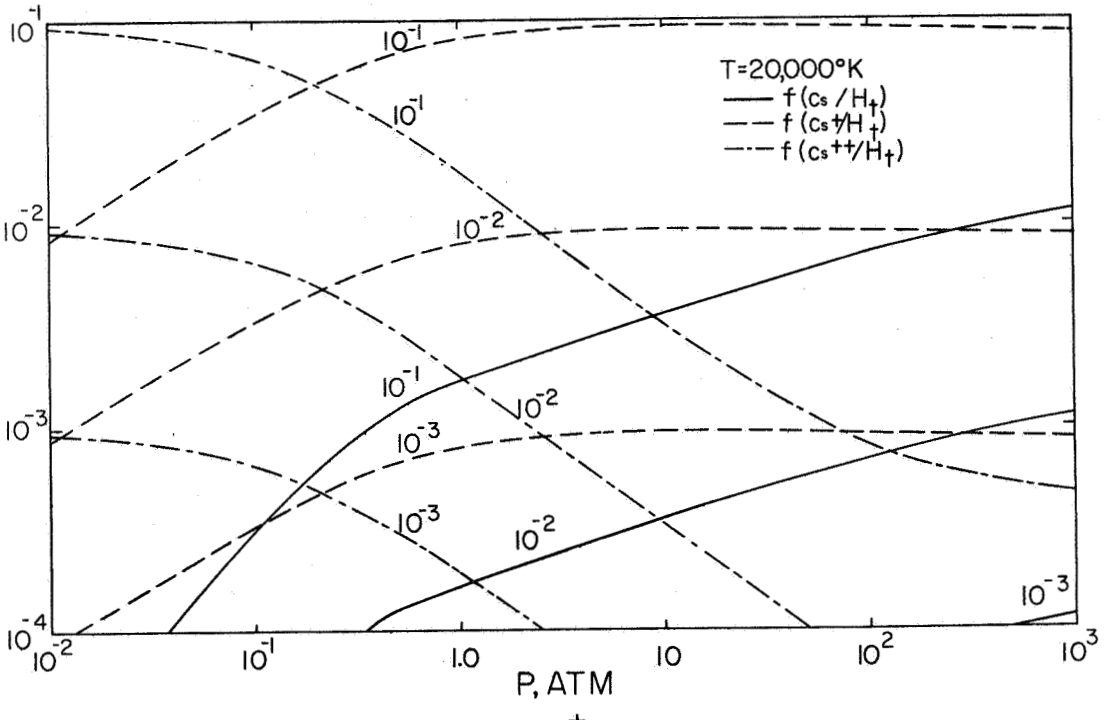

FIG. 10 Ratio of Cs atoms and of Cs^+ ions to hydrogen particles (atoms and ions) at 20,000°K. Nomenclature is the same as Fig. 4.

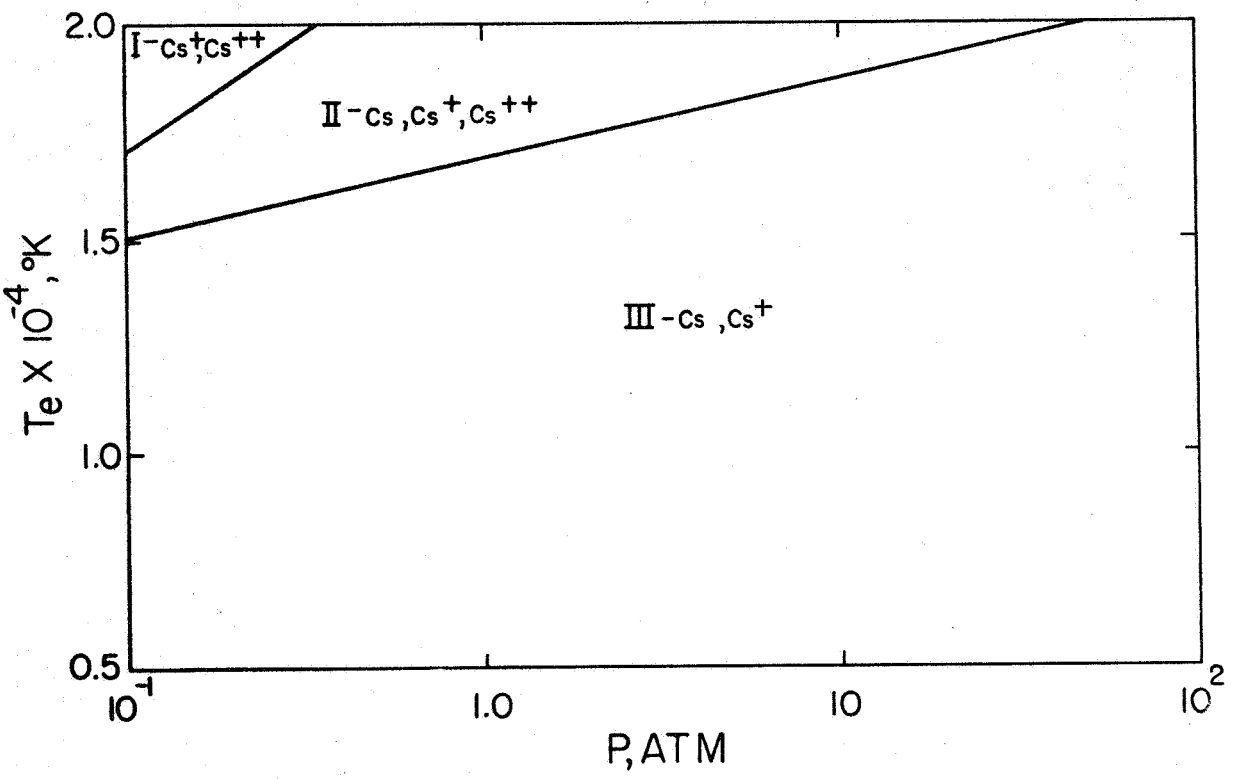

FIG. 11 Temperature-pressure regions where the indicated cesium species constitute more than 1% of the total cesium concentration. Seed fractions from 10^{-3} to 10^{-1} have been considered.

(ergs/cm^2 sec), S_{ij} is the line shape (sec) for transition from level i to level J, N_i is the population density of level i (cm^{-3}), N_e is the electron density and the σ's are cross sections (cm^2). The summations are over bound levels.

The species H, Cs^+ and Cs^{++} have absorption lines for photons in the region being considered. The only hydrogen absorption lines which need be considered are the Lyman series. Five shapes resulting from Stark broadening for the first two members of the series are available in tabular form for a range of temperatures and densities.[3] The profile of higher numbers of the series approaches a dispersion profile with a half-width due to broadening by electron impact.[4] The absorption oscillator strengths needed to compute the B_{ij} for hydrogen are well known.[5]

The constituent calculations discussed in (ii) reveal that there is little or no exicted Cs^+ or Cs^{++} for the conditions of interest. Hence line absorption by any but the ground states of these two ions can be neglected. Oscillator strengths and line shapes for these lines are currently unavailable. Approximate oscillator strength values for Cs^+ can be obtained from coulomb approximation techniques,[6] and line widths can be calculated from Stark broadening theory. Reliable calculations of oscillator strengths or line shapes cannot be made for Cs^{++}, however. The energy level structure of Cs^{++} is not well enough known and Stark broadening theory requires modification if the perturbing ions are multiply charged. Hence line absorption by Cs^{++} will be neglected and calculations of the photoabsorption coefficient in regions I and II of Fig. 11 must be considered incomplete and less reliable.

Exact theoretical expressions are available for the bound-free absorption cross section of hydrogen.[7] Photoionization of the ground state of hydrogen is expected to be the major contributor to the absorption coefficient (threshold at 13.6 eV). Excited states will contribute negligibly, except at high temperatures wherey they are significantly populated. Their thresholds for photoionization are at or below 3.2 eV.

Theoretical values for the photoionization cross sections of Cs are available from previous work.[8] Only the ground and first two excited states are expected to contribute significantly. Thresholds are at 3.89 eV, 2.46 eV and 2.09 eV. Photoionization of Cs^+ can be neglected since the

threshold for the ground state is above 25 eV, and the population of the first excited state (threshold 11.6 eV) is extremely low under these conditions.

The contribution to the absorption coefficient from free-free transitions in the fields of the three ionic species H^+, Cs^+ and Cs^{++} can be computed from available formulae (modified hydrogenic formulae).[9]

Work during the next quarter will be directed to calculations of the needed oscillator strengths and line shapes for Cs^+ and to formulation of the equations for computer calculation of $K(\nu,T)$.

III. ARC JET

The arc jet was described in the previous quarterly report.

The original layout of the ballast resistor has been modified because of the large static weight of the cooling water. This has been completed and the ballast resistor itself has been constructed. Construction and assembly of a frame for the component is underway. A procedure for starting the jet has also been devised. The jet is expected to be operated for the first time in September.

The high resolution scanning monochromator (Jarrell-Ash Model 78-420) obtained for this program has been used to measure line shapes in a cesium plasma. These measurements have demonstrated the utility of the instrument.

IV. REFERENCES

1. D. B. Olfe, J. Quant. Spectry. Rad. Trans. 1, 104 (1961).

2. C. W. Allen, Astrophysical Quantities (Athlone Press, University of London, 1964), p. 102.

3. H. R. Griem, Plasma Spectroscopy (McGraw Hill, New York, 1964), p. 88.

4. H. R. Griem, Astrophys. J. 132, 883 (1960).

5. L. G. Green, P. P. Rush and C. D. Chandler, Ap. J. Suppl. Series, 3, 37 (1957).

6. D. R. Bates and A. Damgaard, Phil. Trans. Roy. Soc. London, A242, 101 (1949).

7. L. H. Aller, Astrophysics (Ronald Press, New York, 1963), 2nd ed.

8. D. W. Norcross and P. M. Stone, J. Quant. Spectry. Rad. Trans. 6, 277 (1966).

9. H. R. Griem, op. cit., p. 105.

V. APPENDIX

Minor errors have been discovered in the final report for the period 1 December 1965 though 30 November 1966. None of these errors alter any of the results or conclusions of the report. They are as follows:

page 4, Eq. (3) should read

$$N_U = \frac{g_U}{g_1} N_1 \, e^{-E_U/kT}$$

page 6, Eq. (4) should read

$$I = 1.0542 \times 10^7 \frac{g_L \, f_{LU} \, N_1 e^{-E_U/kT}}{g_1 \lambda^3}$$

$[\lambda \text{ in } \text{Å}]$

page 16, Eq. (9) should read

$$\ell n \frac{I \, \lambda^3 g' f'}{I' \lambda'^3 g f} = \frac{E' - E}{kT}$$

page 18, Eq. (10) should read

$$\frac{I'}{I} = \frac{1.17 \times 10^{22}}{N_e} \left(\frac{T}{18,000} \right)^{3/2} \frac{f' g' \lambda'^3}{f g \lambda'^3} \exp\left(- \frac{E' + E_\infty - E - \Delta E_\infty}{kT} \right)$$

page 19, The right hand axis in Fig. 9 applies only to the NII/NI curve.